UC Berkeley
UC Berkeley Previously Published Works

Title
Reconstructing Cortical Dynamics with Magnetoencephalography

Permalink
https://escholarship.org/uc/item/2w94g7xb

Journal
ProQuest Dissertatoins and Theses, Aug 2007

Author
Dalal, Sarang S.

Publication Date
2007-03-26

Peer reviewed

eScholarship.org Powered by the California Digital Library
University of California

Reconstructing Cortical Dynamics with Magnetoencephalography

by

Sarang Suresh Dalal

DISSERTATION

Submitted in partial satisfaction of the requirements for the degree of

DOCTOR OF PHILOSOPHY

in

BIOENGINEERING

in the

GRADUATE DIVISIONS

of the

UNIVERSITY OF CALIFORNIA, SAN FRANCISCO

and the

UNIVERSITY OF CALIFORNIA, BERKELEY

Copyright © 2007

by

Sarang Suresh Dalal

Abstract

Reconstructing Cortical Dynamics with Magnetoencephalography

by

Sarang Suresh Dalal

The dynamics of neural information processing are complicated, and determining the sequence and mode of activation is equally important to determining which areas activate. Magnetoencephalography (MEG) and electroencephalography (EEG) noninvasively measure the electromagnetic fields directly generated by neuronal currents in the human brain. The potential to accurately localize these signals has emerged with the advent of dense, whole-head sensor arrays. Adaptive spatial filtering techniques such as beamforming are often used reconstruct the sources of MEG/EEG activity. I have developed extensions to apply beamforming to more experimental paradigms as well as a method for more accurate validation with intracranial EEG.

Beamformers poorly resolve brain sources that are strongly correlated temporally with one another, as might be expected for an auditory experiment. I presented a method to reject the contribution of potentially interfering sources in a user-defined suppression region while allowing for source reconstruction at other specified regions. Performance of the algorithm was validated with data from sim-

ulations and an auditory MEG experiment.

Few methods exist for localizing spectral power changes with MEG. I described a novel method that uses beamformers optimized for time-frequency source reconstruction from MEG data. The performance of the method was demonstrated with simulated sources and was also applied to real MEG data from a finger movement task. Modulations in both the beta band and, importantly, the high gamma band were revealed in sensorimotor cortex and found to be statistically significant across subjects. These results were additionally validated by intracranial EEG data from two epilepsy patients. Another compelling finding was high frequency activity (30-300 Hz) in the cerebellum.

Finally, while intracranial recordings are considered the gold standard for validating noninvasive measurements, often electrode locations are not precisely known. One common method, CT-MRI coregistration, may result in a localization error of more than 10 mm. To address this, I developed a procedure to link preoperative MRIs, surgical photographs, and postimplant X-rays with projective transforms.

Acknowledgments

Several people deserve mention in making this work possible.

First and foremost, I would like to thank my Ph.D. advisor, Dr. Sri Nagarajan, for his excellent mentorship. His enthusiasm and extensive knowledge of both neuroscience and signal processing has been an inspiration to me. While we may have had some lively disagreements, his dedication and faith in my skills encouraged me to persevere through moments of despair while challenging me at every turn. I am deeply grateful for the opportunity we have had to learn from each other and am proud to be his first dissertation student.

My other dissertation committee members, Dr. Heidi Kirsch, Dr. Bob Knight, Dr. John Houde, and Dr. Stan Klein, have been wonderful collaborators, mentors, and commiserators during my graduate school career. Their contributions to my knowledge and research opportunities are reflected on virtually every page of this dissertation. I additionally thank Dr. Tom Ferrée for an excellent introduction to the physics of electromagnetic neuroimaging and, along with Dr. Dan Vigneron, exemplary service on my qualifying exam committee.

Dr. Kensuke Sekihara of Tokyo Metropolitan University kindly shared his experience with source localization methods, suggested avenues of research, and provided helpful critiques, not to mention treated me to several sushi dinners.

Much of this work was made possible by neurosurgeons Dr. Nick Barbaro and Dr. Mitch Berger. Dr. Paul Garcia and Dr. David Filippi welcomed us to the UCSF Epilepsy Monitoring Unit and showed great patience with the scruffy graduate students who periodically invaded their ward with an intimidating rolling cart of amplifiers and computers. All of them, along with Gil Woo, kindly provided assistance in coordinating our research studies with their patients.

Dr. Chuck Yingling and Dr. Leon Deouell introduced me to several key principles of neuroscience and experimental design during rotation projects that preceded this dissertation work. Both are truly an inspiration to all around them.

My colleagues in the Biomagnetic Imaging Lab have been incredible collaborators and friends. For the past few years, I have shared an office and most of my waking hours with Johanna Zumer and Kenneth Hild; I will miss the countless discussions, arguments, and laughs. Anne Findlay, Susanne Honma, and Mary Mantle were always happy to spare a moment to assist in collecting MEG data, help with a problem, or simply offer friendly company. Adrian Guggisberg helped me refine the time-frequency methods described in this dissertation and was always willing to explore California with me. Dave McGonigle provided some of the initial impetus for developing NUTMEG and first introduced me to the joy of

after-work happy hours—on Sunday night. Thanks to Ilana Hairston, Virginie van Wassenhove, Leighton Hinkley, and Julia Owen for the pleasure of working with them.

My collaborators in Bob Knight's lab at UC Berkeley were instrumental in the acquisition of intracranial recordings, including Ryan Canolty and Maryam Soltani. I especially acknowledge Erik Edwards for his infamous time-frequency analyses and insights into high gamma activity—which inspired me to investigate methods for localizing time-frequency components noninvasively with MEG—as well as for prodding me to develop my ideas for better intracranial electrode localization. These and other members of the Knight Lab have provided great moral support, especially Tami Harrison, Laura Hale, Cathrine Dam, and Christina Karns.

My roommates over the years all deserve commendation for their patience, understanding, and friendship, including Mandy Brice, Tané Bechtold, Alessandra Vitale, Shauna Nyborg, Martin Lee, Alexis Wright, and Aaron Brick. Other friends who deserve special mention are Jason Varughese, Rahul Thakar, Nick Toriello, Mariel Velez, Carmel Levitan, and Jennifer Park.

I acknowledge the State of California for funding my initial training through the UCSF Dean's Health Sciences Fellowship and the Roman Reed Fellowship. The United States Government funded my dissertation project primarily through an NIH/NIDCD NRSA Fellowship (F31 DC006762). I hope that our great nation will soon be led once again by an administration that respects the principles of

science and education over political expediency and will restructure its advisory panels and funding accordingly.

Lastly, I am grateful to my family for their endless support and encouragement. My parents, Suresh and Bharti, are responsible for stimulating my curiosity about the world and allowing me to follow my own path. I have always admired my brother, Sunil, and appreciate all the help and humor he has offered over the years. He and his wife, Sonal, have been incredibly supportive of my graduate career. And, finally, I thank their beautiful children, Naia and Milan, for reminding me about the important things in life.

Chapter 2 is a reprint of an article in *IEEE Transactions on Biomedical Engineering* (Dalal et al., 2006) and Appendix A is adapted from an article published in *Neurology and Clinical Neurophysiology* (Dalal et al., 2004).

Contents

List of Tables

List of Figures

Chapter 1

Introduction

1.1 Background and Significance

The noninvasive study of human cortical networks is of great interest to the cognitive neuroscience community. Examination of these networks may provide valuable information for clinicians as well; currently, brain surgery patients with lesions near critical language areas must undergo awake mapping during surgery in order to prevent deficits resulting from inadvertent resection. An accurate, non-invasive technique could eventually obviate the need for such an intimidating procedure, as well as be applicable to other conditions that may manifest themselves as disruptions in cortical pathways, such as learning and psychiatric disorders.

The dynamics of neural information processing are complicated, and determining the sequence of activation is equally important to determining which areas

activate. Magnetoencephalography (MEG) (Cohen, 1968) and electroencephalography (EEG) (Berger, 1929) noninvasively measure the magnetic and electric fields generated by neuronal currents, and so can detect activity with fine temporal resolution. The potential to accurately localize these signals has emerged with the advent of dense, whole-head MEG sensor arrays.

1.2 MEG and EEG Physiology

The fortuitous anatomical arrangement of cortical pyramidal cells allows the noninvasive detection of their activity by MEG and EEG (Freeman, 1975). The long apical dendrites of these cells are arranged perpendicularly to the cortical surface and parallel to each other (Ramón y Cajal, 1904) (Figure 1.1), allowing their electromagnetic fields to often sum up to magnitudes large enough to detect at the scalp (Freeman, 1975). Synchronously fluctuating dendritic currents result in electric and magnetic dipoles that produce these electromagnetic fields (Nunez and Srinivasan, 2006).

Hence, MEG and EEG can directly measure neuronal activity on a millisecond time scale, and are ideally suited for noninvasively studying macroscopic neural dynamics in humans. In comparison, other functional brain imaging modalities such as functional magnetic resonance imaging (fMRI) or positron emission tomography (PET) are limited to temporal resolutions on the order of a second, due

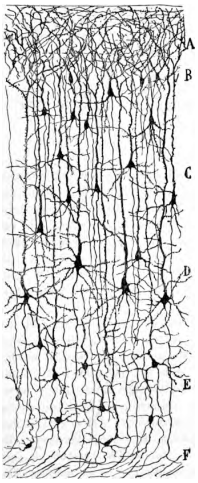

Figure 1.1 EEG and MEG primarily record the postsynaptic activity of pyramidal cells in the cerebral cortex, depicted above in a classic tracing of a Golgi stain by Ramón y Cajal (1905). These cells are characterized by their long apical dendrites, and their arrangement in parallel is thought to facilitate the summation of their electromagnetic fields when they are synchronously active.

to the physiological time constants of measurements such as regional blood flow and glucose metabolism.

However, EEG recordings are subject to distortion and smearing as they pass through tissue and fluid with differing electrical conductivities (Malmivuo and Plonsey, 1995; Nunez and Srinivasan, 2006). Consequently, variability in head shape as well as abnormal conductivities due to tumors or other lesions can result in occasionally drastic distortion from expected results (van den Broek et al., 1998); patients who have had prior brain surgery are especially problematic since craniotomies inherently disturb the volume conductor properties of the scalp, skull, and dura (Kirchberger et al., 1998). In contrast, the magnetic susceptibility of all biological tissue is practically constant and therefore MEG does not suffer from

Figure 1.2 Shown above is the MEG system (VSM MedTech, Coquitlam, BC, Canada) installed at the UCSF Biomagnetic Imaging Laboratory. The helmet above the volunteer contains the SQUID-based magnetic field sensors, while the large cylindrical dewar contains liquid helium to cool them to their superconducting operation temperature. The subject is shown wearing a high-density electrode cap for optional simultaneous recording of EEG.

this shortcoming (Malmivuo and Plonsey, 1995). Furthermore, EEG recordings require a reference channel that may couple activity into all other channels, while MEG recordings are reference-free. Finally, the density of EEG electrode arrays are partially limited by the large amount of preparation time per electrode as well as comfort level for volunteers and particularly patients. MEG tends to be more comfortable since recordings can be done in a supine or prone position with a loose-fitting helmet (see Figure 1.2), and sensor density is limited by the diameter of the magnetic pickup coils.

MEG does have a few disadvantages compared to EEG. Since the sensors are

not fixed to the head, MEG is subject to movement artifacts and spatial blurring of source reconstructions. The superconducting quantum interference device (SQUID) technology and heavily shielded rooms currently required to pick up the weak magnetic fields of MEG (Vrba and Robinson, 2002) make the equipment expensive to acquire and maintain, limiting its prevalence to major academic medical centers. Finally, magnetic field strength decreases with distance from source more sharply than electric potentials resulting in a smaller half-sensitivity volume (Malmivuo et al., 1997; Gulrajani, 1998). (However, this may also be advantageous for inverse techniques, since sensors are less correlated and distant sources introduce less noise.)

Another important difference between EEG and MEG are their differing orientation sensitivities. Unfortunately, many textbooks and scholarly articles present an overly simplified view of these properties. The standard wisdom is that electroencephalography primarily records tangential (i.e., gyral) activity, while magnetoencephalography is only sensitive to radial (i.e., sulcal) activity and cannot record tangential currents *at all*. This assertion follows from the common model of the head as a perfectly spherical volume conductor (Sarvas, 1987)—the magnetic fields of radial currents do indeed cancel out in such a model. However, while the spherical model greatly simplifies the mathematics behind lead field calculations, it is clearly a bit of a stretch; discrepancies in shape aside, the head also has large cylindrical conductors attached to it in the form of the neck and body! Further-

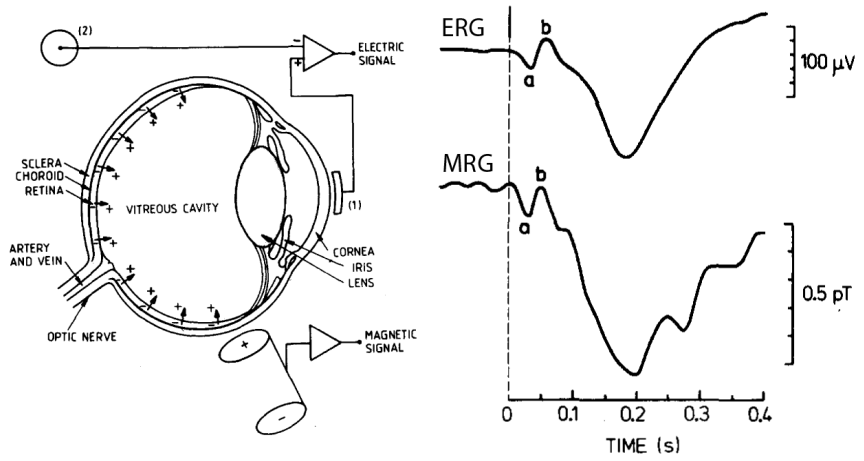

Figure 1.3 The electroretinogram (ERG) measures fluctuations in the transretinal potential. The recording of the corresponding magnetic field fluctuations is referred to as *magnetoretinography* (MRG). Above left is a schematic of the eye showing the orientation of retinal currents. Above right are ERG and MRG tracings evoked by a brief light flash in the same subject. Their similarity shows that an organ closely approximating a spherical volume conductor can still generate externally detectable magnetic fields; it follows that the MEG should similarly be capable of recording radial (i.e., gyral) currents generated within the nonspherical head. Reprinted with permission from Katila et al. (1981).

more, gyral pyramidal cells are not necessarily orthogonal to the skull surface in all locations. Therefore, while tangential currents may dominate MEG recordings, radial currents will nevertheless produce some signal.

The magnetoretinogram reported by Katila et al. (1981) may provide a good argument to this effect—the eye is arguably much better approximated by the spherical volume conductor than the head due to both its shape and tissue content, and retinal cells are quite uniformly perpendicular to the posterior of the eye (Ramón y Cajal, 1893). Nevertheless, the magnetoretinogram picks up the nearly the same waveform as the electroretinogram (Figure 1.3). So, even these small deviations

from the radial configuration and the spherical volume conductor model appear to allow significant magnetic fields to escape the eye. We can therefore presume that MEG—particularly considering its much poorer fit to the spherical model—must be able to record radial currents.

1.3 MEG/EEG Activation Models

Continuous MEG or EEG recordings can appear to be devoid of structure. Indeed, the response to even carefully controlled stimuli contains a variety of noise sources from the environment as well as significant signal from unrelated background neural activity. Cognitive neuroscience experiments are usually designed with hundreds of trials (stimulus repetitions) to overcome this issue.

The prevailing model for the last three decades of EEG/MEG research assumes that the stimulus or task evokes a tightly time-locked response that is superimposed over ongoing "brain noise." Therefore, the responses are averaged over trials to form an *event-related potential* (ERP) in the case of EEG or an *event-related field* (ERF) in the case of MEG. In this way, noise that is uncorrelated to the stimulus will average to zero, while neural responses phase-locked to the stimulus remain, boosting the signal-to-noise ratio (SNR). However, oscillatory components of the true neural response may also be lost if there is jitter in the brains response or if they are otherwise not perfectly phase-locked across trials. Oscillations greater

than about 40 Hz (the high gamma range) are particularly susceptible to this effect, as are the 20 Hz beta desynchronizations associated with motor activity.

Consequently, *event-related spectral perturbation* (ERSP) analyses are becoming increasingly popular to extract more information out of MEG and EEG (Pfurtscheller and Aranibar, 1977; Pfurtscheller and Neuper, 1992; Makeig, 1993; Pfurtscheller and Lopes da Silva, 1999). These analyses transform unaveraged EEG/MEG data into the frequency domain with short-time Fourier transforms (STFTs) or wavelet transforms before averaging the resulting spectrograms across trials and contrasting with a baseline period. In this way, ERSPs characterize oscillatory activity that is time-locked to the stimulus but not necessarily phase-locked. This analysis technique has recently been used in several intracranial EEG studies to reveal focal high gamma activity associated with several types of stimuli and tasks (Crone et al., 1998, 2001a,b; Lachaux et al., 2005; Brovelli et al., 2005; Edwards et al., 2005; Canolty et al., 2006). Especially interesting is that recent studies have suggested neocortical high gamma activity detected with MEG and intracranial EEG correlate best with fMRI results (Logothetis et al., 2001; Mukamel et al., 2005; Niessing et al., 2005; Brovelli et al., 2005; Hoogenboom et al., 2006; Lachaux et al., 2007). Methods are now being developed to combine time-frequency analyses with source localization methods to provide powerful noninvasive tools for studying cortical dynamics (Singh et al., 2002; Gaetz and Cheyne, 2006; Hoogenboom et al., 2006). I will implement and validate such an approach in Chapter 3.

1.4 MEG/EEG Source Localization Algorithms

1.4.1 Overview

Magnetic source imaging (MSI) identifies the location and timing of neural activity using MEG. Most inverse procedures for EEG/MEG data can be classified as either multiple dipole or imaging methods. Traditional multiple dipole methods assume that a small set of current dipoles can adequately represent the distribution of an unknown source. The dipole locations and moments form a set of unknown parameters which are typically found using a non-linear least square fit or by using multiple signal classification algorithms (MUSIC) algorithms (Scherg and von Cramon, 1986; Phillips et al., 1997). While these methods are ideal for point or focal sources, they perform poorly for distributed sources and non-dipolar sources (Jeffs et al., 1987). Another common constraint is to assume that the sources are temporally uncorrelated (Mosher et al., 1999). These assumptions are appropriate when analyzing sensory responses, where activity might be relatively focal and constrained to primary sensory areas.

An alternative approach to the inverse problem is to impose constraints based on anatomical and physiological information that can also be derived from information from other imaging modalities such as structural and functional MRI. For example, using structural MRI, MEG sources can be constrained to the cortex with an orientation normal to the surface (Dale and Sereno, 1993). By tessellat-

ing the cortex into disjoint regions and representing the sources in each region by an equivalent current dipole oriented normal to the surface, the forward model relating the sources and the measurements can be written as a linear model with additive noise. Such a formulation transforms the inverse problem into an imaging method, since it now involves the estimation of electrical activity at discrete locations over a finely sampled reconstruction grid.

The inverse problem can be formulated either in the time domain or in the frequency domain. In the time-domain the problem can be based on either a single time point or an entire spatiotemporal data set (Scherg and von Cramon, 1986). In the frequency domain, the recorded electric and magnetic fields at each channel are transformed into the frequency domain by taking its fast Fourier transform (FFT). Both approaches of source localization are found to be mathematically analogous with similar spatial resolutions (Lehmann and Michel, 1990; Lütkenhöner, 1992; Raz et al., 1995; Salmelin and Hämäläinen, 1995). In either of these domains, the current sources can be modeled by multiple equivalent dipoles or by distributed dipole sources. Alternatively, the inverse problem can be formulated in the time-frequency domain (Sekihara et al., 1999, 2000), which I will explore further in Chapter 3.

Moreover, studies of the inverse problem have traditionally focused on improving the spatial resolution of MEG and EEG, with the accepted limit being on the order of 2 mm to 5 mm (Mosher et al., 1993; Leahy et al., 1998). However, a second

problem in MEG/EEG involves estimating the time course of source activations. Our group developed an efficient method for estimating the time course of neural activity over the brain volume based on a spatial filtering technique called beamforming (Van Veen et al., 1997; Sekihara et al., 2001). This method does not require *a priori* assumptions about the location or number of neural sources. Therefore, in contrast to linear estimation methods, it is applicable to situations in which there are interfering sources with unknown locations in addition to the source of interest. Using such a class of algorithms, it is now possible to view MEG source reconstruction as a "virtual depth electrode" measurement technique.

1.4.2 Beamforming

Since beamforming forms the basis for many of the techniques I will develop in this dissertation, I will now briefly describe its mathematical formulation. (See Figure 1.4 for a general overview of the beamforming algorithm.)

Definitions and Problem Formulation

We shall define the magnetic field measured by the mth detector coil at time t as $b_m(t)$ and a column vector $\boldsymbol{b}(t) \equiv [b_1(t), b_2(t), \ldots, b_M(t)]^T$ as a set of measured data, where M is the total number of detector coils, and the superscript T indicates the matrix transpose. The spatial location is represented by a 3-D vector $\boldsymbol{r}$ such that $\boldsymbol{r} = (x, y, z)$. To express the moment magnitudes of the sources located at $\boldsymbol{r}$ at time t

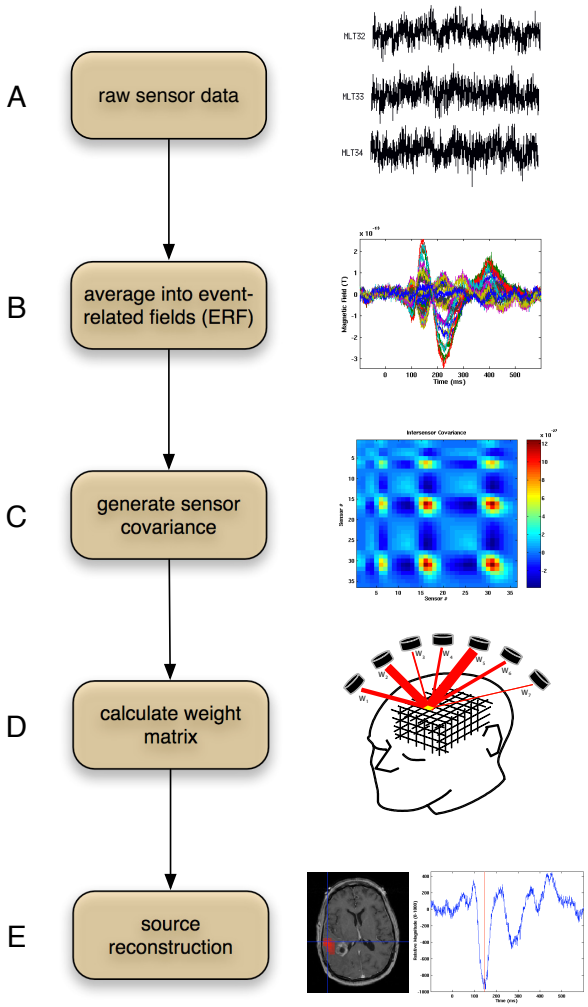

Figure 1.4 Overview of the beamforming algorithm as applied to MEG data, in this case an auditory response to a simple tone. a) We start with the raw sensor data. Shown is one trial of data from three channels. b) Typically, data is averaged across trials into event-related fields (ERFs). Notice the impressive amount of structure in the waveform compared to the raw data. c) Sensor covariance is calculated, essentially estimating the correlation between sensors. Along with the forward model, this covariance is used to calculate d), the weight matrix. The weights specify how much each sensor contributes to the signal for any given brain location. e) Applying the weight matrix to the ERF yields a source time series at every desired location in the brain. Here, the shown time series is associated with the location marked with crosshairs on the MRI. This patient had a large tumor adjacent to auditory cortex; MEG results are often used in such cases for preoperative surgical planning.

in the three orthogonal directions, we define $\boldsymbol{s}(\boldsymbol{r},t) \equiv [s_x(\boldsymbol{r},t), s_y(\boldsymbol{r},t), s_z(\boldsymbol{r},t)]^T$. To express the orientation of the qth source, we define the angles between its moment vector and the x, y, and z axes as β_q^x, β_q^y, and β_q^z respectively. The orientation of the qth source is defined as a vector $\boldsymbol{\eta}_q \equiv [\beta_q^x, \beta_q^y, \beta_q^z]$. We assume in this paper that the orientation of each source is time independent.

The second-order moment matrix of the measurement is denoted $\boldsymbol{R}_b$, i.e., $\boldsymbol{R}_b = \langle \boldsymbol{b}(t)\boldsymbol{b}^T(t)\rangle$, where $\langle\cdot\rangle$ indicates the ensemble average. In practice, the ensemble average is often replaced with the time average over a certain time window. When $\langle \boldsymbol{b}(t)\rangle = 0$, $\boldsymbol{R}_b$ is also equal to the covariance matrix of the measurement.

The lead field vector for the μ component of a source at $\boldsymbol{r}$ is defined as $\boldsymbol{l}_\mu(\boldsymbol{r}) \equiv [l_1^\mu(\boldsymbol{r}), l_2^\mu(\boldsymbol{r}), \cdots, l_M^\mu(\boldsymbol{r})]^T$. Here, $l_m^\mu(\boldsymbol{r})$ expresses the mth sensor output induced by the unit-magnitude source that is located at $\boldsymbol{r}$ and oriented in the μ direction, where μ such that $\mu \in \{x, y, z\}$. We define the lead field matrix as $\boldsymbol{L}(\boldsymbol{r}) \equiv [\boldsymbol{l}_x(\boldsymbol{r}), \boldsymbol{l}_y(\boldsymbol{r}), \boldsymbol{l}_z(\boldsymbol{r})]$, representing the sensitivity of the sensor array at $\boldsymbol{r}$ in all three orthogonal directions. For clarity, we will model the head as a spherical volume conductor, reducing the lead field to two orthogonal components in spherical coordinates, θ and ϕ (Sarvas, 1987). In this case, the orientation of the qth source can instead be represented by a vector $\boldsymbol{\eta}_q = [\beta_q^\theta, \beta_q^\phi]^T$, resulting in $\boldsymbol{L}(\boldsymbol{r}) = [\boldsymbol{l}_\theta(\boldsymbol{r}), \boldsymbol{l}_\phi(\boldsymbol{r})]$.

Conventional Adaptive Spatial Filtering

An adaptive spatial filter estimate of the source moment matrix $\hat{\boldsymbol{s}}(\boldsymbol{r},t)$ is given by applying a set of weights to the measurement data:

$$\hat{\boldsymbol{s}}(\boldsymbol{r},t) = \boldsymbol{W}^T(\boldsymbol{r})\boldsymbol{b}(t) \tag{1.1}$$

In the above equation, $\boldsymbol{W}(\boldsymbol{r}) \equiv [\boldsymbol{w}_\theta(\boldsymbol{r}), \boldsymbol{w}_\phi(\boldsymbol{r})]$ and $\hat{\boldsymbol{s}}(\boldsymbol{r},t) \equiv [\hat{s}_\theta(\boldsymbol{r},t), \hat{s}_\phi(\boldsymbol{r},t)]^T$, where $\boldsymbol{w}_\theta(\boldsymbol{r})$ and $\boldsymbol{w}_\phi(\boldsymbol{r})$ are the weight vectors for the θ and ϕ directions, respectively, while $\hat{s}_\theta(\boldsymbol{r},t)$ and $\hat{s}_\phi(\boldsymbol{r},t)$ are the corresponding components of the source moment vector.

Omitting $\boldsymbol{r}$ from the expression, the weight vectors $\boldsymbol{w}_\theta$ and $\boldsymbol{w}_\phi$ are calculated with the following constraints:

$$\begin{aligned} &\min_{\boldsymbol{w}_\theta} \boldsymbol{w}_\theta^T \boldsymbol{R}_b \boldsymbol{w}_\theta \quad \text{subject to} \\ &\qquad \boldsymbol{l}_\theta^T(\boldsymbol{r})\boldsymbol{w}_\theta = 1 \quad \text{and} \quad \boldsymbol{l}_\phi^T(\boldsymbol{r})\boldsymbol{w}_\theta = 0, \end{aligned} \tag{1.2}$$

$$\begin{aligned} &\min_{\boldsymbol{w}_\phi} \boldsymbol{w}_\phi^T \boldsymbol{R}_b \boldsymbol{w}_\phi \quad \text{subject to} \\ &\qquad \boldsymbol{l}_\theta^T(\boldsymbol{r})\boldsymbol{w}_\phi = 0 \quad \text{and} \quad \boldsymbol{l}_\phi^T(\boldsymbol{r})\boldsymbol{w}_\phi = 1. \end{aligned} \tag{1.3}$$

The solution is known to be (Van Veen et al., 1997):

$$\boldsymbol{W}_{mv}(\boldsymbol{r}) = [\boldsymbol{L}^T(\boldsymbol{r})\boldsymbol{R}_b^{-1}\boldsymbol{L}(\boldsymbol{r})]^{-1}\boldsymbol{R}_b^{-1}\boldsymbol{L}(\boldsymbol{r}). \tag{1.4}$$

An eigenspace-projected extension to the minimum variance beamformer is obtained by projecting the weight matrix of the LCMV beamformer onto the signal

subspace of the measurement covariance matrix (Sekihara et al., 2001):

$$\begin{aligned} \boldsymbol{W}_E(\boldsymbol{r}) &= \boldsymbol{E}_S \boldsymbol{E}_S^T \boldsymbol{W}_{mv}(\boldsymbol{r}) \\ &= \boldsymbol{E}_S \boldsymbol{E}_S^T [\boldsymbol{L}^T(\boldsymbol{r}) \boldsymbol{R}_b^{-1} \boldsymbol{L}(\boldsymbol{r})]^{-1} \boldsymbol{R}_b^{-1} \boldsymbol{L}(\boldsymbol{r}) \end{aligned} \tag{1.5}$$

where $\boldsymbol{E}_S$ contains the eigenvectors representing the signal subspace of $\boldsymbol{R}_b$. This eigenspace projection overcomes the SNR degradation caused by array mismatch and smoothes time courses of source reconstruction (Sekihara et al., 2001).

One significant problem with beamforming is that performance degrades in the presence of highly correlated sources. For instance, the eigenspace beamformer is robust to moderate source correlations; however, sources that are strongly correlated ($\rho > 0.9$) are poorly resolved (Sekihara et al., 2002a). The whole-head coverage offered by modern MEG systems increases the likelihood of encountering such a situation since bilateral activations are often strongly coherent. For example, beamformer reconstructions of auditory evoked fields (AEFs) commonly exhibit this failure, attenuating the two true sources from each primary auditory cortex and often erroneously placing a single low-amplitude source centered between them. In Chapter 2, I will describe an extension to the eigenspace-projected beamformer to address this problem.

1.5 Reconciling MEG with Intracranial EEG

The recording of electrical signals directly from the cortical surface is a form of intracranial EEG referred to as electrocorticography (ECoG). The opportunity

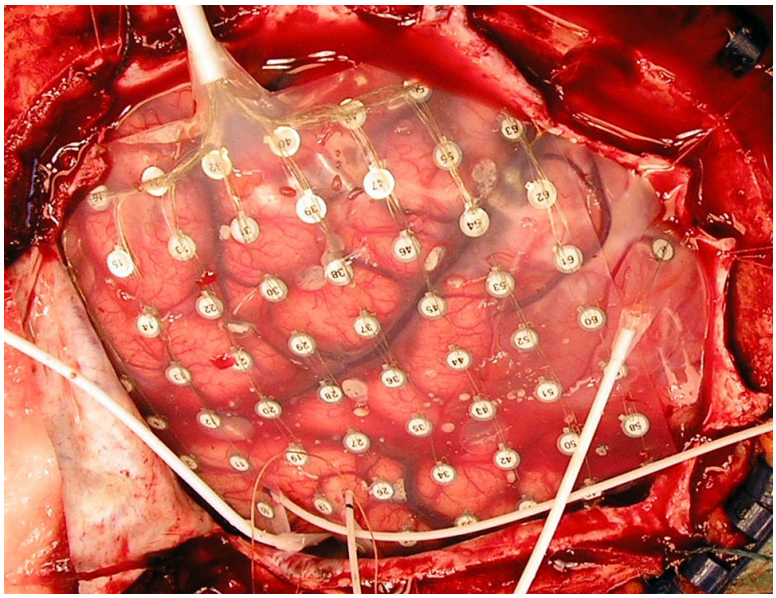

Figure 1.5 Example of ECoG electrodes implanted over a portion of the left hemisphere in an intractible epilepsy patient.

to obtain ECoG in humans is limited to neurosurgery patients with electrodes temporarily applied intraoperatively and to severe epileptics with chonically implanted electrodes (Figure 1.5). ECoG recordings have much in common with scalp EEG and MEG recordings, with the principal advantages being that signal-to-noise ratio and spatial resolution are much improved without the skull and scalp attenuating and smearing the signal.

At UCSF, neurosurgical candidates with planned resections in or near "eloquent" cortex—i.e., sensory, motor, and language areas—routinely undergo preoperative functional mapping with MEG to aid in surgical planning (Schiffbauer et al., 2003). Patients typically participate in a battery of experiments designed to activate motor, language, auditory, somatosensory, and memory. Sometimes, the

results are used to verify hemispheric dominance; the current standard, the Wada test (Wada and Rasmussen, 1960), involves the injection of sodium amobarbital to selectively numb one hemisphere at a time and is sometimes inconclusive. MEG is additionally used to localize seizure foci for intractable epilepsy patients (Tang et al., 2003; Robinson et al., 2004). The results of MEG analyses are used by the neurosurgeon to predict the extent of tissue resection that will minimize postoperative functional deficits.

However, noninvasive techniques are not considered precise enough for certain patient populations. Intracranial EEG is acquired in neurosurgical patients when noninvasive diagnostic techniques prove inconclusive (Bancaud et al., 1965). These recordings also provide rare but highly valuable data to test basic hypotheses in neurophysiology and cognitive neuroscience. Furthermore, intracranial EEG is a promising avenue for the development of neural prostheses designed to aid patients with brain or spinal cord damage resulting from trauma, stroke, or neurodegenerative diseases (Leuthardt et al., 2006; Santhanam et al., 2006; Hochberg et al., 2006).

Awake language mapping is indicated for patients with brain tumors and medically intractable epilepsy at risk of language deficits due to aggressive resection of eloquent cortex (Penfield and Roberts, 1959; Ojemann, 1979; Ojemann et al., 1989), and ECoG is recorded in some of these patients. Additionally, many of the epilepsy patients require long-term invasive monitoring to localize seizure foci as well as to

prevent resection of critical brain areas that would result in cognitive deficits or paralysis (Wyler et al., 1988; Lesser et al., 1991). These patients are implanted with chronic electrodes, often spanning a large grid, that remain in place for about a week.

Both types of patients are regularly seen at UCSF Medical Center. Thus, we were presented with a unique opportunity to collect both preoperative MEG and ECoG in the same patients with identical experimental paradigms.

With ECoG data, it becomes possible to validate many MEG analyses. ECoG studies have shown drastically different results from traditional studies using EEG/MEG sensors (Bullock et al., 1995; Towle et al., 1999). These studies suggest significant fluctuations in cortical dynamics on a millimetric scale. Meanwhile, coherence between EEG/MEG sensors is on the scale of centimeters (Nunez et al., 1997); therefore, the interpretation of EEG/MEG sensor data is clouded by many factors, such as volume conduction (in the case of EEG), unique neural sources being picked up by many sensors, or even common noise sources or reference electrode effects (Fein et al., 1988).

Hence, resolving the detail required for surgical planning or cognitive neuroscience research requires a source localization method. It has historically been difficult to noninvasively evaluate the real-world performance of such methods. In particular, the beamforming method can be subject to straightforward comparisons with ECoG since it estimates a time series of activation at any given point in

the cortical volume. Improved source localization with the millisecond time resolution that MEG provides can not only elucidate mechanisms of cortical function, but may eventually obviate the need for awake language mapping—an understandably intimidating procedure for most patients.

Additionally, ECoG allows confident analysis of higher frequency activity of approximately 60-300 Hz (Crone et al., 1998), known as the *high gamma* band. This frequency band is thought to be a marker for perceptual binding and cognitive processing (Crone et al., 2001a). However, MEG/EEG have thus far been less useful for these experiments due to inherently lower signal-to-noise ratios in this frequency range. While the skull has similar impedance at both low and high frequencies, active patches of cortex can exhibit large phase variability, and the resulting polyphasic summation effectively results in lowpass filtering (Pfurtscheller and Cooper, 1975). It has also been suggested that high gamma activity is more focal compared to lower frequency activity (Crone et al., 1998, 2001a,b; Edwards et al., 2005), implying less signal reaches the scalp since the active patch may be relatively small. Finally, artifactual scalp muscle activity and electromagnetic interference in the high gamma frequency range have further complicated studies with MEG and EEG. Despite these issues, MEG activity in this frequency range is often observed (e.g. Kaiser et al., 2002) and requires validation to gain acceptance by the neuroimaging community.

The ECoG signal, on the other hand, is dominated by cortical tissue directly

in contact with the electrode. Hence, the signal-to-noise ratio is significantly enhanced and the recordings are much less susceptible to muscle artifact interference; cancellation due to polyphasic summing should be less of a hindrance as well. This provides us with an opportunity to distinguish true neural gamma activity recorded with MEG from other sources of artifact. Therefore, ECoG collection provides a convincing means of validation for high gamma activity observed with MEG, as I will show in Chapter 3.

In the course of my involvement with ECoG experiments, however, I came up against a frustrating, yet maddeningly simple problem—we were not always certain where these electrodes ended up. Many intracranial electrodes are inserted deep into the brain or slipped underneath the edge of the craniotomy, and so their final positions are not directly observable. The most common chronic electrode localization technique involves coregistering postimplant CT with preoperative MRI (Grzeszczuk et al., 1992). In Chapter 4, I will illustrate why this method is not satisfactory and present a more accurate alternative that takes advantage of known information from surgical photographs to register all electrodes visible on postimplant X-rays with preoperative MRIs.

1.6 Towards Statistical Group Analyses of MEG Data

Another need for MEG source reconstructions was the normalization of group data. Due to the rapid development of fMRI, sophisticated techniques for evaluating image-based group data have emerged. Functional MRI studies routinely use nonlinear methods to warp individual subject data to normalized brain space, e.g., Talairach space (Talairach and Tournoux, 1988) or Montreal Neurological Institute (MNI) space (Evans et al., 1993; Mazziotta et al., 2001), in order to aid in the analysis and visualization of results. Statistical parametric mapping (SPM) has emerged as the most popular tool for drawing conclusions on a normalized brain (Ashburner and Friston, 1999; Dale et al., 1999; Fischl et al., 1999). These multiple comparison measures provide a way to assess statistical significance from a group of subjects.

Multiple subjects analyses with EEG and MEG, on the other hand, have traditionally been done in sensor space. Source localization techniques have largely been applied on an individual basis. Barnes and Hillebrand (2003) described an application of SPM to MEG beamformers, while Singh et al. (2003) described SnPM (statistical *non*parametric mapping). These developments will ease comparisons of EEG/MEG analyses with fMRI and ECoG and I have incorporated them into our source reconstruction methods.

1.7 Software Development

In order to address all of the shortcomings of existing MEG analysis methods and explore the research avenues mentioned in this introduction, it became apparent that our first task was necessarily to develop our own software toolbox. At the time I started on this project, no publicly available software implemented beamformer algorithms for MEG source reconstruction. Additionally, interactive visualization of 4-D time-varying functional maps, regardless of the algorithm used, was severely lacking.[1] Finally, my fellow graduate student, Johanna Zumer, and I realized that we would be embarking on adventures in algorithm development and data analysis that would require an extensible software framework specifically customized for our needs, yet user-friendly enough for our colleagues. Thus was born the Neurodynamic Utility Toolbox for Magnetoencephalography, or simply NUTMEG. Appendix A gives a brief overview of NUTMEG and its features.

[1] Little did I know that I would later boldly enter the realm of five dimensions by extending whole-brain source localization methods to the time-frequency domain!

Chapter 2

Modified Beamformers for Coherent Source Region Suppression[1]

Abstract

Many tomographic source localization algorithms used in biomagnetic imaging assume, explicitly or sometimes implicitly, that the source activity at different brain locations are either independent or that the correlation structure between sources is known. Among these algorithms are a class of adaptive spatial filters known as beamformers, which have superior spatiotemporal resolution abilities. The performance of beamformers is robust to weakly coherent sources. However, these algorithms are extremely sensitive to the presence of strongly coherent sources. A

[1]This chapter originally appeared as an article in *IEEE Transactions on Biomedical Engineering* (Dalal et al., 2006)

frequent mode of failure in beamformers occurs with reconstruction of auditory evoked fields (AEFs), in which bilateral auditory cortices are highly coherent in their activation. Here, we present a novel beamformer that suppresses activation from regions with interfering coherent sources. First, a volume containing the interfering sources is defined. The lead field matrix for this volume is computed and reduced into a few significant columns using singular value decomposition (SVD). A vector beamformer is then constructed by rejecting the contribution of sources in the suppression region while allowing for source reconstruction at other specified regions. Performance of this algorithm was first validated with simulated data. Subsequent tests of this modified beamformer were performed on bilateral auditory evoked field (AEF) data. An unmodified vector beamformer using whole head coverage misplaces the source medially. After defining a suppression region containing the temporal cortex on one side, the described method consistently results in clear focal activations at expected regions of the contralateral superior temporal plane.

2.1 Introduction

Magnetoencephalography (MEG) is a functional neuroimaging technique with the ability to resolve brain dynamics on the order of milliseconds (Hämäläinen et al., 1993). In contrast to other techniques, MEG provides a direct measure of

the brain's neuronal activity that is relatively undistorted by the various tissue layers of the head (Hämäläinen and Sarvas, 1989). The potential for improved spatiotemporal reconstruction of neural activity has emerged with the advent of dense MEG sensor arrays with whole-head coverage.

Several source reconstruction algorithms, each employing a different set of assumptions, have been proposed to overcome the ill-posed inverse problem. Source reconstructions from MEG data can be classified as either parametric or tomographic. Parametric methods include equivalent current dipole (ECD) fitting techniques; they often require knowledge about the number of sources and their approximate locations, and poorly model sources with a large spatial extent. Tomographic methods reconstruct source activity at each voxel in the brain. It has been shown that a class of adaptive spatial filters known as beamformers (Van Veen and Buckley, 1988) have the best spatial resolution and performance amongst existing tomographic methods (Darvas et al., 2004). Beamformers avoid the high number of parameters and nonlinear nature of ECD analysis. Beamformers can also be used to perform time-frequency analysis and study oscillatory power changes of neural sources, which are difficult to reconstruct using parametric methods (Ishii et al., 1999; Taniguchi et al., 2000; Dalal et al., 2005).

However, the performance of beamformers degrades in the presence of highly correlated sources. For instance, the eigenspace beamformer is robust to moderate source correlations; however, sources that are strongly correlated ($\rho > 0.9$) are

poorly resolved (Sekihara et al., 2002a). Whole-head coverage increases the likelihood of encountering such a situation since bilateral activations are often strongly coherent. For example, beamformer reconstructions of auditory evoked fields (AEFs) commonly exhibit this failure, attenuating the two true sources from each primary auditory cortex and often erroneously placing a single low-amplitude source centered between them.

A partial solution to this problem is to process left temporal sensors separately from right temporal sensors; this method was first employed to overcome difficulties encountered with ECD methods (Pekkonen et al., 1995) and later applied to beamformers (Herdman et al., 2003). However, this method is not entirely satisfactory since it essentially discards most of the information gained from a whole-head sensor array; it also may not be sufficient for sources in closer proximity such as bilateral occipital activations evoked by visual stimuli or other more complex configurations.

We propose a modified beamformer method that circumvents these shortcomings by defining a region to ignore and augmenting the lead field matrix with this information. We demonstrate the efficacy of the proposed modified beamformer with simulations and real AEF data. Such a method improves upon the accuracy and resolution of beamforming.

Throughout this paper, plain italics indicate scalars, lowercase boldface italics indicate vectors, and uppercase boldface italics indicate matrices.

2.2 Method

2.2.1 Definitions and Problem Formulation

We shall define the magnetic field measured by the mth detector coil at time t as $b_m(t)$ and a column vector $\boldsymbol{b}(t) \equiv [b_1(t), b_2(t), \ldots, b_M(t)]^T$ as a set of measured data, where M is the total number of detector coils, and the superscript T indicates the matrix transpose. The spatial location is represented by a 3-D vector $\boldsymbol{r}$ such that $\boldsymbol{r} = (x, y, z)$. To express the moment magnitudes of the sources located at $\boldsymbol{r}$ at time t in the three orthogonal directions, we define $\boldsymbol{s}(\boldsymbol{r}, t) \equiv [s_x(\boldsymbol{r}, t), s_y(\boldsymbol{r}, t), s_z(\boldsymbol{r}, t)]^T$.

To express the orientation of the qth source, we define the angles between its moment vector and the x, y, and z axes as β_q^x, β_q^y, and β_q^z respectively. The orientation of the qth source is defined as a vector $\boldsymbol{\eta}_q \equiv [\beta_q^x, \beta_q^y, \beta_q^z]$. We assume in this paper that the orientation of each source is time independent.

The second-order moment matrix of the measurement is denoted $\boldsymbol{R}_b$, i.e., $\boldsymbol{R}_b = \langle \boldsymbol{b}(t)\boldsymbol{b}^T(t) \rangle$, where $\langle \cdot \rangle$ indicates the ensemble average. In practice, the ensemble average is often replaced with the time average over a certain time window. When $\langle \boldsymbol{b}(t) \rangle = 0$, $\boldsymbol{R}_b$ is also equal to the covariance matrix of the measurement.

The lead field vector for the μ component of a source at $\boldsymbol{r}$ is defined as $\boldsymbol{l}_\mu(\boldsymbol{r}) \equiv [l_1^\mu(\boldsymbol{r}), l_2^\mu(\boldsymbol{r}), \cdots, l_M^\mu(\boldsymbol{r})]^T$. Here, $l_m^\mu(\boldsymbol{r})$ expresses the mth sensor output induced by the unit-magnitude source that is located at $\boldsymbol{r}$ and oriented in the μ direction, where μ such that $\mu \in \{x, y, z\}$. We define the lead field matrix as

$\boldsymbol{L}(\boldsymbol{r}) \equiv [\boldsymbol{l}_x(\boldsymbol{r}), \boldsymbol{l}_y(\boldsymbol{r}), \boldsymbol{l}_z(\boldsymbol{r})]$, representing the sensitivity of the sensor array at $\boldsymbol{r}$ in all three orthogonal directions. Modeling the head as a spherical volume conductor reduces the lead field to two orthogonal components in spherical coordinates, θ and ϕ (Sarvas, 1987). In this case, the orientation of the qth source can instead be represented by a vector $\boldsymbol{\eta}_q = [\beta_q^\theta, \beta_q^\phi]^T$, resulting in $\boldsymbol{L}(\boldsymbol{r}) = [\boldsymbol{l}_\theta(\boldsymbol{r}), \boldsymbol{l}_\phi(\boldsymbol{r})]$.

2.2.2 Conventional Adaptive Spatial Filtering

An adaptive spatial filter estimate of the source moment matrix $\hat{\boldsymbol{s}}(\boldsymbol{r}, t)$ is given by:

$$\hat{\boldsymbol{s}}(\boldsymbol{r}, t) = \boldsymbol{W}^T(\boldsymbol{r})\boldsymbol{b}(t) \tag{2.1}$$

In the above equation, $\boldsymbol{W}(\boldsymbol{r}) \equiv [\boldsymbol{w}_\theta(\boldsymbol{r}), \boldsymbol{w}_\phi(\boldsymbol{r})]$ and $\hat{\boldsymbol{s}}(\boldsymbol{r}, t) \equiv [\hat{s}_\theta(\boldsymbol{r}, t), \hat{s}_\phi(\boldsymbol{r}, t)]^T$, where $\boldsymbol{w}_\theta(\boldsymbol{r})$ and $\boldsymbol{w}_\phi(\boldsymbol{r})$ are the weight vectors for the θ and ϕ directions, respectively, while $\hat{s}_\theta(\boldsymbol{r}, t)$ and $\hat{s}_\phi(\boldsymbol{r}, t)$ are the corresponding components of the source moment vector.

This section reviews an eigenspace-projected linearly constrained minimum variance vector (LCMV) beamformer (Sekihara et al., 2001; Van Veen et al., 1997). Omitting $\boldsymbol{r}$ from the expression, the weight vectors $\boldsymbol{w}_\theta$ and $\boldsymbol{w}_\phi$ are calculated with

the following constraints:

$$\begin{aligned}
&\min_{\boldsymbol{w}_\theta} \boldsymbol{w}_\theta^T \boldsymbol{R}_b \boldsymbol{w}_\theta \quad \text{subject to} \\
&\quad \boldsymbol{l}_\theta^T(\boldsymbol{r})\boldsymbol{w}_\theta = 1 \quad \text{and} \quad \boldsymbol{l}_\phi^T(\boldsymbol{r})\boldsymbol{w}_\theta = 0, \qquad (2.2) \\
&\min_{\boldsymbol{w}_\phi} \boldsymbol{w}_\phi^T \boldsymbol{R}_b \boldsymbol{w}_\phi \quad \text{subject to} \\
&\quad \boldsymbol{l}_\theta^T(\boldsymbol{r})\boldsymbol{w}_\phi = 0 \quad \text{and} \quad \boldsymbol{l}_\phi^T(\boldsymbol{r})\boldsymbol{w}_\phi = 1. \qquad (2.3)
\end{aligned}$$

The solution is known to be (Van Veen et al., 1997):

$$\boldsymbol{W}_{mv}(\boldsymbol{r}) = [\boldsymbol{L}^T(\boldsymbol{r})\boldsymbol{R}_b^{-1}\boldsymbol{L}(\boldsymbol{r})]^{-1}\boldsymbol{R}_b^{-1}\boldsymbol{L}(\boldsymbol{r}). \qquad (2.4)$$

An eigenspace-projected minimum variance beamformer is obtained by projecting the weight matrix of the LCMV beamformer onto the signal subspace of the measurement covariance matrix:

$$\begin{aligned}
\boldsymbol{W}_E(\boldsymbol{r}) &= \boldsymbol{E}_S \boldsymbol{E}_S^T \boldsymbol{W}_{mv}(\boldsymbol{r}) \\
&= \boldsymbol{E}_S \boldsymbol{E}_S^T [\boldsymbol{L}^T(\boldsymbol{r})\boldsymbol{R}_b^{-1}\boldsymbol{L}(\boldsymbol{r})]^{-1}\boldsymbol{R}_b^{-1}\boldsymbol{L}(\boldsymbol{r})
\end{aligned} \qquad (2.5)$$

where $\boldsymbol{E}_S$ contains the eigenvectors representing the signal subspace of $\boldsymbol{R}_b$. This eigenspace projection overcomes the SNR degradation caused by array mismatch and smoothes time courses of source reconstruction (Sekihara et al., 2001).

2.2.3 Proposed Adaptive Beamformer with Coherent Suppression

A Method for Point Source Interference Suppression

The LCMV formulation allows one to add additional null constraints to suppress the influence of correlated sources. If the exact location of an interfering source is known to be at point $\boldsymbol{r}_i$, then the weight matrix can be reformulated:

$$\begin{aligned} &\min_{\boldsymbol{w}_\theta} \boldsymbol{w}_\theta^T \boldsymbol{R}_b \boldsymbol{w}_\theta \quad \text{subject to} \\ &\qquad \boldsymbol{l}_\theta^T(\boldsymbol{r})\boldsymbol{w}_\theta = 1, \quad \boldsymbol{l}_\phi^T(\boldsymbol{r})\boldsymbol{w}_\theta = 0, \\ &\qquad \boldsymbol{l}_\phi^T(\boldsymbol{r}_i)\boldsymbol{w}_\theta = 0, \quad \boldsymbol{l}_\theta^T(\boldsymbol{r}_i)\boldsymbol{w}_\theta = 0. \end{aligned} \tag{2.6}$$

Similarly, for the orthogonal orientation ϕ:

$$\begin{aligned} &\min_{\boldsymbol{w}_\phi} \boldsymbol{w}_\phi^T \boldsymbol{R}_b \boldsymbol{w}_\phi \quad \text{subject to} \\ &\qquad \boldsymbol{l}_\theta^T(\boldsymbol{r})\boldsymbol{w}_\phi = 0, \quad \boldsymbol{l}_\phi^T(\boldsymbol{r})\boldsymbol{w}_\phi = 1, \\ &\qquad \boldsymbol{l}_\phi^T(\boldsymbol{r}_i)\boldsymbol{w}_\phi = 0, \quad \boldsymbol{l}_\theta^T(\boldsymbol{r}_i)\boldsymbol{w}_\phi = 0. \end{aligned} \tag{2.7}$$

Therefore, the standard composite lead field matrix may be augmented with additional columns:

$$\boldsymbol{L}_{ps}(\boldsymbol{r}) = [\boldsymbol{l}_\theta(\boldsymbol{r}), \boldsymbol{l}_\phi(\boldsymbol{r}), \boldsymbol{l}_\theta(\boldsymbol{r}_i), \boldsymbol{l}_\phi(\boldsymbol{r}_i)], \tag{2.8}$$

resulting in a new weight matrix formulation:

$$\boldsymbol{W}_{ps}(\boldsymbol{r}) = [\boldsymbol{L}_{ps}^T(\boldsymbol{r})\boldsymbol{R}_b^{-1}\boldsymbol{L}_{ps}(\boldsymbol{r})]^{-1}\boldsymbol{R}_b^{-1}\boldsymbol{L}_{ps}(\boldsymbol{r}) \tag{2.9}$$

A Method for Region Suppression

However, the precise location of interference is seldom known a priori. Nevertheless, in many cases, an interfering source can safely be presumed to originate from somewhere within a larger brain region. For example, in auditory MEG experiments, interfering sources are typically present in superior temporal areas contralateral to the region of interest. It is therefore desirable to extend this formulation to suppress a selected region suspected to contain an interfering source.

In order to accomplish this, the lead field of the desired suppression region may be added to the null constraint of the weight matrix computation. As with a single point, the lead field matrix is augmented with the contribution from each voxel in the desired suppression region, Σ:

$$\min_{\boldsymbol{w}_\theta} \boldsymbol{w}_\theta^T \boldsymbol{R}_b \boldsymbol{w}_\theta \quad \text{subject to}$$

$$\boldsymbol{l}_\theta^T(\boldsymbol{r})\boldsymbol{w}_\theta = 1, \quad \boldsymbol{l}_\phi^T(\boldsymbol{r})\boldsymbol{w}_\theta = 0, \quad \text{and} \quad \boldsymbol{C}_\Sigma^T \boldsymbol{w}_\theta = 0, \tag{2.10}$$

where Σ is composed of the points $\{\boldsymbol{r}_{\Sigma_1}, \boldsymbol{r}_{\Sigma_2}, \cdots, \boldsymbol{r}_{\Sigma_N}\}$ and $\boldsymbol{C}_\Sigma \equiv [\boldsymbol{l}_\theta(\boldsymbol{r}_{\Sigma_1}), \boldsymbol{l}_\phi(\boldsymbol{r}_{\Sigma_1}), \cdots, \boldsymbol{l}_\theta(\boldsymbol{r}_{\Sigma_N}), \boldsymbol{l}_\phi(\boldsymbol{r}_{\Sigma_N})]$. Again, for orientation ϕ:

$$\min_{\boldsymbol{w}_\phi} \boldsymbol{w}_\phi^T \boldsymbol{R}_b \boldsymbol{w}_\phi \quad \text{subject to}$$

$$\boldsymbol{l}_\theta^T(\boldsymbol{r})\boldsymbol{w}_\phi = 0, \quad \boldsymbol{l}_\phi^T(\boldsymbol{r})\boldsymbol{w}_\phi = 1, \quad \text{and} \quad \boldsymbol{C}_\Sigma^T \boldsymbol{w}_\phi = 0. \tag{2.11}$$

Then, defining $\boldsymbol{L}_{rs}(\boldsymbol{r}) \equiv [\boldsymbol{l}_\theta(\boldsymbol{r}), \boldsymbol{l}_\phi(\boldsymbol{r}), \boldsymbol{C}_\Sigma]$, the weight matrix retains a familiar form:

$$\boldsymbol{W}_{rs}(\boldsymbol{r}) = [\boldsymbol{L}_{rs}^T(\boldsymbol{r})\boldsymbol{R}_b^{-1}\boldsymbol{L}_{rs}(\boldsymbol{r})]^{-1}\boldsymbol{R}_b^{-1}\boldsymbol{L}_{rs}(\boldsymbol{r}). \tag{2.12}$$

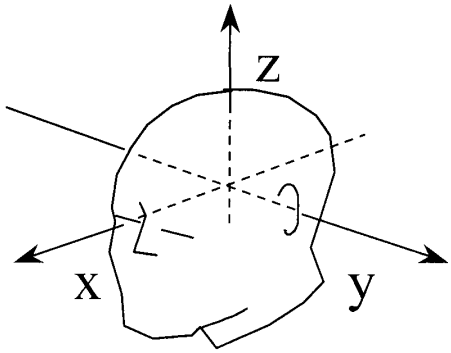

Figure 2.1 The x, y, and z coordinates used to express the reconstruction results in Section 2.4. The midpoint between the left and right preauricular points was defined as the coordinate origin. The axis directed away from the origin to the left preauricular point was defined as the $+y$ axis, and that from the origin to the nasion was the $+x$ axis. The $+z$ axis was defined as the axis perpendicular to both these axes and was directed from the origin toward the vertex.

In practice, Σ will consist of several thousand voxels, making the product $\boldsymbol{L}_{rs}^{T}(\boldsymbol{r})\boldsymbol{R}_{b}^{-1}\boldsymbol{L}_{rs}(\boldsymbol{r})$ a highly singular matrix and therefore difficult to invert accurately. Furthermore, each additional column increases the computational load proportionately. To remedy these two problems, singular value decomposition (SVD) may be applied to $\boldsymbol{C}_{\Sigma}$; the most significant components can then be chosen to limit the number of additional columns and improve the condition number of this matrix. This has the added benefit of allowing the suppression region to be sampled at a different spatial resolution from the region of interest; a coarser suppression grid would be more computationally efficient without significantly compromising accuracy.

Let us define $\boldsymbol{C}_S$ such that $\boldsymbol{C}_S \equiv [\boldsymbol{c}_1, \cdots, \boldsymbol{c}_P]$, the P left singular vectors of $\boldsymbol{C}_{\Sigma}$, and $\widetilde{\boldsymbol{L}}_{rs}(\boldsymbol{r}) \equiv [\boldsymbol{l}_{\theta}(\boldsymbol{r}), \boldsymbol{l}_{\phi}(\boldsymbol{r}), \boldsymbol{C}_S]$. Then, building on the full eigenspace-projection

beamformer, we construct an orthonormal basis $\widetilde{\boldsymbol{E}}_S$ by performing Gram-Schmidt orthogonalization on the composite matrix $[\boldsymbol{E}_S, \boldsymbol{C}_S]$. Finally, substituting $\widetilde{\boldsymbol{E}}_S$ for $\boldsymbol{E}_S$ from equation 2.5, and $\widetilde{\boldsymbol{L}}_{rs}(\boldsymbol{r})$ for $\boldsymbol{L}_{rs}(\boldsymbol{r})$ from equation 2.12, we obtain:

$$\widetilde{\boldsymbol{W}}_{rs}(\boldsymbol{r}) = \widetilde{\boldsymbol{E}}_S \widetilde{\boldsymbol{E}}_S^T [\widetilde{\boldsymbol{L}}_{rs}^T(\boldsymbol{r}) \boldsymbol{R}_b^{-1} \widetilde{\boldsymbol{L}}_{rs}(\boldsymbol{r})]^{-1} \boldsymbol{R}_b^{-1} \widetilde{\boldsymbol{L}}_{rs}(\boldsymbol{r}) \tag{2.13}$$

We use the first two columns of $\boldsymbol{W}_{rs}(\boldsymbol{r})$ as $\boldsymbol{w}_\theta(\boldsymbol{r})$ and $\boldsymbol{w}_\phi(\boldsymbol{r})$. That is, defining $p+2$ dimensional column vectors $\boldsymbol{f}_1$ and $\boldsymbol{f}_2$ such that

$$\boldsymbol{f}_1 = [1, 0, 0, \ldots, 0]^T \quad \text{and} \quad \boldsymbol{f}_2 = [0, 1, 0, \ldots, 0]^T,$$

the weight vectors, $\boldsymbol{w}_\theta(\boldsymbol{r})$ and $\boldsymbol{w}_\phi(\boldsymbol{r})$, are obtained using

$$\boldsymbol{w}_\theta(\boldsymbol{r}) = \boldsymbol{W}_{rs}(\boldsymbol{r}) \boldsymbol{f}_1 \quad \text{and} \quad \boldsymbol{w}_\phi(\boldsymbol{r}) = \boldsymbol{W}_{rs}(\boldsymbol{r}) \boldsymbol{f}_2. \tag{2.14}$$

The normalized lead field matrix $\widetilde{\boldsymbol{L}}_{rs}(\boldsymbol{r}) / \|\widetilde{\boldsymbol{L}}_{rs}(\boldsymbol{r})\|$ may be used to prevent erroneous values near the local sphere origin (Van Veen et al., 1997; Gross and Ioannides, 1999).

2.3 Numerical Experiments

2.3.1 Data Generation

A series of numerical experiments were conducted to test the effectiveness of the proposed method. The sensor configuration of the 275-channel CTF Omega 2000 biomagnetic measurement system (VSM MedTech, Coquitlam, BC, Canada)

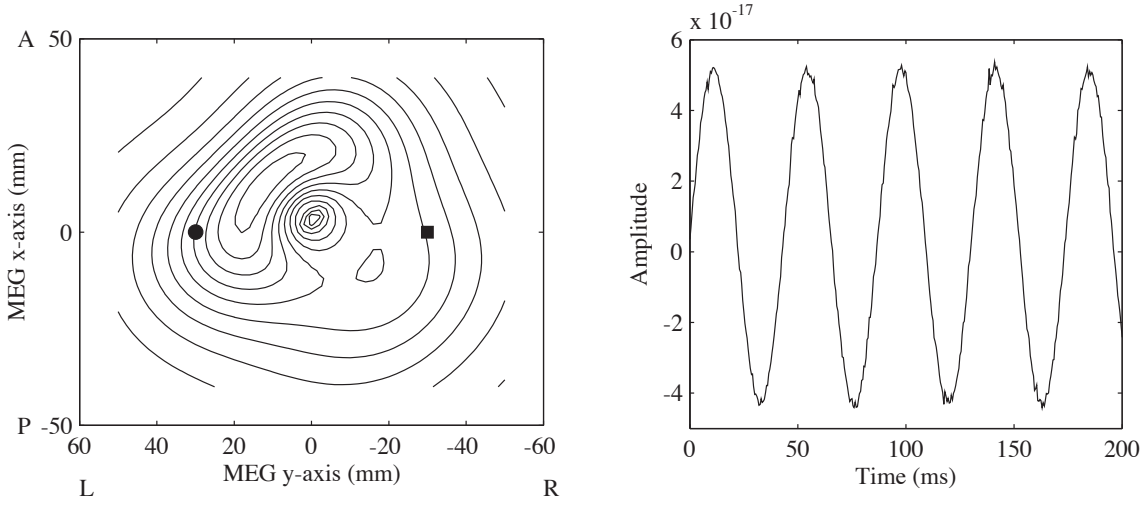

Figure 2.2 Above left, the reconstruction profile on the $z = 40$ mm plane, using the conventional beamformer. The circle and square indicate the locations of the two simulated coherent sources. At right, the time series associated with the spatial peak at $(8.0, 6.0, 40.0)$ mm.

was used. Data were simulated and processed using a development version of NUTMEG (Dalal et al., 2004).

Two identical synchronous sine wave sources were synthesized and placed at $(0, 30, 40)$ mm and $(0, -30, 40)$ mm, with coordinates defined as in Figure 2.1. A sensor lead field was calculated using a single-layer spherical volume conductor as the forward model (Sarvas, 1987) and the Omega 2000's sensor geometry, with 2 mm grid spacing. Gaussian white noise was added to the generated data such that the signal-to-noise (SNR) was equal to 2. The SNR was defined as the ratio of the Frobenius norm of the MEG data matrix to that of the noise matrix.

The conventional beamformer erroneously placed a diffuse "source" centered at $(8.0, 6.0, 40.0)$ mm, shown in Figure 2.2. Note also the corresponding time course

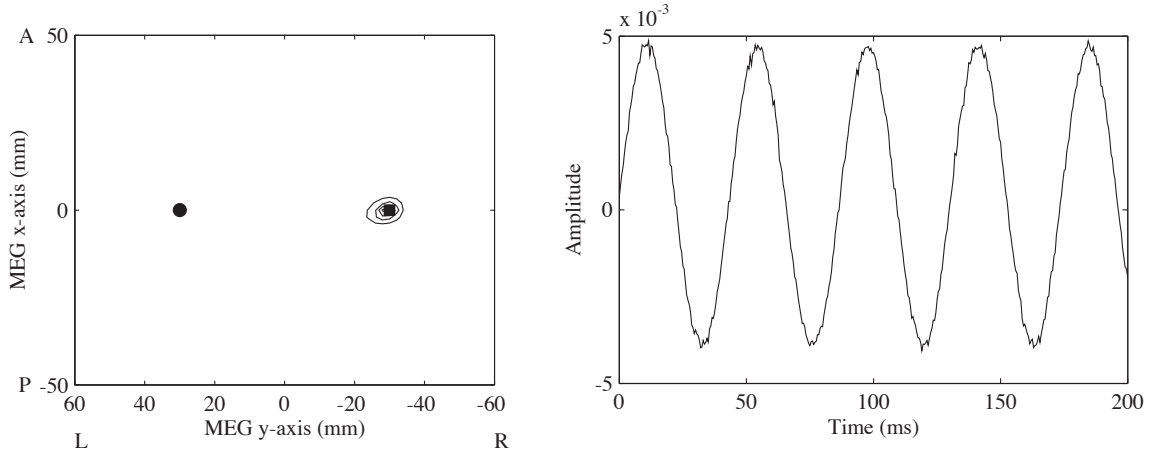

Figure 2.3 Above left, the reconstruction profile on the $z = 40$ mm plane, using the beamformer with the point suppression modification and the same simulated data as in Figure 2.2. The left source was suppressed, perfectly reconstructing the right source. At right, the time series reconstructed for the right source.

does not show discernible distortion or other indications of an inaccurate reconstruction, and can be misleading in applications to real data. Applying point suppression to the coordinates of one source resulted in a highly focal and accurate reconstruction of the other source (Figure 2.3).

Next, we synthesized a total of six sine wave sources to test the region-based suppression technique. Four of these sources were synchronous, while the other two had different frequencies and phases. As expected, the conventional beamformer reconstructs the two unique sources, but fails to resolve any of the four correlated sources (Figure 2.4). A suppression region was defined covering three of the four correlated sources, leaving three sources in the region of interest; the region was $80 \times 40 \times 20$ mm. The eigenspectrum of this region's lead field is shown in Figure 2.5(a). Choosing eigenvectors that represent 95% of the variance is gen-

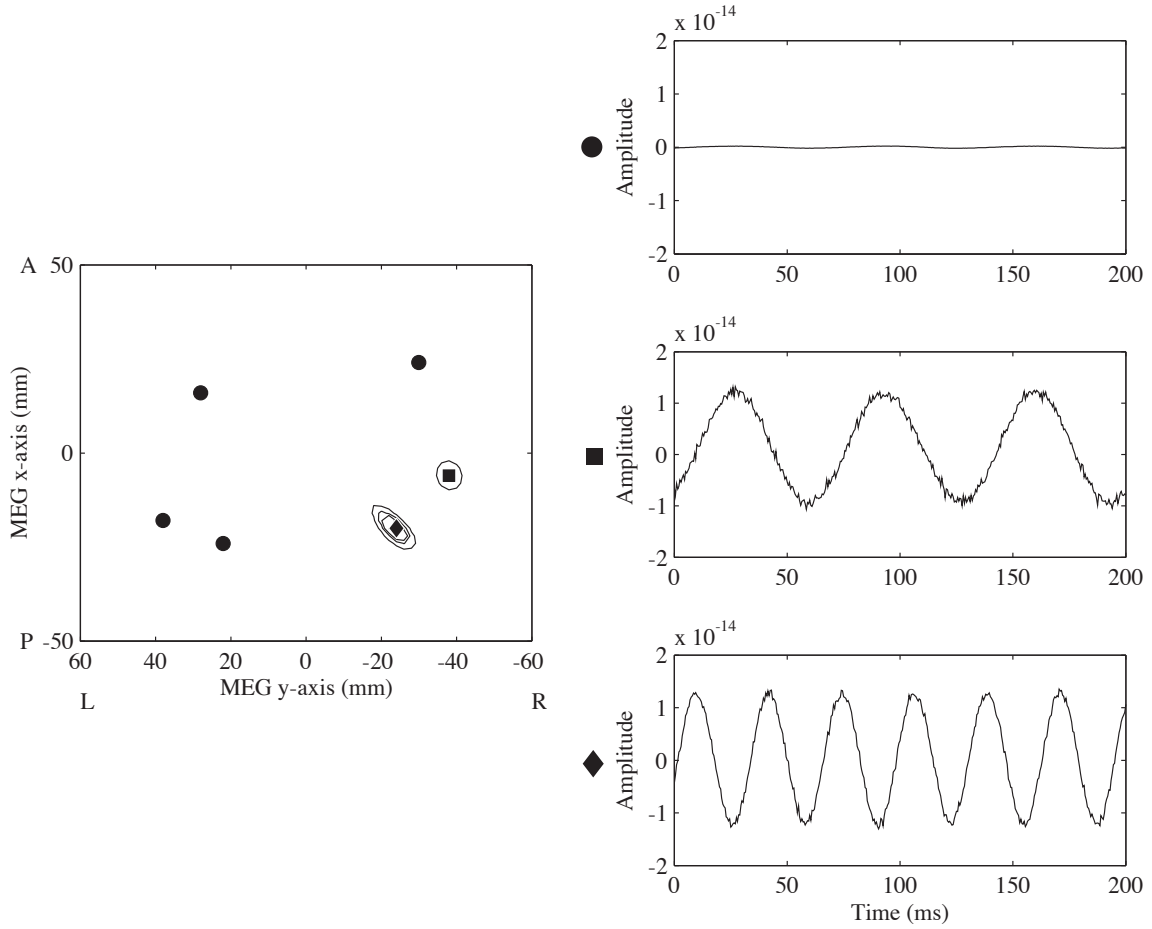

Figure 2.4 The reconstruction profile and time courses obtained from six simulated sources, four of which are coherent (indicated by circles) and two of which are uncorrelated (indicated by the square and the diamond). None of the four coherent sources are resolved.

erally acceptable; however, often the precise eigenvalue thresholding is apparent by inspection. In this case, the first 13 eigenvectors, representing 93% of the variance, were chosen to augment the lead field of the reconstruction region as a null constraint. As shown in Figure 2.5(b), all three sources of interest were resolved; the peak of the reconstructed correlated source had a localization error of 4.9 mm (approximately two voxels), while the other two were reconstructed perfectly with no localization error.

The size of the pseudosignal subspace represented by $\widetilde{\boldsymbol{E}}_s$ is greater than the true signal subspace $\boldsymbol{E}_s$, hence a small increase in noise was observed in the reconstructed time series. To assess how noise is affected by the chosen eigenvectors, the mean square errors (MSE) of the time courses were calculated for several choices (see Figure 2.6). As expected, the MSE of the time course for the correlated source reduced with more eigenvalues, leveling off at approximately 13. The error of one uncorrelated source increased slightly with more eigenvalues, while the other remained fairly constant.

To assess how well an interfering source is suppressed depending on its position within the suppression region, we returned to the case of two synchronous sine wave sources. Using the left hemisphere suppression region defined above, one source was fixed at $(0, -30, 40)$ mm, while the algorithm was evaluated with the other source at each of 190 locations throughout the suppression region. Figure 2.7 shows the localization error of the source of interest as a function of the

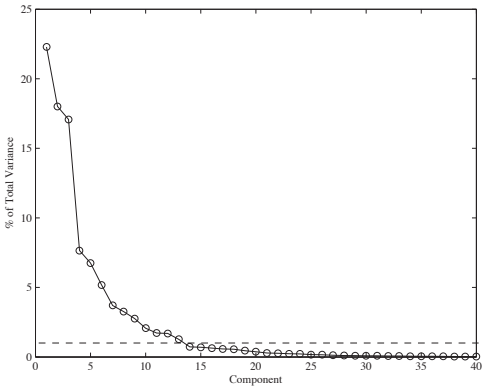

(a)

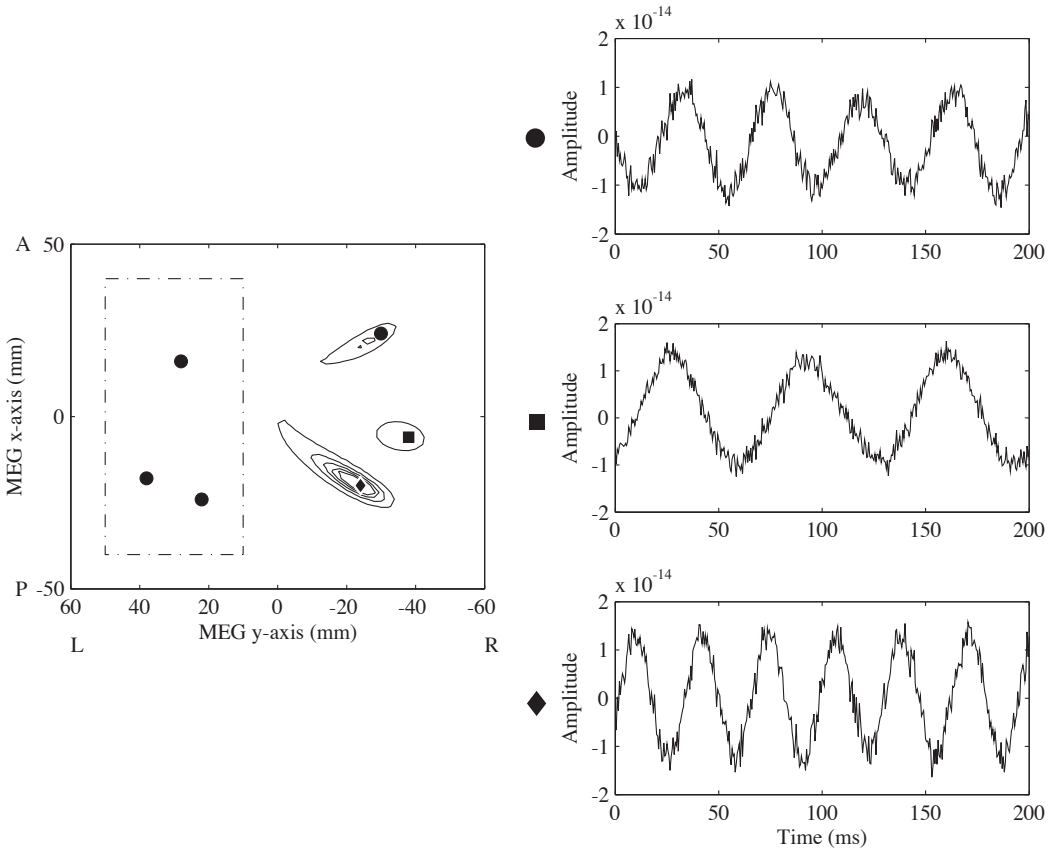

(b)

Figure 2.5 (a) Eigenspectrum of the lead field of the suppression region. 13 eigenvalues, accounting for 93% of the total variance, were chosen by inspection. (b) The reconstruction profile and time courses obtained when defining the boxed area as the suppression region. The four circles indicate the coherent sources, while the sources indicated by the square and diamond are uncorrelated.

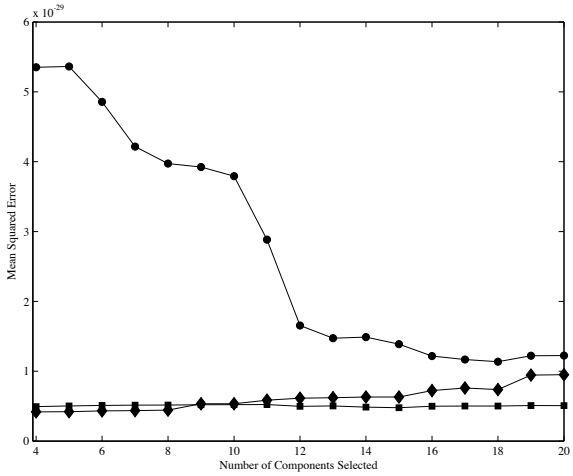

Figure 2.6 Mean squared error of the time courses of the three sources as a function of eigenvector components selected for the lead field of the suppression region. The circles, diamonds, and squares correspond to the sources in Figures 2.4 and 2.5.

interfering source within the suppression region. The mean error was 4.8 mm, with 73% of locations within the suppression region yielding reconstruction errors of 5 mm or less. Interfering sources placed within 5 mm of the edges farthest from the model sphere center produced the largest errors of up to 20 mm.

2.4 Application to Auditory-Evoked MEG Data

In order to apply our proposed technique to real data, auditory evoked field data was acquired from a 24-year-old female using pure tones. Data was acquired with a 275-channel whole-head MEG device from CTF Systems (VSM MedTech, Coquitlam, BC, Canada). The recordings were collected in accordance with the ethical standards of the UCSF Institutional Review Board and Helsinki Declaration of 1975, as revised in 1983. The auditory stimuli consisted of 1 kHz pure tones of

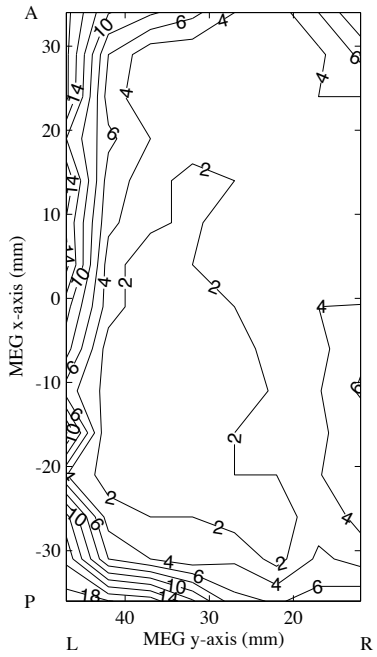

Figure 2.7 Contour map showing reconstruction error (mm) of right source as a function of position of left source within suppression region.

400 ms duration. The interstimulus interval was randomly varied between 1.5–1.6 s. The sampling frequency was set at 1200 Hz. All post-processing and analysis were performed using a development version of NUTMEG (Dalal et al., 2004). A digital filter was used to highpass the data at 1 Hz. After visual rejection of trials containing eyeblink and movement artifacts, a total of 112 trials were averaged (Figure 2.8).

Source reconstruction using a standard eigenspace vector beamformer with the full 275 channel array shows a failure typical of simultaneous bilateral activation, placing a low-amplitude, diffuse source bleeding towards the center of the model sphere (Figure 2.9(a)). For this reconstruction, the signal subspace dimension Q

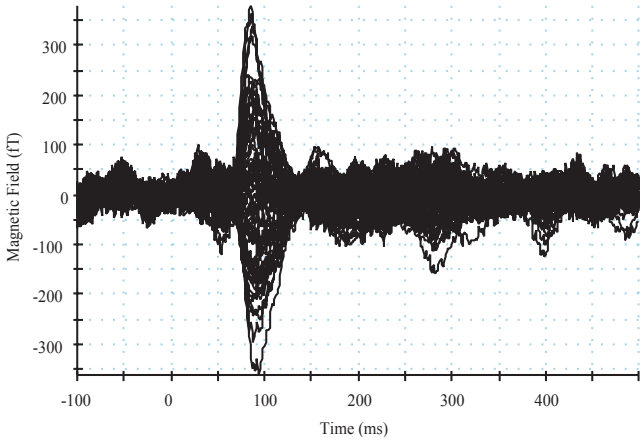

Figure 2.8 A bilateral AEF response to a 1 kHz pure tone, with data from sensors over the left and right temporal cortices overlaid.

was set to two because the eigenspectrum showed two dominant eigenvalues. Note that the reconstructed time series appears to be reasonable and does not show obvious symptoms of failure.

Applying the proposed technique, we used all 275 channels and defined the suppression region to be a broad volume ($75 \times 40 \times 65$ mm) containing right temporal areas. We then projected the lead field of the suppression region onto the 13 dominant eigenvectors and completed source reconstruction. As shown in Figure 2.9(b), a plausible location for left primary auditory cortex on the superior temporal plane clearly emerges. Similarly, selecting a similar suppression region containing left temporal areas results in a peak at a plausible location for right primary auditory cortex (Figure 2.9(c)). Furthermore, no spurious activations near the center of the model sphere were observed. The correlation coefficient between the reconstructed time series for the two peaks was observed to be 0.90.

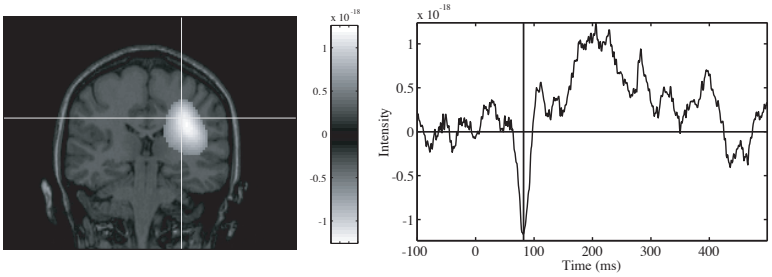

(a)

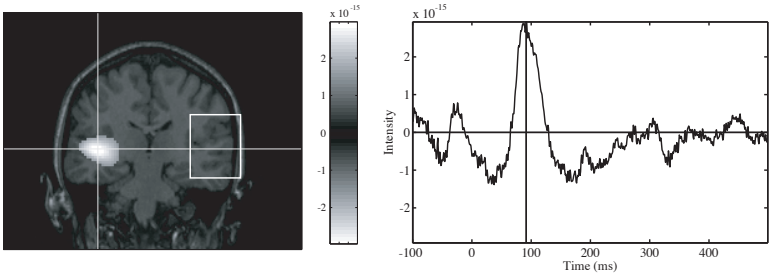

(b)

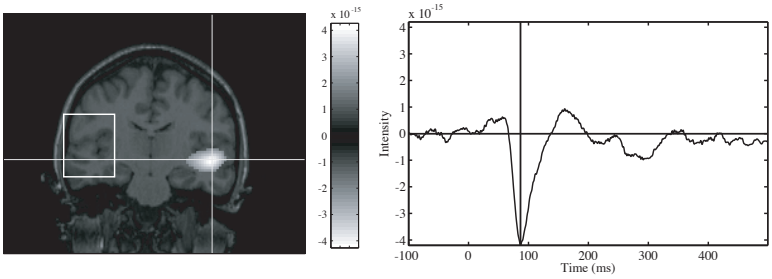

(c)

Figure 2.9 (a) Conventional beamformer reconstruction of AEF data, exhibiting failure due to correlated sources. The algorithm reconstructs a false source, placed in the frontal lobe, superior and anterior to the expected location on the superiotemporal plane. The spatial activation shown is at full width half maximum (FWHM). The time course shown is for the spatial peak marked by the crosshairs. (b) Reconstruction of AEF data with suppression of the outlined region (left temporal cortex). Right auditory cortex is revealed, along with its time course. (c) Similarly, region suppression of right temporal cortex reveals left auditory cortex.

For comparison, the data were also fit to a spatiotemporal ECD model with DipoleFit (VSM MedTech, Coquitlam, BC, Canada). Using the same single-sphere head model as the beamformer analyses, two dipoles were fit simultaneously over the interval 75 ms to 100 ms, achieving a total weighted error of 9.8%. The left dipole localized 12.5 mm lateral and inferior to the left source reconstructed by the modified beamformer, while the right dipole localized 6.4 mm superior and slightly medial to the reconstructed right source. Both of these locations were within the full-width at half-maximum (FWHM) of each peak of the modified beamformer. The correlation coefficient between the two dipole moments was 0.93.

2.5 Conclusion

Adaptive beamformers have been shown to have zero bias and the highest spatial resolution amongst various spatial filtering methods used in neuromagnetic source reconstruction (Sekihara et al., 2005b). However, the accurate resolution of highly correlated sources has been problematic for beamformer techniques. One workaround has been to simply process different sensor groups independently, especially for auditory experiments. While such results may be satisfactory for some situations, this method likely will not be sufficient for correlated sources that are in the same hemisphere or otherwise closer together. Hence, highly correlated visual or somatosensory activity may not be accurately resolved by simply ignoring

distant sensors.

The described method for suppressing regions of coherent activation is an important development for MEG inverse techniques. We have presented a modification that solves the problem of coherent sources when the approximate region of one source is known and disjoint from the other. This method essentially allows for a specific exception to the assumption of independent sources commonly made in beamformer reconstructions. Thus, simultaneous bilateral activations may now be accurately reconstructed using this technique without discarding any channels. It may also provide a solution in the case of highly correlated sources located in the same hemisphere or otherwise close to each other.

While the manual selection of the suppression region is a drawback of the method proposed here, the suppression region can be defined with the aid of a priori knowledge, potentially including information from fMRI studies. It may also be possible to automate the selection through a method that scans through several potential suppression regions.

Acknowledgments

Special thanks to co-author Kensuke Sekihara for his collaboration on this project. The authors would like to thank Anne Findlay and Susanne Honma for their assistance in acquiring MEG data, as well as Johanna Zumer and Kenneth Hild for helpful discussions.

Chapter 3

Five-Dimensional Neuroimaging: Localization of the Time-Frequency Dynamics of Cortical Activity

Abstract

The spatiotemporal dynamics of cortical oscillations across human brain regions remain poorly understood because of a lack of adequately validated methods for reconstructing such activity from noninvasive electrophysiological data. In this paper, we present a novel adaptive spatial filtering algorithm optimized for robust source time-frequency reconstruction from magnetoencephalography (MEG) and electroencephalography (EEG) data. The efficacy of the method is demon-

strated with simulated sources and is also applied to real MEG data from a self-paced finger movement task. The algorithm reliably reveals modulations both in the beta band (12–30 Hz) and high gamma band (65–90 Hz) in sensorimotor cortex. The performance is validated by both across-subjects statistical comparisons and by intracranial electrocorticography (ECoG) data from two epilepsy patients. Interestingly, we also reliably observed high frequency activity (30–300 Hz) in the cerebellum, though with variable locations and frequencies across subjects. The proposed algorithm is highly parallelizable and runs efficiently on modern high performance computing clusters. This method enables and optimizes the ultimate promise of MEG and EEG for five-dimensional imaging of space, time, and frequency activity in the brain and renders it applicable for widespread studies of human cortical dynamics during cognition.

3.1 Introduction

Magnetoencephalography (MEG) and electroencephalography (EEG) are functional neuroimaging techniques with millisecond time resolution (Hämäläinen et al., 1993). Traditionally, MEG and EEG have been used to study *evoked responses*, i.e., activity that is both time-locked and phase-locked to a stimulus or task. These analyses assume a model of neural activity in which responses are additive and/or phases are reset (Hanslmayr et al., 2007). However, it has been

well-known that ongoing MEG/EEG oscillations can be suppressed in response to a stimulus or task since the earliest EEG research (Berger, 1930); this possibility is not accounted for by the evoked model. Furthermore, the across-trial jitter inherent in responses to even simple stimuli have been shown to be sufficient to markedly reduce the amplitude of averaged responses (Michalewski et al., 1986); this effect becomes even more pronounced for higher frequency bands. Averaging also assumes trial-to-trial phase locking, which may not be valid for many complex cognitive paradigms.

Another approach to interpreting MEG and EEG data is to quantify oscillatory aspects of the signals using time-frequency methods. Typically, modulations of oscillatory activity are described as event-related spectral power changes (Pfurtscheller and Aranibar, 1977; Pfurtscheller and Neuper, 1992; Makeig, 1993). By comparing the power of neural activity to a quiescent baseline, these types of analyses reveal *induced responses*, i.e., activity that is time-locked but not necessarily phase-locked. Additionally, the power change may be negative, termed an *event-related desynchronization* (ERD), or positive, termed an *event-related synchronization* (ERS). Analyses of ERD and ERS overcome many of the limitations of evoked response analyses. However, most MEG/EEG time-frequency analyses are conducted on the sensor signals without source localization, providing only vague information as to which brain structures generated the activity of interest.

Several source reconstruction algorithms, each employing a different set of as-

sumptions, have been proposed to overcome the ill-posed inverse problem. Source reconstructions from MEG data can be classified as either parametric or tomographic. Parametric methods include equivalent current dipole (ECD) fitting techniques; they often require knowledge about the number of sources and their approximate locations and poorly model sources with a large spatial extent.

Tomographic methods reconstruct source activity at each voxel (3-D location) in the brain. Spatial filtering techniques avoid the high number of parameters and the nonlinear iterative search required by ECD analysis. Nonadaptive spatial filtering techniques, which include minimum-norm-based methods such as sLORETA (Pascual-Marqui, 2002), use sensor geometry to construct the weights for the spatial filter. Adaptive techniques, on the other hand, additionally use sensor data to create a custom filter depending on signal characteristics. It has been shown that a class of adaptive spatial filters known as beamformers (Van Veen and Buckley, 1988) have the best spatial resolution and performance amongst existing tomographic methods (Darvas et al., 2004; Sekihara et al., 2005b).

Adaptive spatial filtering methods have the potential to compute electromagnetic source images in both the time and frequency domains (Robinson and Vrba, 1999; Gross et al., 2001; Sekihara et al., 2001; Dalal et al., 2004). Techniques such as the synthetic aperture magnetometry (SAM) beamformer have been employed to examine either the time course of neural sources or the spatial distribution of power within a specific frequency band (Robinson and Vrba, 1999). However, pub-

lished studies typically employ SAM to generate static fMRI-style images using a large bandwidth and wide time window—effectively discarding the temporal resolution advantage of magnetoencephalography. Only a few studies have attempted time-frequency analysis in source space (Singh et al., 2002; Cheyne et al., 2003; Gaetz and Cheyne, 2006; Jurkiewicz et al., 2006). These reports describe a method in which a single set of beamformer weights are first computed over a wide time window and frequency range; time-frequency decompositions are then computed from the reconstructed time series for a few locations of interest. However, as we show in this paper, weights computed from unfiltered or wideband data may be inherently biased towards resolving low-frequency brain activity due to the power law of typical electrophysiological data. Additionally, responses of shorter duration or outside the fixed time window used to generate the weights may not be adequately captured.

In this paper, we propose a novel adaptive spatial filtering algorithm that is optimized for time-frequency source reconstructions from MEG/EEG data. Performance of this algorithm will first be evaluated with simulated data. Then we will demonstrate the method with real finger movement data, validated with group statistics and intracranial recordings. The proposed algorithm enables accurate reconstruction of five-dimensional brain activity from MEG and EEG data, thereby realizing the ultimate promise of MEG- and EEG-based neuroimaging.

3.2 Methods

3.2.1 Definitions and Problem Formulation

Throughout this paper, plain italics indicate scalars, lower-case boldface italics indicate vectors, and uppercase boldface italics indicate matrices.

We define the magnetic field measured by the mth detector coil at time t as $b_m(t)$ and a column vector $\boldsymbol{b}(t) \equiv [b_1(t), b_2(t), \ldots, b_M(t)]^T$ as a set of measured data, where M is the total number of detector coils and the superscript T indicates the matrix transpose. The second-order moment matrix of the measurement is denoted $\boldsymbol{R}$, i.e., $\boldsymbol{R} \equiv \langle \boldsymbol{b}(t)\boldsymbol{b}^T(t) \rangle$, where $\langle \cdot \rangle$ indicates the ensemble average over trials. When $\langle \boldsymbol{b}(t) \rangle = 0$, $\boldsymbol{R}$ is also equal to the covariance matrix of the measurement. In practice, the ensemble average is often replaced with the time average over a certain time window, $\boldsymbol{t}$, such that $\boldsymbol{R}(\boldsymbol{t}) \equiv \langle \boldsymbol{b}(\boldsymbol{t})\boldsymbol{b}^T(\boldsymbol{t}) \rangle$.

We assume that the sensor data arises from elemental dipoles at each spatial location $\boldsymbol{r}$, represented by a 3-D vector such that $\boldsymbol{r} = (r_x, r_y, r_z)$. The orientation of each source is defined as a vector $\boldsymbol{\eta}(\boldsymbol{r}) \equiv [\beta^x, \beta^y, \beta^z]$, where β^x, β^y, and β^z are the angles between the moment vector of the source and the x, y, and z axes, respectively.

We define $l_m^\zeta(\boldsymbol{r})$ as the output of the mth sensor that would be induced by a unit-magnitude source located at $\boldsymbol{r}$ and pointing in the ζ direction. The column vector $\boldsymbol{l}_\zeta(\boldsymbol{r})$ is defined as $\boldsymbol{l}_\zeta(\boldsymbol{r}) \equiv [l_1^\zeta(\boldsymbol{r}), l_2^\zeta(\boldsymbol{r}), \cdots, l_M^\zeta(\boldsymbol{r})]^T$. The lead field matrix,

which represents the sensitivity of the whole sensor array at $\boldsymbol{r}$, is defined as $\boldsymbol{L}(\boldsymbol{r}) \equiv [\boldsymbol{l}_x(\boldsymbol{r}), \boldsymbol{l}_y(\boldsymbol{r}), \boldsymbol{l}_z(\boldsymbol{r})]$. The lead field vector for a unit-dipole oriented in the direction $\boldsymbol{\eta}$ is defined as $\boldsymbol{l}(\boldsymbol{r}, \boldsymbol{\eta})$ where $\boldsymbol{l}(\boldsymbol{r}, \boldsymbol{\eta}) \equiv \boldsymbol{L}(\boldsymbol{r})\boldsymbol{\eta}(\boldsymbol{r})$.

3.2.2 Conventional Adaptive Spatial Filtering

This section reviews an adaptive spatial filter called the minimum variance (MV) scalar beamformer, also referred to as the synthetic aperture magnetometry (SAM) beamformer (Robinson and Vrba, 1999). An adaptive spatial filter estimate of the source moment $\hat{s}(\boldsymbol{r}, t)$ is given by

$$\hat{s}(\boldsymbol{r}, t) = \boldsymbol{w}^T(\boldsymbol{r})\boldsymbol{b}(t) \tag{3.1}$$

where $\boldsymbol{w}(\boldsymbol{r})$ is the weight vector.

The MV scalar beamformer weight vector $\boldsymbol{w}(\boldsymbol{r})$ is calculated by minimizing $\boldsymbol{w}^T(\boldsymbol{r})\boldsymbol{R}(\boldsymbol{t})\boldsymbol{w}(\boldsymbol{r})$ subject to $\boldsymbol{l}^T(\boldsymbol{r}, \boldsymbol{\eta})\boldsymbol{w}(\boldsymbol{r}) = 1$. The solution is known to be (Robinson and Vrba, 1999):

$$\boldsymbol{w}(\boldsymbol{r}) = \frac{\boldsymbol{R}^{-1}(\boldsymbol{t})\boldsymbol{l}(\boldsymbol{r}, \boldsymbol{\eta})}{\boldsymbol{l}^T(\boldsymbol{r}, \boldsymbol{\eta})\boldsymbol{R}^{-1}(\boldsymbol{t})\boldsymbol{l}(\boldsymbol{r}, \boldsymbol{\eta})}. \tag{3.2}$$

Finally, in the absence of *a priori* orientation information from, e.g., MRI, an optimal orientation $\boldsymbol{\eta}_{opt}(\boldsymbol{r})$ must be determined. The typical approach to determining $\boldsymbol{\eta}_{opt}$ is to compute the solution that maximizes output power with respect to $\boldsymbol{\eta}$ (Sekihara and Scholz, 1996). Our approach is to compute the solution that

maximizes output SNR (Sekihara et al., 2004):

$$\boldsymbol{\eta}_{opt}(\boldsymbol{r}) = \max_{\boldsymbol{\eta}} \frac{\boldsymbol{l}^T(\boldsymbol{r},\boldsymbol{\eta})\boldsymbol{R}^{-1}(\boldsymbol{t})\boldsymbol{l}(\boldsymbol{r},\boldsymbol{\eta})}{\boldsymbol{l}^T(\boldsymbol{r},\boldsymbol{\eta})\boldsymbol{R}^{-2}(\boldsymbol{t})\boldsymbol{l}(\boldsymbol{r},\boldsymbol{\eta})} \tag{3.3}$$

As shown in Sekihara et al. (2004), the solution for $\boldsymbol{\eta}_{opt}$ is $\boldsymbol{v}_3$, the eigenvector corresponding to the minimum eigenvalue of:

$$[\boldsymbol{L}^T(\boldsymbol{r})\boldsymbol{R}^{-1}(\boldsymbol{t})\boldsymbol{L}(\boldsymbol{r})]^{-1}[\boldsymbol{L}^T(\boldsymbol{r})\boldsymbol{R}^{-2}(\boldsymbol{t})\boldsymbol{l}(\boldsymbol{r})]\boldsymbol{v}_j = \gamma_j \boldsymbol{v}_j, \tag{3.4}$$

The estimated source power $\hat{P}_s(\boldsymbol{r},\boldsymbol{t})$ can be computed from the weights $\boldsymbol{w}$ and covariance $\boldsymbol{R}(\boldsymbol{t})$:

$$\hat{P}_s(\boldsymbol{r},\boldsymbol{t}) = \langle \hat{s}(\boldsymbol{r},\boldsymbol{t})^2 \rangle = \langle [\boldsymbol{w}^T(\boldsymbol{r})\boldsymbol{b}(\boldsymbol{t})][\boldsymbol{b}^T(\boldsymbol{t})\boldsymbol{w}(\boldsymbol{r})] \rangle = \boldsymbol{w}^T(\boldsymbol{r})\boldsymbol{R}(\boldsymbol{t})\boldsymbol{w}(\boldsymbol{r}) \tag{3.5}$$

The sensor noise power $\sigma^2(\boldsymbol{t})$ may be obtained from calibration measurements of the MEG system or estimated by computing the minimum eigenvalue of $\boldsymbol{R}(\boldsymbol{t})$. Then, the power of projected sensor noise $\hat{P}_N$ may be estimated by replacing $\boldsymbol{R}(\boldsymbol{t})$ with $\sigma^2(\boldsymbol{t})\boldsymbol{I}$:

$$\hat{P}_N(\boldsymbol{r}) = \boldsymbol{w}^T(\boldsymbol{r})[\sigma^2(\boldsymbol{t})\boldsymbol{I}]\boldsymbol{w}(\boldsymbol{r}) = \sigma^2(\boldsymbol{t})\boldsymbol{w}^T(\boldsymbol{r})\boldsymbol{w}(\boldsymbol{r}) \tag{3.6}$$

Often, one is interested in the change in power from a control (i.e., baseline) time window to an active time window, i.e., a dual-condition paradigm. These windows are denoted as vectors of time samples, $\boldsymbol{t}_{con}$ and $\boldsymbol{t}_{act}$, respectively. In this case:

$$\hat{P}_{con}(\boldsymbol{r}) = \hat{P}_s(\boldsymbol{r},\boldsymbol{t}_{con}) = \boldsymbol{w}^T(\boldsymbol{r})\boldsymbol{R}_{con}\boldsymbol{w}(\boldsymbol{r}) \tag{3.7}$$

$$\hat{P}_{act}(\boldsymbol{r}) = \hat{P}_s(\boldsymbol{r},\boldsymbol{t}_{act}) = \boldsymbol{w}^T(\boldsymbol{r})\boldsymbol{R}_{act}\boldsymbol{w}(\boldsymbol{r}) \tag{3.8}$$

where $\boldsymbol{R}_{con} \equiv \boldsymbol{R}(\boldsymbol{t}_{con})$, the covariance of the control window, and $\boldsymbol{R}_{act} \equiv \boldsymbol{R}(\boldsymbol{t}_{act})$, the covariance of the active window.

In order to improve numerical stability and ensure an appropriately matched baseline period, the same orientation $\boldsymbol{\eta}_{opt}(\boldsymbol{r})$ and $\boldsymbol{w}(\boldsymbol{r})$ must be used to compute $\hat{P}_{act}(\boldsymbol{r})$ and $\hat{P}_{con}(\boldsymbol{r})$. This ensures that the magnitude of sources are comparable between the active and control periods; it also decreases the likelihood of resolving false sources. Thus, $\boldsymbol{\eta}_{opt}(\boldsymbol{r})$ and $\boldsymbol{w}(\boldsymbol{r})$ may be computed using the average covariance of the active and control periods, i.e., by substituting $\boldsymbol{R} = (\boldsymbol{R}_{act} + \boldsymbol{R}_{con})/2$. Note that $\boldsymbol{t}_{con}$ must be the same length as $\boldsymbol{t}_{act}$.

The contrast between $\hat{P}_{act}$ and $\hat{P}_{con}$ can then be expressed as a pseudo-t difference $\hat{P}_{act} - \hat{P}_{con}$ or an F-ratio $\hat{P}_{act}/\hat{P}_{con}$. If the contribution of projected sensor noise is subtracted, the ratio becomes $F = (\hat{P}_{act} - \hat{P}_N)/(\hat{P}_{con} - \hat{P}_N)$. In this paper, we will use the noise-corrected F-ratio expressed in units of decibels:

$$F_{dB} = 10 \log_{10} \frac{\hat{P}_{act} - \hat{P}_N}{\hat{P}_{con} - \hat{P}_N}. \tag{3.9}$$

Time-Frequency Extension of Conventional Beamformers

It is often desirable to compute contrasts for multiple activation windows and possibly multiple baseline windows, relative to specific experimental or cognitive events. The resulting contrasted spectrogram is a time-frequency representation of source events. In order to obtain such a representation from the conventional beamformer, one may directly compute the spectrogram of the source time series

from Equation 3.1, contrasting it with the spectrogram of the control period (Singh et al., 2002; Cheyne et al., 2003).

Another approach is to apply the weights $\boldsymbol{w}(\boldsymbol{r})$ computed above—with $\boldsymbol{R}$ generated from long time windows $\boldsymbol{t}_{act}$ and $\boldsymbol{t}_{con}$ spanning the entire duration of interest—to a new set of covariances generated from filtered and segmented data. First, the data is passed through a filter bank and partitioned into several overlapping active segments, $\boldsymbol{\tau}_{act}[n]$, and at least one control segment, $\boldsymbol{\tau}_{con}[n]$, where the subscript n refers to the index of the time window. (These windows are shorter than $\boldsymbol{t}_{act}$ and $\boldsymbol{t}_{con}$.) Then, covariances are computed for each resulting time-frequency window, yielding $\widetilde{\boldsymbol{R}}_{act}(n,f) \equiv \boldsymbol{R}(\boldsymbol{\tau}_{act}[n],f)$ and $\widetilde{\boldsymbol{R}}_{con}(n,f) \equiv \boldsymbol{R}(\boldsymbol{\tau}_{con}[n],f)$, where f corresponds to the index of the frequency band. Power maps may be computed directly by replacing $\boldsymbol{R}_{act}$ and $\boldsymbol{R}_{con}$ with $\widetilde{\boldsymbol{R}}_{act}(n,f)$ and $\widetilde{\boldsymbol{R}}_{con}(n,f)$, respectively:

$$\hat{P}_{con}(\boldsymbol{r},n,f) = \boldsymbol{w}^T(\boldsymbol{r})\widetilde{\boldsymbol{R}}_{con}(n,f)\boldsymbol{w}(\boldsymbol{r}) \tag{3.10}$$

$$\hat{P}_{act}(\boldsymbol{r},n,f) = \boldsymbol{w}^T(\boldsymbol{r})\widetilde{\boldsymbol{R}}_{act}(n,f)\boldsymbol{w}(\boldsymbol{r}) \tag{3.11}$$

$$\hat{P}_{N}(\boldsymbol{r},n,f) = \sigma^2(n,f)\boldsymbol{w}^T(\boldsymbol{r})\boldsymbol{w}(\boldsymbol{r}) \tag{3.12}$$

Finally,

$$F_{dB}(\boldsymbol{r},n,f) = 10\log_{10}\frac{\hat{P}_{act}(\boldsymbol{r},n,f) - \hat{P}_{N}(\boldsymbol{r},n,f)}{\hat{P}_{con}(\boldsymbol{r},n,f) - \hat{P}_{N}(\boldsymbol{r},n,f)}. \tag{3.13}$$

However, while spectrograms may be constructed from the conventional beamformer in this fashion, the weights are still optimized for the wide $\boldsymbol{t}_{act}$ and $\boldsymbol{t}_{con}$

windows used to compute $\boldsymbol{w}(\boldsymbol{r})$. MEG/EEG spectra follows the power law, implying that weights generated from unfiltered data are inherently biased towards low-frequency activity.

3.2.3 Frequency-Dependent Weight Computation

Therefore, in order to better resolve low-amplitude, high-frequency activity, one approach is to calculate a different set of weights for each frequency band:

$$\boldsymbol{w}(\boldsymbol{r}, f) = \frac{\boldsymbol{R}^{-1}(f)\boldsymbol{l}^T(\boldsymbol{r}, \boldsymbol{\eta})}{\boldsymbol{l}(\boldsymbol{r}, \boldsymbol{\eta})\boldsymbol{R}^{-1}(f)\boldsymbol{l}(\boldsymbol{r}, \boldsymbol{\eta})} \tag{3.14}$$

where $\boldsymbol{R}(f)$ is the covariance matrix generated from $\boldsymbol{b}(t)$ filtered for the frequency band of interest, and $\boldsymbol{\eta} = \boldsymbol{\eta}_{opt}(\boldsymbol{r}, f)$, i.e., the optimum orientation computed using $\boldsymbol{R}(f)$. The corresponding power at each voxel for each frequency band is:

$$\hat{P}_s(\boldsymbol{r}, f) = \boldsymbol{w}^T(\boldsymbol{r}, f)\boldsymbol{R}(f)\boldsymbol{w}(\boldsymbol{r}, f) \tag{3.15}$$

Again, the powers of an active window and a control window may be computed as follows:

$$\hat{P}_{con}(\boldsymbol{r}, f) = \hat{P}_s(\boldsymbol{r}, \boldsymbol{t}_{con}, f) = \boldsymbol{w}^T(\boldsymbol{r}, f)\boldsymbol{R}_{con}(f)\boldsymbol{w}(\boldsymbol{r}, f) \tag{3.16}$$

$$\hat{P}_{act}(\boldsymbol{r}, f) = \hat{P}_s(\boldsymbol{r}, \boldsymbol{t}_{act}, f) = \boldsymbol{w}^T(\boldsymbol{r}, f)\boldsymbol{R}_{act}(f)\boldsymbol{w}(\boldsymbol{r}, f) \tag{3.17}$$

The time-frequency representation may be computed either from the source time series, or, as shown here, by using $\boldsymbol{w}(\boldsymbol{r}, f)$ from Equation 3.14 and replacing $\boldsymbol{R}(f)$ from Equation 3.15 with $\widetilde{\boldsymbol{R}}_{act}(n, f)$ and $\widetilde{\boldsymbol{R}}_{con}(n, f)$:

$$\hat{P}_{con}(\boldsymbol{r}, f) = \boldsymbol{w}^T(\boldsymbol{r}, f)\widetilde{\boldsymbol{R}}_{con}(n, f)\boldsymbol{w}(\boldsymbol{r}, f) \tag{3.18}$$

$$\hat{P}_{act}(\boldsymbol{r}, n, f) = \boldsymbol{w}^T(\boldsymbol{r}, f)\widetilde{\boldsymbol{R}}_{act}(n, f)\boldsymbol{w}(\boldsymbol{r}, f) \tag{3.19}$$

$$\hat{P}_N(\boldsymbol{r}, n, f) = \sigma^2(n, f)\boldsymbol{w}^T(\boldsymbol{r}, f)\boldsymbol{w}(\boldsymbol{r}, f) \tag{3.20}$$

$$F_{dB}(\boldsymbol{r}, n, f) = 10\log_{10}\frac{\hat{P}_{act}(\boldsymbol{r}, n, f) - \hat{P}_N(\boldsymbol{r}, n, f)}{\hat{P}_{con}(\boldsymbol{r}, n, f) - \hat{P}_N(\boldsymbol{r}, n, f)}. \tag{3.21}$$

This formulation accounts for amplitude differences between different frequency bands, but its performance may be degraded in the presence of activity that is more transient. Sources that are active only briefly may not be adequately captured. Similarly, the spatial filters may not be optimized for sources that change position and orientation over time. Lastly, when analyzing long epochs, this method might be prone to sources active at different latencies interfering with each other. For example, if one source has an early response, and another nearby source becomes active later in the same frequency band, then generating weights from the covariance of the whole interval may result in degraded reconstruction and poor separation of the two sources.

3.2.4 Proposed Time-Frequency Optimized Beamforming

To overcome the above mentioned limitations, we propose that a custom set of weights $\boldsymbol{w}(\boldsymbol{r}, n, f)$ be generated from the covariances $\widetilde{\boldsymbol{R}}_{act}(n, f)$ corresponding to each time-frequency window. As in the approaches described above, the data is first passed through a filter bank and subsequently segmented into overlapping active windows, $\boldsymbol{\tau}_{act}[n]$, and control windows, $\boldsymbol{\tau}_{con}[n]$. For optimum time-frequency

resolution and beamformer performance, it is desirable to choose larger time windows for lower frequencies and narrower time windows for higher frequencies.

$$\boldsymbol{w}(\boldsymbol{r}, n, f) = \frac{\boldsymbol{R}^{-1}(n, f)\boldsymbol{l}(\boldsymbol{r})}{\boldsymbol{l}^T(\boldsymbol{r})\boldsymbol{R}^{-1}(n, f)\boldsymbol{l}(\boldsymbol{r})} \tag{3.22}$$

where $\boldsymbol{R}(n, f) = [\widetilde{\boldsymbol{R}}_{act}(n, f) + \widetilde{\boldsymbol{R}}_{con}(n, f)]/2$. Then,

$$\hat{P}_{con}(\boldsymbol{r}, n, f) = \boldsymbol{w}^T(\boldsymbol{r}, n, f)\widetilde{\boldsymbol{R}}_{con}(n, f)\boldsymbol{w}(\boldsymbol{r}, n, f) \tag{3.23}$$

$$\hat{P}_{act}(\boldsymbol{r}, n, f) = \boldsymbol{w}^T(\boldsymbol{r}, n, f)\widetilde{\boldsymbol{R}}_{act}(n, f)\boldsymbol{w}(\boldsymbol{r}, n, f) \tag{3.24}$$

$$\hat{P}_N(\boldsymbol{r}, n, f) = \sigma^2(n, f)\boldsymbol{w}^T(\boldsymbol{r}, n, f)\boldsymbol{w}(\boldsymbol{r}, n, f) \tag{3.25}$$

$$F_{dB}(\boldsymbol{r}, n, f) = 10\log_{10}\frac{\hat{P}_{act}(\boldsymbol{r}, n, f) - \hat{P}_N(\boldsymbol{r}, n, f)}{\hat{P}_{con}(\boldsymbol{r}, n, f) - \hat{P}_N(\boldsymbol{r}, n, f)}. \tag{3.26}$$

Finally, the estimated power of overlapping segments are averaged to improve numerical stability and better capture transitions in source activity. The procedure is summarized in Figure 3.1.

The computational load of the algorithm scales linearly with the number of time-frequency bins. In practice, hundreds of weight vectors must be computed to assemble a complete source spectrogram and would require dozens of CPU hours to complete. However, since the result for each time-frequency window is essentially an independent computation, the time-frequency array is well-suited for running on a parallel computing cluster. We used the shared computing cluster at the California Institute for Quantitative Biomedical Research to generate the results shown in this paper; the total running time for generating images for all

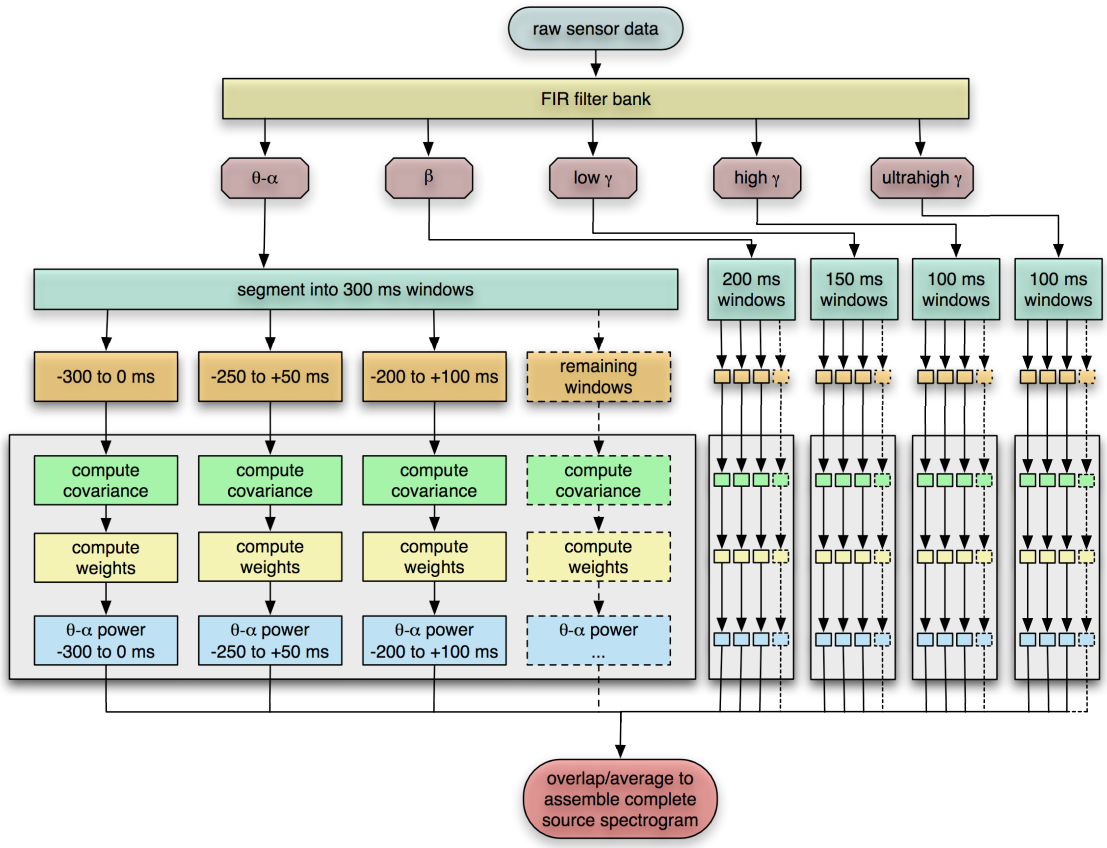

Figure 3.1 Algorithm for optimal time-frequency beamforming. Processing of the combined θ-α band is shown in detail; each of the other frequency bands has a similar workflow. Note that the algorithm is highly parallel and well-suited to run on high performance computing clusters.

time-frequency windows is less than 20 minutes when the cluster is unloaded and all windows can be processed on approximately 300 nodes simultaneously. Upon conclusion of the cluster run, the results were assembled and visualized with a development version of our NUTMEG neuromagnetic source reconstruction toolbox (Dalal et al., 2004), freely available from http://bil.ucsf.edu.

The filter bank approach provides an inherent potential advantage over FFT and wavelet-based techniques, since frequency bins can be of variable size and customized according to the experimenter's hypothesis. For example, it has been suggested that the spectral peak of high gamma activity may vary across subjects and even within an individual (Crone et al., 2001a; Edwards et al., 2005); therefore, those bands may be defined with a larger bandwidth. We chose to follow traditional MEG/EEG power band definitions as best as possible for the experiments presented here: 4–12 Hz (theta-alpha), 12–30 Hz (beta), 30–55 Hz (low gamma), and 65–90 Hz (high gamma). Additionally, we defined ultrahigh frequency bands at 90–115 Hz, 125–150 Hz, 150–175 Hz, and 185–300 Hz. The power line frequency (60 Hz) and harmonics (120 Hz and 180 Hz) were avoided to reduce noise.

3.2.5 Across-Subjects Statistics

The significance of activations across subjects was tested with statistical non-parametric mapping (SnPM) (http://www.sph.umich.edu/ni-stat/SnPM/). SnPM does not depend on a normal distribution of power change values across

subjects and allows correction for familywise error of testing at multiple voxels and time-frequency points. The detailed rationale and procedures of SnPM statistics of beamformer images are described elsewhere (Singh et al., 2003). In short, time-frequency beamformer images for each subject were first spatially normalized to the MNI template brain using SPM (http://www.fil.ion.ucl.ac.uk/spm). The three-dimensional average and variance maps across subjects were calculated at each time-frequency point, and the variance maps were smoothed with a 20×20×20 mm Gaussian kernel in order to account for the spatial frequency noise inherent to beamformer images. From this, a pseudo-t statistic was obtained at each voxel, time window, and frequency band. In addition, a distribution of pseudo-t statistics was also calculated from 2^N permutations of the original N datasets (subjects). Each permutation consisted of two steps: 1) inverting the polarity of the power change values for some subjects (with 2^N possible combinations of negations), and 2) finding the current maximum pseudo-t value among all voxels and time windows for each frequency band. Instead of estimating the significance of each non-permuted pseudo-t value from an assumed normal distribution, it is then calculated from the position within the distribution of these maximum permuted pseudo-t values. The comparison against maximum values effectively corrects for the familywise error of testing multiple voxels and time windows.

3.2.6 Numerical Experiments

Data Generation

Numerical experiments were conducted to evaluate the proposed method and compare it with existing methods. The sensor configuration of the 275-channel CTF Omega 2000 biomagnetic measurement system (VSM MedTech, Coquitlam, BC, Canada) was used. Data were simulated and processed using a development version of NUTMEG (Dalal et al., 2004).

Fifty trials of simulated data were generated, spanning -750 ms to 1000 ms per trial, sampled at 1200 Hz. Two 77 Hz sine wave sources were synthesized and placed at $(10, 50, 60)$ mm and $(15, 60, 75)$ mm[1]; the phases of each source were assigned randomly and varied between each other and each trial. The sine waves were windowed such that they represented ERS activity and were not simultaneously active; one source was active from 50 ms to 300 ms, while the other was active from 350 ms to 550 ms. A third 19 Hz source was placed at $(25, 30, 100)$ mm, active from -750 ms to 50 ms and from 600 ms to 1000 ms to simulate ERD activity.

A sensor lead field was calculated with 5 mm grid spacing using a single-layer multiple sphere volume conductor as the forward model (Huang et al., 1999) and the Omega 2000's sensor geometry with respect to a real subject's headshape.

[1]The numerical experiments used a coordinate system based on a real subject's head geometry, described as follows: The midpoint between the left and right preauricular points was defined as the coordinate origin. The x-axis was directed from the origin through the nasion, while the y-axis was directed through the left preauricular point and rotated slightly to maintain orthogonality with the x-axis. The z-axis is directed upward perpendicularly from the xy-plane towards the vertex.

Spontaneous MEG recordings from a human subject ("brain noise") were added to the generated data such that the signal-to-noise (SNR) was equal to 1. The SNR was defined as the ratio of the Frobenius norm of the simulated data matrix to that of the brain noise matrix.

Data Processing

Covariances for use with the beamformers were generated by creating a lattice of time-frequency windows. The original data were first passed through a bank of 200th-order finite impulse response (FIR) bandpass filters and subsequently split into several overlapping temporal windows with a step size of 25 ms for all bands. In our filter design, we chose to follow traditional MEG/EEG power band definitions as best as possible. Theta-alpha band was defined as 4–12 Hz with 300 ms windows, beta band 12–30 Hz with 200 ms windows, low gamma 30–55 Hz with 150 ms windows. Additionally, five high gamma bands were defined, avoiding the 60 Hz power line frequency and its harmonics: 65–90 Hz, 90–115 Hz, 125–150 Hz, 150–175 Hz, 185–300 Hz, all with 100 ms windows. Finally, covariances were generated for this matrix of time-frequency windows and averaged over trials. Spatial filter weights were computed for each time-frequency window, and an $F_{dB}(\boldsymbol{r}, n, f)$ space-time-frequency power map was assembled as described earlier.

For comparison, the data was processed in three additional ways. In the first way, which we will term the "broadband" approach, the simulated data were pro-

cessed with a conventional minimum variance beamformer; i.e., a single weight was computed from unfiltered data using one large active window and a corresponding large control window (Equation 3.2). In this case, 0 ms to 500 ms was chosen as the active window, and -600 ms to -100 ms was chosen as the control window. This weight was then applied to the covariances for each time-frequency window to calculate estimated power and contrasted with the estimated power of the control period to generate the final space-time-frequency representation.

The second way was a frequency-dependent beamformer approach (Equation 3.14). The original simulated data was passed through the same filter bank as with our proposed method. However, instead of segmenting into several time windows, the single large active window with a corresponding control window was chosen as for the broadband approach. Thus, weights were computed for filtered data corresponding to each frequency band. Again, 0 ms to 500 ms was chosen as the active window, with -600 ms to -100 ms as the control window. Weights, powers, and the final power map were generated as with the other two techniques.

Finally, the data was analyzed with sLORETA (Pascual-Marqui, 2002) as a representative of minimum norm source reconstruction techniques. As sLORETA is a nonadaptive spatial filter dependent only on sensor configuration, the same set of weights was applied to the covariances for each time-frequency window. The estimated power and contrast with a control period was performed as described above with the beamformer techniques (Equation 3.13).

3.2.7 Finger Movement Data

Subjects

Data was collected from 12 right-handed volunteers (6 females and 6 males, mean age 29.2 years, age range 22-38 years). The participants were screened for potentially confounding health conditions and medications. The study protocol was approved by the UCSF Committee on Human Research.

Data Acquisition and Processing

Data was acquired with a 275-channel CTF Omega 2000 whole-head MEG system from VSM MedTech (Coquitlam, BC, Canada) with a 1200 Hz sampling rate. All post-processing and analysis were performed using a development version of NUTMEG (Dalal et al., 2004). A digital filter was used to highpass the data at 1 Hz. Trials containing eyeblink and movement artifacts were manually rejected.

Subjects were instructed to press the response button with their right index finger (RD2) at a self-paced interval of approximately four seconds, acquiring 100 trials. In a subsequent block, the subjects completed the same task with their left index finger (LD2) instead.

The data was processed as in the above simulation, but with 50 ms window overlap due to the length of the epochs. For the broadband and frequency-domain methods, the active window was chosen to be -250 ms to 250 ms relative to the button press, with -950 ms to -450 ms as the baseline. These windows were cho-

sen based on typical results in the literature (Pfurtscheller and Neuper, 1992; Jurkiewicz et al., 2006) and our laboratory's extensive unpublished clinical data.

As with the simulations, a multiple sphere head model was calculated for each subject at 5 mm resolution based on individual head shape and relative sensor geometry. Spectral power changes were statistically tested across subjects with the SnPM method described above, with $p < 0.05$ as the threshold for significant activity.

3.2.8 Intracranial Recordings

Preoperative MEG data and corresponding intracranial electrocorticograms (ECoG) were obtained from two patients undergoing surgical treatment for intractable epilepsy. Intracranial electrodes were implanted in these patients for preresection seizure localization and functional mapping of critical language and motor areas. The study protocol, approved by the UCSF and UC Berkeley Committees on Human Research, did not interfere with the ECoG recordings made for clinical purposes and presented minimal risk to the subjects. Upon informed consent, the experiments were conducted while the patient was alert and on minimal medication. The implants consisted of an 8×8 grid of platinum-iridium electrodes (Ad-Tech Medical, Racine, WI) placed over the left frontotemporal region (Figure 3.2(a)). The electrodes had a 2.3 mm contact diameter and a center-to-center spacing of 10 mm. Electrodes with an impedance greater than 5 kΩ or exhibiting

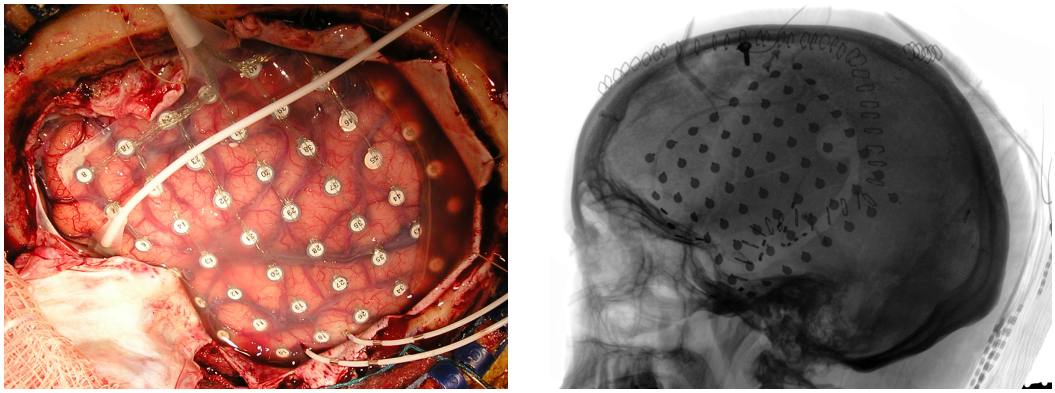

(a) (b)

Figure 3.2 (a) Example of a typical frontotemporal ECoG montage in an intractable epilepsy patient. The implant consists of an 8×8 electrode grid with 10 mm center-to-center spacing between electrodes. (b) Lateral X-ray radiograph of the same patient showing electrode locations. The surgical photograph was used to annotate the locations of visible electrodes on an MRI rendering, while the coordinates of hidden electrodes were found using X-ray backprojection to the MRI-derived brain surface (Dalal et al., 2007a).

epileptiform activity were rejected from further analyses. An electrode in the corner of the electrode grid was selected as the reference. Data was collected with an EEG amplifier (SA Instrumentation, San Diego, CA) sampling at 2003 Hz with 16-bit resolution. As with the MEG experiment, patients were asked to move their right index finger (RD2) at a self-paced interval of approximately four seconds for a total of 100 trials. Both patients had corresponding MEG recordings acquired one day prior to their grid implants. The recordings were conducted identically as with the healthy volunteers (see above).

Electrodes were localized on individual subject MRIs using visual identification of landmarks on intraoperative photographs and backprojection from postimplant

X-rays as described in Dalal et al. (2007a) (Figure 3.2). Time-frequency analyses of ECoG data were performed using the event-related spectral perturbation (ERSP) method (Makeig, 1993). Time courses for the power of single trial data were generated for each frequency band using a Gaussian filter bank and the Hilbert transform (Edwards, 2007); after averaging across trials, the power time courses were divided by the mean baseline spectrum to generate the ERSP. These results were converted to decibels and then rebinned into the same time-frequency windows used to analyze the MEG data for ease of comparison.

3.3 Results

3.3.1 Numerical Experiments

The sLORETA method produced relatively blurry results for all three simulated sources, with peaks on the periphery of the defined volume of interest in each case (see Figure 3.3). The reconstructions were not of sufficiently high fidelity to appreciably distinguish the spectrograms of the different sources. Several regularization parameters were tested with similar results.

The broadband beamformer correctly placed the peak of beta ERD at $(25, 30, 100)$ mm. (See Figure 3.3.) However, the spatiotemporal extent of both high gamma ERS sources were not as cleanly resolved. The first source was placed at $(20, 50, 60)$ mm peaking over 150–175 ms, while the second source was placed

at (20,55,70) mm, peaking over 450–475 ms. Additionally, the spatial extent of all sources was blurred.

The frequency domain beamformer found the correct location of the beta ERD, resolving a more focal peak than the broadband beamformer. (See Figure 3.3.) It also found the correct locations for both high gamma ERS sources. However, the activation was spatially blurred and attenuated for the high gamma ERS sources, especially over 300-350 ms when one source tapers off and other tapers on. Additionally, the spatiotemporal extent of all three sources was compromised. The spectrogram computed for (15,60,75) mm shows contamination from the (10,50,60) mm source and vice versa.

Finally, we applied our proposed technique to the data. (See Figure 3.3.) As expected, the beta ERD was accurately resolved. Both high gamma ERS sources were accurately localized and their temporal extents accurately captured. Virtually no contamination between the two source locations were observed on their respective spectrograms. This method provided the best reconstruction of the simulated data.

3.3.2 Finger Movement Data

The characteristic beta band power decrease in contralateral sensorimotor cortex was observed and reached statistical significance across subjects for all three beamformer variants. (See Figure 3.4 for corresponding MNI coordinates and corrected p values for right index finger movement.) However, only low-amplitude

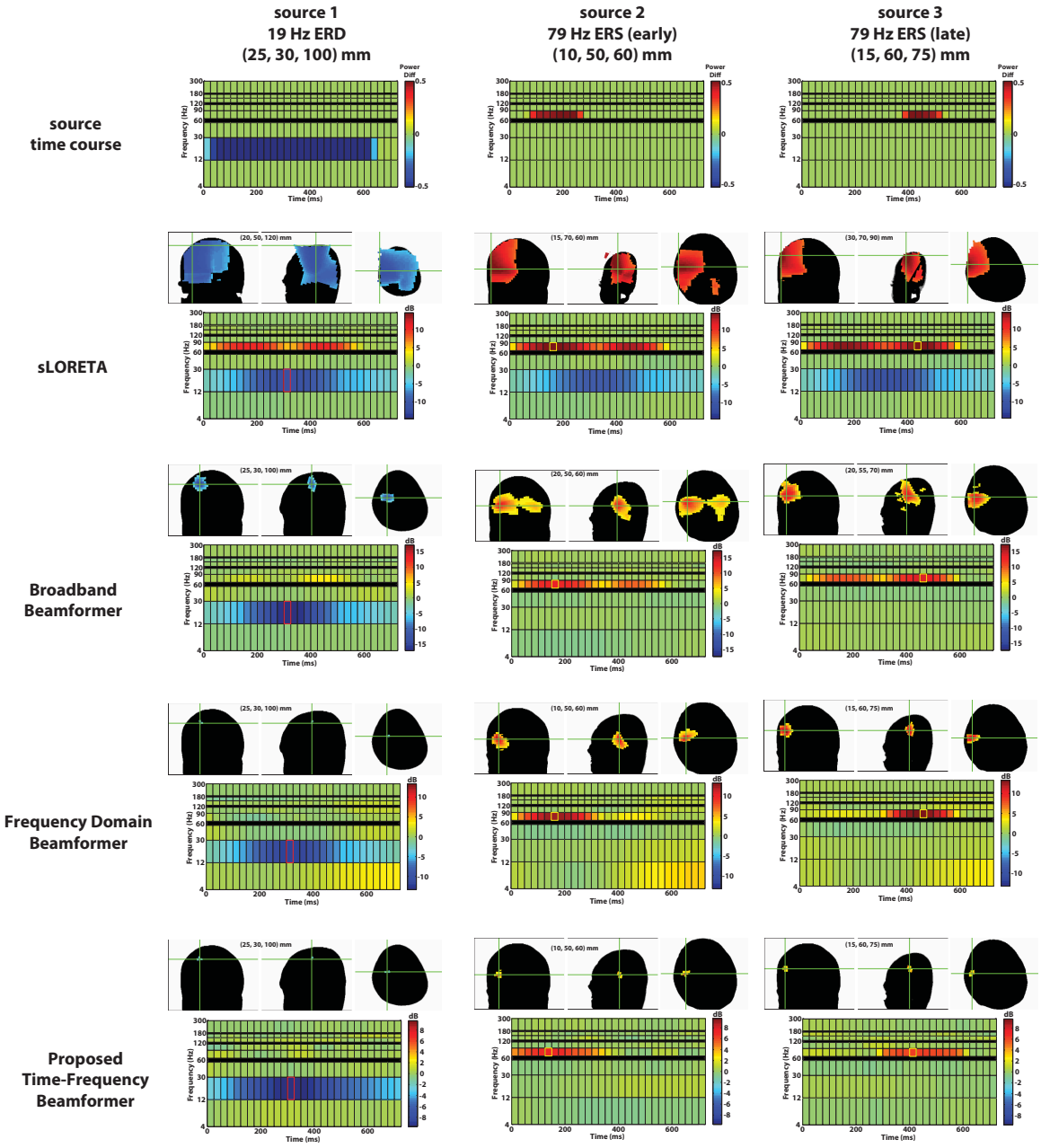

Figure 3.3 At top is the spectrogram corresponding to the three simulated sources. In the rows below are the reconstruction results using sLORETA, the broadband beamformer, the frequency domain beamformer, and the proposed time-frequency beamformer. In each of those panels, the crosshairs mark the spatiotemporal peak for the reconstructed source, with the corresponding spectrogram shown below it. The time-frequency window plotted on the MRI is highlighted on the spectrogram. The functional maps are thresholded at 50% of the maximum power (in dB) for the beamformer variants and 75% for sLORETA.

early time windows near -400 ms were significant for the broadband beamformer. In contrast, significant contralateral activation was observed over -500 ms to 250 ms with both the proposed time-frequency beamformer and the frequency-domain beamformer, although results were more spatially focal for the proposed method. Additionally, both of these methods revealed significant beta band power decreases in ipsilateral sensorimotor cortex and ipsilateral secondary somatosensory cortex approximately 0 ms to 200 ms after movement onset.

The contralateral decrease in beta power was followed by a significant contralateral beta rebound for all three methods. Again, the time-frequency beamformer performed the best, with a relatively focal activation area. The broadband beamformer revealed a peak in sensorimotor cortex, but the spatial extent of the activation extended into areas both implausibly deep as well as outside the brain. The frequency-domain beamformer placed the peak nearby, but grossly overestimated the statistically significant spatial extent, apparently due to a large baseline shift evident in voxels distant from motor cortex. The time-frequency beamformer depicts a relatively focal activation in contralateral sensorimotor cortex. (Individual results for many subjects also showed an ipsilateral beta rebound, but this did not reach statistical significance across subjects.) It also found an increase in beta power peaking at (5,-5,65) mm (MNI coordinates, $p < 0.038$, corrected), corresponding to activation of the supplementary motor area (SMA) (not shown).

Interestingly, both the frequency-domain beamformer and the time-frequency

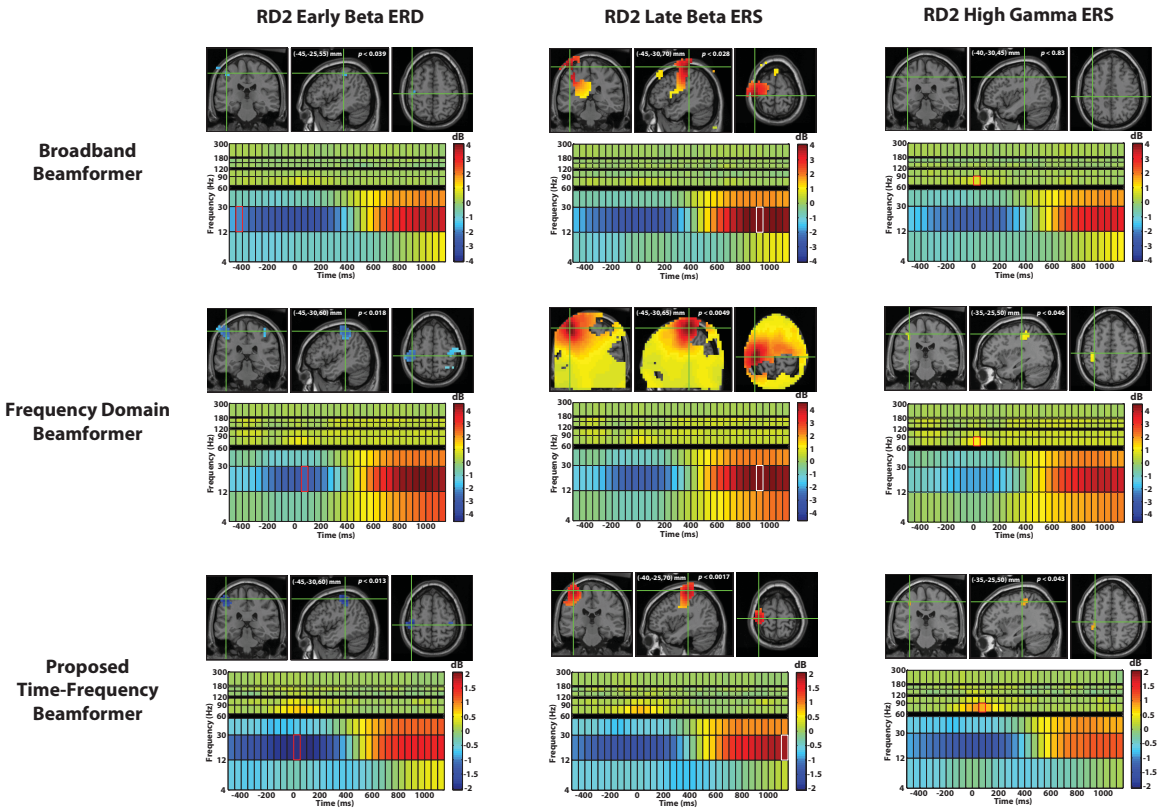

Figure 3.4 Shown above are the grand average reconstruction results for right index finger movement using the broadband beamformer, the frequency domain beamformer, and the proposed time-frequency beamformer. The functional maps are superimposed on the MNI template brain and are statistically thresholded at $p < 0.05$ (corrected). In each of the panels, the crosshairs mark the spatiotemporal peak for the reconstructed source, with the corresponding spectrogram shown below it. The functional map plotted on the MRI corresponds to the time-frequency window highlighted on the spectrogram.

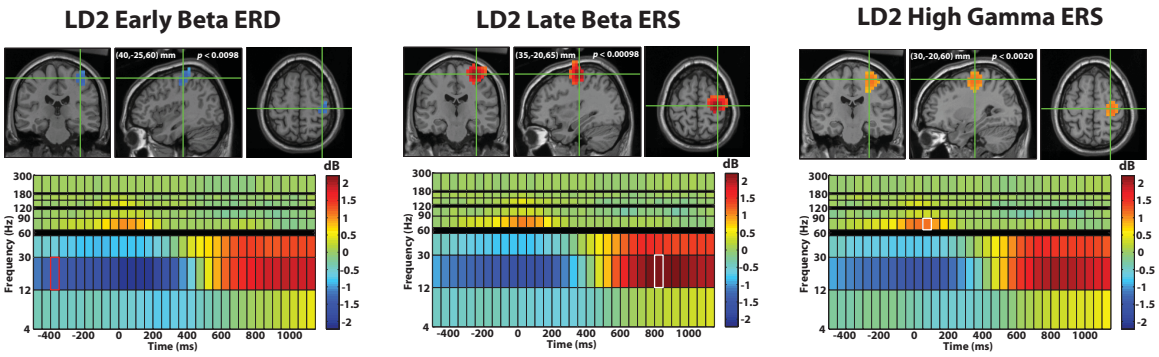

Figure 3.5 Shown above are the grand average reconstruction results for left index finger movement using the proposed time-frequency beamformer, superimposed on the MNI template brain. The functional maps are superimposed on the MNI template brain and are statistically thresholded at $p < 0.05$ (corrected). In each panel, the crosshairs mark the spatiotemporal peak for the reconstructed source, with the corresponding spectrogram shown below it. The functional map plotted on the MRI corresponds to the time-frequency window highlighted on the spectrogram.

beamformer localized a focal, statistically significant high gamma (65–90 Hz) peak in sensorimotor cortex. This activity was found to be more spatially focal and temporally bound to the movement. No significant high gamma activity was observed with the broadband beamformer.

Similarly, the proposed technique revealed similar activity for left index finger movement (Figure 3.5). The typical beta band desynchronization and late rebound as well as high gamma activity were found in right sensorimotor cortex, reaching statistical significance across subjects.

Activation of the cerebellum was also found in 9 of 12 healthy volunteers and in both of the patients. (See Figure 3.6.) While the spatiotemporal extent and particular frequency content of cerebellar activations exhibited considerable variability

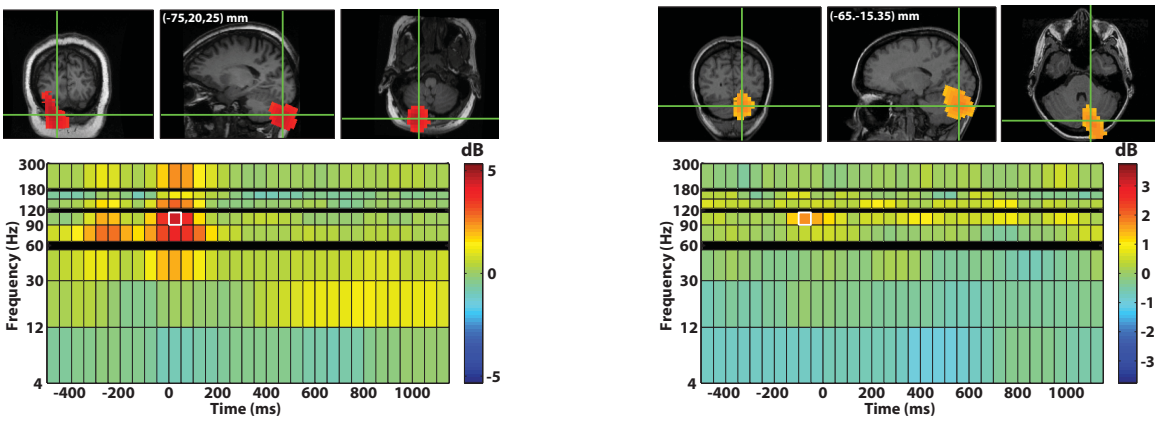

Figure 3.6 Examples of cerebellum activation for finger movement in two subjects. Above left are the results for RD2 movement in one subject. Above right are the results for LD2 movement in a different subject. Both functional maps are thresholded at 75% of the maximum power (in dB).

across subjects and did not reach statistical significance in our across-subject analyses with whole-brain multiple comparison correction, we did observe that our method found consistent high-frequency sources in the cerebellum in either the 65–90 Hz or 90–115 Hz bands. Examples of distinct cerebellar responses from two subjects are shown in Figure 3.6; see Figure 3.7 for responses from the two patients.

3.3.3 Intracranial Recordings

As shown in Figure 3.7, several locations showing ECoG activity during the right finger movement task were also found with the proposed MEG time-frequency beamformer method and exhibited fairly similar spectrogram patterns. Table 3.1 lists the coordinates of each peak in the grid coverage area for beta and high gamma activations for both patients. MEG peaks were found between 2.8 mm

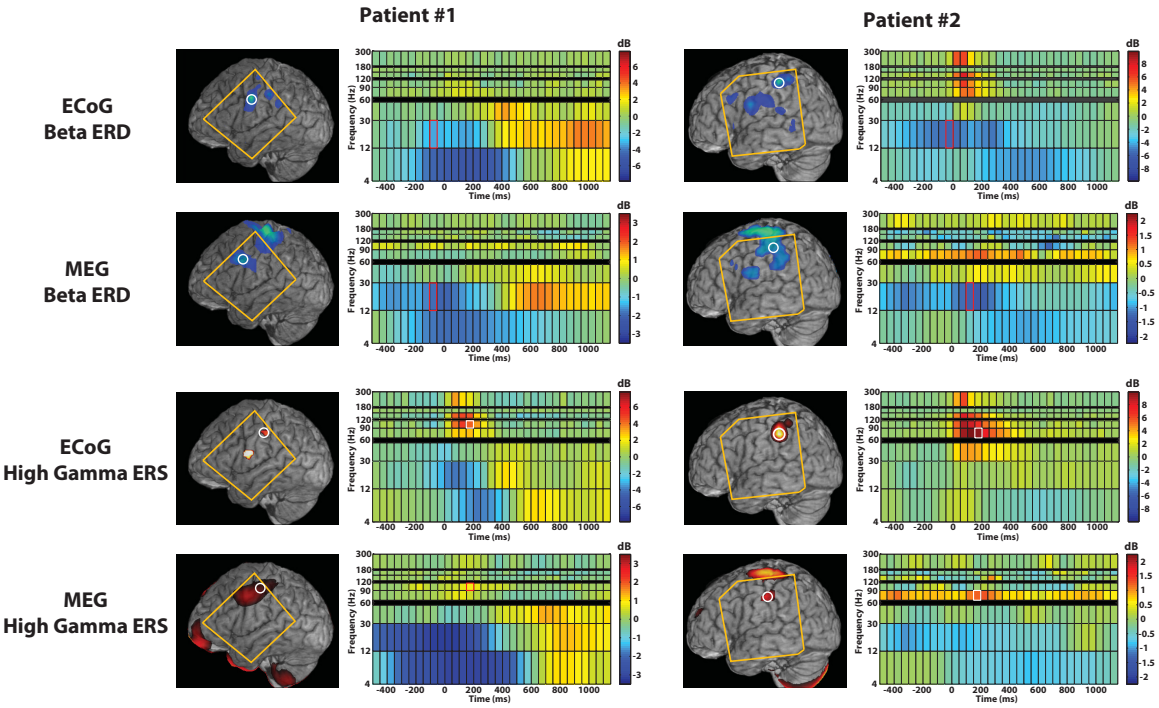

Figure 3.7 Shown above are the right finger (RD2) movement activity for two intractable epilepsy patients, using both time-frequency analyses from an 8×8 intracranial electrode grid and the corresponding results from preoperative magnetoencephalography and the proposed time-frequency beamformer. The spectrogram corresponds to the circled spatial location, while the functional maps show the spatial extent of activation for the indicated time window and frequency band. The orange outline indicates the region covered by the intracranial electrode grid. Note that MEG reveals strong primary motor cortex and cerebellum activity, but these areas were not covered with electrodes in either patient; instead, lower-amplitude secondary activations are compared between the two methods.

and 10.4 mm from eight ECoG peaks, while two adjacent electrodes showing low-amplitude beta ERD and one electrode showing high gamma ERS did not have corresponding MEG activations.

Note that the MEG reconstruction for both patients show the largest-amplitude beta desynchronization and high gamma synchronization in left primary motor cortex and the cerebellum in accordance with the across-subjects analyses above,

but these areas were not covered by the ECoG grid in either patient; therefore, the ECoG analyses show only lower-amplitude secondary areas of activation which tend to result in blurrier MEG activations. Nevertheless, the ECoG analyses supported the validity of MEG reconstructions of these secondary activations, taking into account the 1 cm spacing and cortical surface placement of the ECoG grid as well as spatiotemporal blurring inherent to the beamformer technique.

3.4 Discussion

We have shown that, with our novel time-frequency optimized beamformer techniques, MEG can resolve sources of transient power changes across multiple frequency bands, including high gamma activity. The method was validated with across-subjects statistics and intracranial recordings.

Some secondary activity revealed by the ECoG analyses was not observed with the MEG source reconstructions; these sources may have activated a small cortical region and/or were not optimally oriented for detection by MEG sensor arrays. Additionally, MEG source reconstructions for any given voxel are linear combinations of activity from multiple nearby sources due to spatiotemporal blur and may explain minor spectrogram differences as compared to ECoG. The degree of spatial blur depends on various factors, especially SNR as well as the true spatial extent of the sources.

Patient	Band	ECoG Coords (mm)	MEG Coords (mm)	Difference (mm)
1	beta	-50.6, 3.8, 28.2	-45.8, -1.2, 25.5	7.5
1	beta	-55.2, 13.2, 9.4	-50.3, 13.8, 15.3	7.7
1	beta	-54.9, -0.7, 20.6	-50.8, -1.1, 25.4	6.3
1	beta	-57.7, -5.1, 0.0	–	–
1	beta	-57.7, 0.6, 7.7	–	–
1	high gamma	-54.9, -0.7, 20.6	-51.0, -3.1, 30.0	10.4
1	high gamma	-53.7, 20.3, 3.9	–	–
2	beta	-56.9, -24.4, 30.6	-51.3, -28.9, 36.7	9.5
2	beta	-58.3, 2.0, 14.1	-61.0, 0.3, 8.9	6.1
2	beta	-55.0, -33.7, 33.3	-51.2, -27.5, 32.0	7.4
2	high gamma	-64.4, -26.4, 23.5	-66.2, -24.5, 22.5	2.8

Table 3.1 The above table lists ECoG electrode locations with activity in the beta and high gamma bands and the nearest peaks found from the MEG time-frequency beamformer reconstruction. Note that coordinates given are in each patient's native MRI space (rather than MNI coordinates) in order to accurately characterize Euclidean distances between ECoG and MEG peaks, given in the last column.

Adaptive spatial filter weights computed in the traditional manner from unfiltered or wideband data are inherently biased towards resolving low-frequency brain activity due to the power law of typical electrophysiological data. By creating a set of weights customized for each time-frequency window, higher frequency sources may be characterized with much greater fidelity. Additionally, segmenting the data into time windows can better capture the temporal extent of oscillatory modulations as well as allow for sources to change position and orientation. This is particularly important for experiment designs with long interstimulus intervals that yield several hundred milliseconds of data per epoch.

Noise is known to significantly impact the performance of minimum-norm-based methods by increasing localization bias and decreasing spatial resolution (Greenblatt et al., 2005; Sekihara et al., 2005b), and this likely explains the presented sLORETA results; ultimately, the regularization parameters and method are critical in the presence of noise. Perhaps a similar approach to the proposed method can be taken; i.e., regularization parameters can be customized for different time-frequency segments, creating a hybrid adaptive-nonadaptive source reconstruction technique. This requires additional investigations beyond the scope of this paper.

ECoG has been shown to clearly resolve high gamma (>60 Hz) activity and suggests it is more spatiotemporally focal than lower-frequency activity (Crone et al., 1998, 2001a,b; Edwards et al., 2005; Canolty et al., 2006). Recently, high gamma ac-

tivity has been gaining attention in the MEG/EEG literature as well (Kaiser et al., 2002; Hoogenboom et al., 2006; Vidal et al., 2006; Siegel et al., 2006; Osipova et al., 2006). While increases in high gamma power may coincide with decreases in beta power in many cases, high gamma may be a better indicator of task-specific neural processing in local cortical circuits since it is found to be more focused spatially and temporally. The hand motor data we present in this paper supports this hypothesis. Additionally, many studies have recently shown that high gamma activity is positively correlated with the hemodynamic response measured by functional MRI (fMRI) (Logothetis et al., 2001; Mukamel et al., 2005; Niessing et al., 2005; Brovelli et al., 2005; Hoogenboom et al., 2006; Lachaux et al., 2007). Finally, higher frequency bands may be less likely to be temporally correlated even if they are simultaneously active, and may thereby naturally circumvent the known limitation of beamformer techniques to resolve highly temporally correlated sources (Sekihara et al., 2002a).

Other ECoG studies also show motor ERS in bands greater than 60 Hz (Ohara et al., 2000; Pfurtscheller et al., 2003) and even up to 200 Hz (Leuthardt et al., 2004; Brovelli et al., 2005; Crone et al., 2006) in the same region we observed with our MEG technique. Additionally, the postmovement beta rebound has been observed in both ECoG (Pfurtscheller et al., 1996; Sochůrková et al., 2006) and MEG (Jurkiewicz et al., 2006).

Our method suggested activations in the cerebellum for most of the healthy

subjects and both epilepsy patients, though it did not reach statistical significance across subjects, likely due to individual variability in precise location, latency, and frequency. We speculate that both the sensor configuration and existing head models are not optimized for accuracy in the cerebellar region. Currently available MEG sensor arrays may not provide adequate coverage that far down the head with normal subject positioning. Furthermore, evidence from fMRI studies (Grodd et al., 2001; Hülsmann et al., 2003; Thickbroom et al., 2003; Dhamala et al., 2003; Dimitrova et al., 2006) suggests that the anterior cerebellum may be the most active, placing the neural generators fairly distant from the sensors and significantly lowering the SNR of the signals. Additionally, the strategy employed by individual subjects in pacing their finger movements may have introduced variability in the quality and extent of activation due to the cerebellum's role in timing and rhythm (Ivry and Keele, 1989; Dhamala et al., 2003; Lotze et al., 2003). Finally, existing MEG/EEG head models focus on cerebral hemispheres and do not explicitly account for the structure of the cerebellum or its role in generating signals. As such, they may introduce large lead field inaccuracies in the region of the cerebellum, severely degrading the performance of spatial filtering techniques. Perhaps more sophisticated models based on boundary element modeling (BEM) or finite element modeling (FEM) are needed to improve fidelity in the cerebellum and other deep brain structures.

Previous MEG/EEG studies have suggested coherence between the cerebellum

and cerebral cortex in the alpha and beta bands (Gross et al., 2002; Pollok et al., 2005). However, the activations found in this study suggest that the cerebellum may exhibit oscillatory activity at much higher frequencies that are not necessarily coherent with other locations, in accordance with speculation by Niedermeyer (2004) and the classic experiments of Adrian (1935), Dow (1938), Ten Cate and Wiggers (1942), and Pellet (1967). The use of space-time-frequency methods for analyzing MEG/EEG data may finally allow the cerebellum's electrical activity to be independently studied noninvasively.

In addition to the hand motor data presented in this paper, other MEG studies by our group show that our method can reveal more complex cognitive processes related to learning, decision-making, and memory (Dalal et al., 2005; van Wassenhove and Nagarajan, 2006; Hinkley et al., 2006; Guggisberg et al., 2007; van Wassenhove and Nagarajan, 2007).

The technique we propose can be customized according to the preferences of the experimenter. For example, the frequency bands and time windows can be adjusted depending on the expected SNR and trial-to-trial variability of the experiment. Any typical filter type can be used to construct the filter banks; an experimenter may prefer to substitute filters with different properties than we have chosen or even wavelet-based filters. Finally, since the power of the active windows, control window, and noise are preserved in the final results, the contrast type may be selected by the end user. Rather than an F-ratio contrast, a t-test (difference) or

the uncontrasted power time course may be selected instead.

This type of analysis does yield a large amount of information—a time-frequency spectrogram for every spatial location implies five dimensions of output data! Therefore, we have implemented an interactive time-frequency viewer into our software package NUTMEG to help make navigation of the results more intuitive. Future directions may include developing factor analysis techniques to help mine the rich output afforded by five-dimensional space-time-frequency analyses.

Acknowledgments

Special thanks to Adrian G. Guggisberg for the development of statistical methods used in this chapter, Erik Edwards for providing ECoG time-frequency analyses, Kensuke Sekihara for extensive discussions on beamformers, and Anne M. Findlay for assistance with MEG acquisition and analysis. Additional thanks to Ryan T. Canolty, Heidi E. Kirsch, and Nicholas M. Barbaro for various aspects of ECoG data acquisition and analysis. Credit is also due to Johanna M. Zumer, Susanne M. Honma, Virginie van Wassenhove, Leighton B. Hinkley, John F. Houde, Julia P. Owen, Maryam Soltani, and Mary M. Mantle for invaluable assistance and feedback, as well as Jeff Block and Jason Crane for critical advice on the use of parallel computing resources.

Chapter 4

Localization of Neurosurgically Implanted Electrodes via Photograph-MRI-Radiograph Coregistration

Abstract

Intracranial electroencephalography (iEEG) is clinically indicated for medically refractory epilepsy and is a promising approach for developing neural prosthetics. These patient populations also provide valuable data for cognitive neuroscience research. Accurate localization of iEEG electrodes is essential for evaluating specific

brain regions underlying the electrodes that indicate normal or pathological activity, as well as for relating research findings to neuroimaging and lesion studies. However, electrodes are frequently tucked underneath the edge of a craniotomy, inserted via a burr hole, or placed deep within the brain, where their locations cannot be verified visually or with neuronavigational systems.

We present a novel method for localizing iEEG electrodes. This procedure is an improvement over existing techniques yet makes use of routinely acquired surgical photographs, X-ray radiographs, and magnetic resonance imaging (MRI) scans. The end result is a set of electrode positions on the patient's rendered MRI yielding locations relative to sulcal and gyral landmarks on individual anatomy, as well as MNI coordinates. We demonstrate the superiority and accuracy of the proposed localization procedure in two intractable epilepsy patients implanted with electrode grids and strips.

4.1 Introduction

Intracranial electroencephalography (iEEG) is indicated in potential neurosurgical patients when noninvasive diagnostic techniques prove inconclusive (Bancaud et al., 1965). Most of these patients have medically intractable epilepsy, requiring long-term invasive monitoring to localize seizure foci as well as to prevent resection of critical brain areas that would result in cognitive deficits or paraly-

sis (Wyler et al., 1988; Lesser et al., 1991). These recordings also provide rare but highly valuable data to test basic hypotheses in neurophysiology and cognitive neuroscience. Furthermore, iEEG is a promising avenue for the development of neural prostheses designed to aid patients with brain or spinal cord damage resulting from trauma, stroke, or neurodegenerative diseases (Leuthardt et al., 2006; Santhanam et al., 2006; Hochberg et al., 2006).

Accurate localization of iEEG electrodes is critical for planning resective surgery as well as for relating iEEG findings to the larger neuroimaging literature. Direct visual observation of electrode positions, perhaps supplemented by neuronavigational systems (Barnett et al., 1993) or recorded with digital photography (Wellmer et al., 2002), provides the most reliable information. However, many electrodes are tucked underneath the edge of a craniotomy or guided into locations deep within the brain, and so their final locations relative to brain anatomy are not precisely known since they cannot be visually verified. In some procedures, electrodes may be inserted into the subdural space via a small burr hole.

Postimplant radiographs (X-rays) are routinely ordered at most epilepsy centers, and while they are high-resolution, they are nevertheless flat 2D projections that give little indication of underlying brain anatomy. They are typically used to visualize the approximate extent and curvature of the implanted electrode arrays. Simple measurements can be performed to estimate rough electrode positioning on anatomy (Fox et al., 1985; Miller et al., 2007). However, variable magnification

and distortion as well as inherent variability in anatomy and X-ray configuration between patients may reduce the accuracy of these measurements.

Many epilepsy centers obtain postimplant computed tomography (CT) scans to visualize the 3D configuration of the electrodes. However, CT has poor soft tissue contrast and brain structures are very difficult to discern, especially in the presence of severe streaking artifacts caused by the electrodes themselves. Therefore, CT scans must be coregistered to preoperative magnetic resonance imaging (MRI) scans in order to visualize electrode positions on brain anatomy (Grzeszczuk et al., 1992; Winkler et al., 2000; Nelles et al., 2004; Hunter et al., 2005). However, the resolution of CT is often poor, resulting in partial volume effects, and as we will show, the brain may shift considerably following the electrode implant, contributing to significant errors in coregistered location of electrodes. These disadvantages are compounded by the fact that CT delivers a large radiation dose, can be uncomfortable and sometimes risky for implanted epilepsy patients, and is relatively expensive.

Some groups acquire postimplant MRI scans, which can visualize brain anatomy with high fidelity. Unfortunately, many electrodes can be difficult to see on them (Bootsveld et al., 1994); from MRI scans published in the literature (Schulze-Bonhage et al., 2002; Kovalev et al., 2005; Sochůrková et al., 2006), it seems likely that electrodes on arrays with spacing tighter than 1 cm would be indistinguishable. Susceptibility artifacts from the electrode material may also distort the

images. As with CT, many epilepsy centers consider postimplant MRIs to be unjustifiably risky and expensive.

We present a procedure and algorithm for localizing electrodes implanted into the brains of neurosurgery patients and for interactively linking a 3D MRI with a 2D radiograph and surgical photographs. The method provides a more robust estimate of electrode positions than previously possible. Additionally, we use the transformation matrices to create an interactive viewer that links coordinates on the MRI, photograph, and radiograph; this both verifies goodness of fit as well as assists identification of other structural features on the radiograph by corresponding them to 3D locations on the patient's MRI.

4.2 Methods

4.2.1 Patients and Electrodes

Intractable epilepsy patients were implanted with subdural electrodes for the purpose of planning resective surgery. Electrode implants were guided strictly by clinical indications and research recordings were approved by the Committees on Human Research at the University of California, San Francisco and the University of California, Berkeley. The electrodes were 4 mm diameter platinum-iridium disks with a 2.3 mm contact width, embedded within a Silastic sheet (Ad-Tech Medical, Racine, WI, USA). The center-to-center spacing between electrodes was

10 mm. Grid electrodes consisted of 64 electrodes arranged in an 8×8 square and placed on the surface of left frontotemporal cortex in all patients. Electrode grids were sewn to the dura to minimize movement after placement. In most patients, supplemental 4×1 or 6×1 electrode strips (10 mm spacing) were also placed on the cortical surface. In addition, most had 4×1 depth electrodes implanted (10 mm spacing) to record from the hippocampus and amygdala.

4.2.2 Medical Images

High-resolution T1-weighted MRI scans were acquired with a FSPGR sequence at a resolution of 0.43×1.5×0.43 mm on a 3 T scanner (GE, Milwaukee, WI, USA). Lateral skull film radiographs were digitized at approximately 0.15×0.15 mm. A CT scan was acquired on one patient at a resolution of 0.43×0.43×3.75 mm.

Digital photographs were taken of the craniotomy both prior to and following placement of the electrodes using a consumer-grade camera. The camera was handheld roughly 50 cm away from the exposed cortex and oriented approximately orthogonal to it.

4.2.3 MRI Processing

Skull and scalp tissue were stripped from the structural MRIs with the Brain Extraction Tool (Jenkinson et al., 2005, http://www.fmrib.ox.ac.uk/analysis/research/bet/). This segmented vol-

ume was used to determine the coordinates of points on the brain surface as well as create rendered brains with MRIcro (Rorden and Brett, 2000, http://www.sph.sc.edu/comd/rorden/mricro.html).

4.2.4 Registration of Surgery Photographs

Two photographs are typically taken during surgical implantation of the electrode array—one showing the exposed brain (*anatomical photograph*) and one showing the electrode grid on top of the brain (*grid photograph*) (Figures 4.1(a) and 4.1b). The plastic and cabling of the electrode grid partially occludes the view of the brain anatomy underneath it; therefore, it is useful to transfer the coordinates of the electrodes seen in the grid photograph to the anatomical photograph. Fortunately, matching two photographs of the same scene taken with an uncalibrated camera is a 2D homography problem that is well-studied in the field of computer vision; given at least four matched point pairs called *control points*, a *projective transform* may be computed to map any given point from one photograph to the other (Abdel-Azziz and Karara, 1971; Hartley and Zisserman, 2004). In this case at hand, several control points can easily be chosen on the two photographs, including prominent features of blood vessels, distinct corners of the craniotomy, fixed sutures, and other stationary surgical hardware.

Given N pairs of control points with coordinates $\boldsymbol{a}_i \equiv (x_i, y_i)$ from the first photograph and $\boldsymbol{b}_i \equiv (u_i, v_i)$ from the second photograph, the projective transform

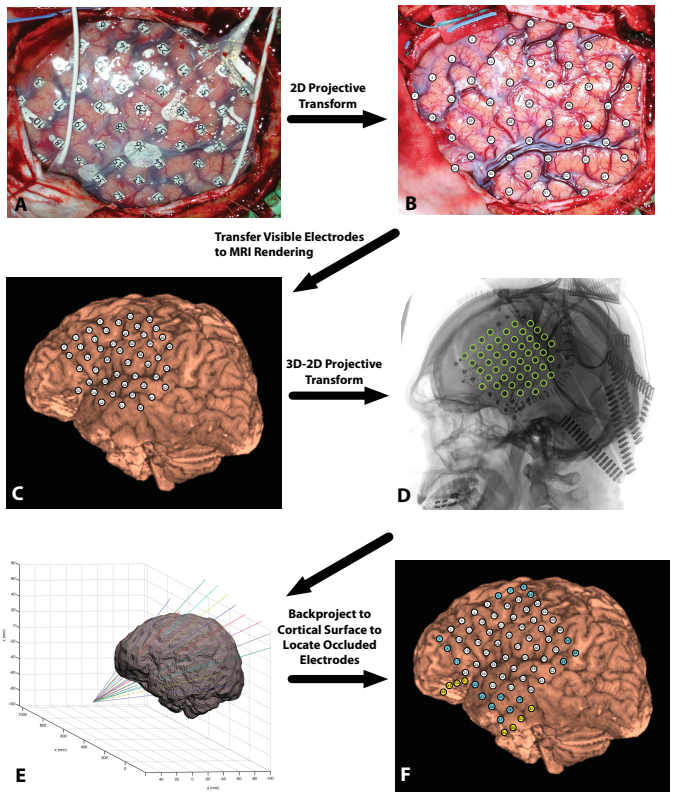

Figure 4.1 Complete procedure for registration of electrodes from photographs, MRI, and X-ray. (a) Photograph showing position of grid implant. Cables entering the bottom left and bottom right corners of the craniotomy connect to electrode strips. (b) Photograph taken immediately before grid placement clearly showing anatomical features. A projective transform with the photograph in (a) is computed with several manually selected point correspondences, such as blood vessel features, craniotomy edges, and stationary surgical hardware. The transform were then applied to electrode positions from (a) and superimposed. (c) MRI-based brain rendering with electrode positions transcribed from the photographs. (d) Lateral radiograph showing electrode positions (dark dots) along with electrode cabling. The green circles outline the electrodes with 3D locations known from the previous photograph-MRI registration step; these two sets of coordinates were used as control pairs to generate the MRI-radiograph projective transform. (e) The projective transform can be used to compute the location of the X-ray source and trace the path of X-rays that generated the image for each electrode location. Surface electrodes are known to be at the intersection of these rays with the cortical surface. (f) The final rendering showing electrode positions confirmed by the photograph (in white) and those determined solely by backprojection (grid electrodes in blue, strip electrodes in yellow). Note that the strip electrodes A1-A4 and B1-B4 are difficult to see at the contrast level chosen for the shown radiograph.

may be computed as follows. First, the coordinates are normalized with transforms $\boldsymbol{T}_1$ and $\boldsymbol{T}_2$, respectively, such that the centroid for each group is (0,0) and the mean distance from the origin is $\sqrt{2}$ for each set of points. Let us define $\widetilde{\boldsymbol{a}}_i \equiv \boldsymbol{T}_1[\boldsymbol{a}_i \;\; 1]^T$ and $\widetilde{\boldsymbol{b}}_i \equiv \boldsymbol{T}_2[\boldsymbol{b}_i \;\; 1]^T$, with $\widetilde{\boldsymbol{a}}_i = (\widetilde{x}_i, \widetilde{y}_i, 1)$ and $\widetilde{\boldsymbol{b}}_i = (\widetilde{u}_i, \widetilde{v}_i, 1)$. The coordinate vectors are augmented with unity as a scaling factor, which will become important later.

Then, the discrete linear transformation (DLT) algorithm can be used to determine the 3×3 projective transform $\widetilde{\boldsymbol{P}}$ that best maps $\widetilde{\boldsymbol{a}}$ to $\widetilde{\boldsymbol{b}}$ (Abdel-Azziz and Karara, 1971; Hartley and Zisserman, 2004):

$$\widetilde{\boldsymbol{P}} = \begin{bmatrix} p_{11} & p_{12} & p_{13} \\ p_{21} & p_{22} & p_{23} \\ p_{31} & p_{32} & 1 \end{bmatrix} \tag{4.1}$$

where the entries in $\widetilde{\boldsymbol{P}}$ can be determined by solving the following $2N \times 8$ system:

$$\begin{bmatrix} \widetilde{x}_1 & \widetilde{y}_1 & 1 & 0 & 0 & 0 & -\widetilde{u}_1\widetilde{x}_1 & -\widetilde{u}_1\widetilde{y}_1 \\ 0 & 0 & 0 & \widetilde{x}_1 & \widetilde{y}_1 & 1 & -\widetilde{v}_1\widetilde{x}_1 & -\widetilde{v}_1\widetilde{y}_1 \\ \vdots & \vdots & \vdots & \vdots & \vdots & \vdots & \vdots & \vdots \\ \widetilde{x}_N & \widetilde{y}_N & 1 & 0 & 0 & 0 & -\widetilde{u}_N\widetilde{x}_N & -\widetilde{u}_N\widetilde{y}_N \\ 0 & 0 & 0 & \widetilde{x}_N & \widetilde{y}_N & 1 & -\widetilde{v}_N\widetilde{x}_N & -\widetilde{v}_N\widetilde{y}_N \end{bmatrix} \begin{bmatrix} p_{11} \\ p_{12} \\ p_{13} \\ p_{21} \\ p_{22} \\ p_{23} \\ p_{31} \\ p_{32} \end{bmatrix} = \begin{bmatrix} \widetilde{u}_1 \\ \widetilde{v}_1 \\ \widetilde{u}_2 \\ \widetilde{v}_2 \\ \vdots \\ \widetilde{u}_N \\ \widetilde{v}_N \end{bmatrix} \tag{4.2}$$

When $N > 4$, the system is overdetermined, but may be solved in a least

squares sense using singular value decomposition. Then, in order to apply the transform to the original coordinate spaces, the normalization transforms must be applied to $\widetilde{\boldsymbol{P}}$:

$$\boldsymbol{P} \equiv \boldsymbol{T}_2^{-1} \widetilde{\boldsymbol{P}} \boldsymbol{T}_1 \tag{4.3}$$

Finally, $\boldsymbol{P}$ may be applied to any point $\boldsymbol{m} \equiv (m_x, m_y)$ from the first image to estimate the corresponding point $\hat{\boldsymbol{n}} \equiv (\hat{n}_u, \hat{n}_v)$ on the second image:

$$\begin{bmatrix} k\hat{n}_u \\ k\hat{n}_v \\ k \end{bmatrix} = \boldsymbol{P} \begin{bmatrix} m_x \\ m_y \\ 1 \end{bmatrix} \tag{4.4}$$

Note that after applying the transform to (m_x, m_y), the first two elements of the output vector must be divided by the third, k, to yield $(\hat{n}_u, \hat{n}_v)$. This effectively removes any perspective distortion; in fact, if $\boldsymbol{P}$ defines an affine transform, then the mapping is distortionless by definition and $k = 1$.

The transform requires matching of fixed landmarks (*fiducials*) between the two photographs; in this application, features on visible portions of the brain, blood vessels, and fixed surgical hardware may be used as landmarks for control points. The computed transform can then estimate the coordinates on the anatomical photograph corresponding to any point from the grid photograph. Therefore, the transform is applied to the coordinates of all visible electrodes in the grid photograph. This method does not require that the two photographs be taken with identical parameters (e.g., the angle, distance, and zoom/focus settings need not

be the same).

4.2.5 Photograph-MRI Registration

The locations of visible electrodes from the photograph can then be manually annotated on a high-resolution MRI surface rendering of the patients brain. This yields a set of 3D coordinates of known electrode positions in MRI space (Figure 4.1c). This process may be assisted with the use of a 3D-2D projective transform (see Section 4.2.6 below), or a feature matching algorithm may help automate this step (e.g., Yuan et al., 2004).

4.2.6 MRI-Radiograph Registration

The projective transform used above to register two photographs of the same scene may be extended to a more general "camera" problem (Abdel-Azziz and Karara, 1971). A photograph is a projection of 3D "world" points onto a 2D image plane; light rays from the photographed scene converge onto a focal point behind the image plane (film or digital sensor). Note that radiography is a special case of the camera problem in which the focal point is actually the X-ray source; the X-rays then *diverge* before being absorbed by the object or the film/sensor (image plane) behind it. Fortunately, most camera geometry principles and formulae are readily generalizable to the case of radiography with the proper assignment of polarities to various parameters. Thus, in our case, the 3D world data is represented by the

MRI and the photographic projection is represented by the X-ray image. It should be noted that due to the fan beam configuration of typical clinical X-ray sources, an affine transform—which assumes parallel rays—would result in greater registration errors.

Given at least six control points matching 3D world locations to a 2D image plane, a 3×4 projective transform may be computed to map *any* 3D location to the image. (Abdel-Azziz and Karara, 1971; Hartley and Zisserman, 2004). In practice, ten or more well-distributed control points are needed to generate a reliable transform. It is difficult to find that many uniquely identifiable yet nonplanar point correspondences given a standard MRI and uncalibrated radiograph. Other approaches require calibration of the X-ray system (including precise measurement of the position and orientation of the X-ray source relative to the patient) and/or placement of additional external markers that can be observed in both sets of images (e.g., Gutiérrez et al., 2005). These methods are cumbersome to implement in clinical practice and cannot work for typical existing data.

However, electrodes are clearly visible on radiographs (Figure 4.1d) and many of their 3D positions are known from the above photograph-MRI registration. Therefore, several known 3D-2D point correspondences exist from the visible electrodes. With the addition of some potentially clear anatomical landmarks (e.g., nasion, auditory canals, teeth, and upper vertebrae), enough control points can be defined to create a viable projective transform between the MRI and the ra-

diograph. As a sanity check, the transform can confirm the location of the X-ray source, which in a typical clinical setting is 100 cm from the head. The transform can then be applied to the X-ray positions of the electrodes.

We start with N pairs of control points with coordinates $\boldsymbol{a}_i \equiv (x_i, y_i, z_i)$ from the MRI and $\boldsymbol{b}_i \equiv (u_i, v_i)$ from the radiograph. As with the 2D projective transform, the coordinates should be normalized with transforms $\boldsymbol{T}_1$ and $\boldsymbol{T}_2$, respectively, such that each set of coordinates has a centroid that falls on the origin and is distributed with a mean distance of $\sqrt{3}$ for the 3D coordinates and $\sqrt{2}$ for the 2D coordinates. Let us define $\widetilde{\boldsymbol{a}}_i \equiv \boldsymbol{T}_1[\boldsymbol{a}_i \;\; 1]^T$ and $\widetilde{\boldsymbol{b}}_i \equiv \boldsymbol{T}_2[\boldsymbol{b}_i \;\; 1]^T$, with $\widetilde{\boldsymbol{a}}_i = (\widetilde{x}_i, \widetilde{y}_i, \widetilde{z}_i)$ and $\widetilde{\boldsymbol{b}}_i = (\widetilde{u}_i, \widetilde{v}_i)$.

An expanded form of the DLT algorithm can be used to determine the 3×4 projective transform $\widetilde{\boldsymbol{P}}$ that best maps $\widetilde{\boldsymbol{a}}$ to $\widetilde{\boldsymbol{b}}$ (Abdel-Azziz and Karara, 1971; Hartley and Zisserman, 2004):

$$\widetilde{\boldsymbol{P}} \equiv \begin{bmatrix} p_{11} & p_{12} & p_{13} & p_{14} \\ p_{21} & p_{22} & p_{23} & p_{24} \\ p_{31} & p_{32} & p_{33} & 1 \end{bmatrix} \tag{4.5}$$

where the entries in $\widetilde{\boldsymbol{P}}$ can be determined by solving the following $2N \times 11$ system:

$$\begin{bmatrix} \widetilde{x}_1 & \widetilde{y}_1 & \widetilde{z}_1 & 1 & 0 & 0 & 0 & 0 & -\widetilde{u}_1\widetilde{x}_1 & -\widetilde{u}_1\widetilde{y}_1 & -\widetilde{u}_1\widetilde{z}_1 \\ 0 & 0 & 0 & 0 & \widetilde{x}_1 & \widetilde{y}_1 & \widetilde{z}_1 & 1 & -\widetilde{v}_1\widetilde{x}_1 & -\widetilde{v}_1\widetilde{y}_1 & -\widetilde{v}_1\widetilde{z}_1 \\ \vdots & \vdots & \vdots & \vdots & \vdots & \vdots & \vdots & \vdots & \vdots & \vdots & \vdots \\ \widetilde{x}_N & \widetilde{y}_N & \widetilde{z}_N & 1 & 0 & 0 & 0 & 0 & -\widetilde{u}_N\widetilde{x}_N & -\widetilde{u}_N\widetilde{y}_N & -\widetilde{v}_N\widetilde{z}_N \\ 0 & 0 & 0 & 0 & \widetilde{x}_N & \widetilde{y}_N & \widetilde{z}_N & 1 & -\widetilde{v}_N\widetilde{x}_N & -\widetilde{v}_N\widetilde{y}_N & -\widetilde{v}_N\widetilde{z}_N \end{bmatrix} \begin{bmatrix} p_{11} \\ p_{12} \\ p_{13} \\ p_{14} \\ p_{21} \\ p_{22} \\ p_{23} \\ p_{24} \\ p_{31} \\ p_{32} \\ p_{32} \\ p_{33} \end{bmatrix} = \begin{bmatrix} \widetilde{u}_1 \\ \widetilde{v}_1 \\ \widetilde{u}_2 \\ \widetilde{v}_2 \\ \vdots \\ \widetilde{u}_N \\ \widetilde{v}_N \end{bmatrix} \tag{4.6}$$

Again, in practice the system will be overdetermined (given $N > 6$), so singular value decomposition can be used to find the least squares solution. Next, $\widetilde{\boldsymbol{P}}$ is denormalized so that it may be applied to the original coordinate spaces:

$$\boldsymbol{P} \equiv \boldsymbol{T}_2^{-1}\widetilde{\boldsymbol{P}}\boldsymbol{T}_1 \tag{4.7}$$

Finally, $\boldsymbol{P}$ may be applied to any MRI point $\boldsymbol{m} \equiv (m_x, m_y, m_z)$ to estimate the

corresponding point on the radiograph $\hat{\boldsymbol{r}} \equiv (\hat{r}_u, \hat{r}_v)$:

$$\begin{bmatrix} k\hat{r}_u \\ k\hat{r}_v \\ k \end{bmatrix} = \boldsymbol{P} \begin{bmatrix} m_x \\ m_y \\ m_z \\ 1 \end{bmatrix} \tag{4.8}$$

As with the 2D-2D case, the first two elements of the output vector must be divided by the third, k, to to remove projective distortion and obtain $(\hat{r}_u, \hat{r}_v)$.

An interesting property of the projective transform $\boldsymbol{P}$ is that the position of the focal point $\boldsymbol{f}$ (i.e., the X-ray source) may be directly calculated from it. Let us define:

$$\boldsymbol{M} \equiv \begin{bmatrix} p_{11} & p_{12} & p_{13} \\ p_{21} & p_{22} & p_{23} \\ p_{31} & p_{32} & p_{33} \end{bmatrix} \tag{4.9}$$

and

$$\boldsymbol{p}_4 \equiv [p_{14} \;\; p_{24} \;\; p_{34}]^T \tag{4.10}$$

such that $\boldsymbol{P} = [\boldsymbol{M} \;\; \boldsymbol{p}_4]$. Then, the focal point is known to be

$$\boldsymbol{f} = -\boldsymbol{M}^{-1}\boldsymbol{p}_4 \tag{4.11}$$

Indeed, if $\boldsymbol{M}$ is singular, $||\boldsymbol{f}|| = \infty$ and therefore $\boldsymbol{P}$ would define an affine transform, which assumes parallel rays with no convergence (i.e., an infinite focal length).

In practice, the DLT method for 3D-2D registration is somewhat sensitive to noise and inaccuracy in the given control points, and the computed X-ray source location is subject to some uncertainty along the axis perpendicular to the X-ray image plane. However, with only knowledge of the distance and approximate direction of the X-ray source, Levenberg-Marquardt optimization (Levenberg, 1944; Marquardt, 1963) may be used to adjust the displacement parameters in the normalization transform $\boldsymbol{T}_1$ to ensure a reasonable estimate of $\boldsymbol{f}$ and, by extension, $\boldsymbol{P}$.

Applying the projective transform $\boldsymbol{P}$ maps every 3D MRI point to a 2D radiograph point. We are interested in mapping the radiograph points to the MRI as well, but since $\boldsymbol{P}$ is a 3×4 matrix, $\boldsymbol{P}^{-1}$ is not defined. However, a form of the inverse projective transform does exist! Intuitively, all points on a line passing through the focal point $\boldsymbol{f}$ must map to a single point on the radiograph. Therefore, applying the inverse projective transform to a point on the radiograph should backproject to a *line* in MRI space. For a non-affine projective transform, the line equation is known to be (Hartley and Zisserman, 2004):

$$\boldsymbol{l}(\boldsymbol{r},\mu) = \boldsymbol{M}^{-1}\left(\mu\begin{bmatrix}\boldsymbol{r}^T\\ \\ 1\end{bmatrix} - \boldsymbol{p}_4\right) \tag{4.12}$$

where $\boldsymbol{r} \equiv (r_u, r_v)$ is the radiograph coordinate to be backprojected, and μ is a parameter that determines position along the backprojected line.

If the electrodes are known to be on the brain surface, then their coordinates

are easily found by backprojecting each electrode's X-ray location and finding the intersection with the set of MRI points comprising the brain outline. It should be noted that large backprojection errors may arise in areas where the brain curves sharply away from the X-ray image plane. For example, when backprojecting to the bottom of the temporal lobe from a lateral radiograph, small errors along the superior-inferior axis of the brain may result in large displacement along the left-right axis. In this case, known electrode spacing can be used to constrain the solution.

The solution for localizing depth electrodes is more involved. If multiple X-ray views are available, projective transforms can be computed for each of them; a depth electrode can then be localized by computing the intersection of its backprojections from each X-ray view. Alternatively, if only one X-ray view is available, the position of electrodes along the backprojected lines may be estimated from knowledge of the approximate depth of the shallowest electrode on a given probe, using known spacing to determine the position of remaining electrodes.

4.2.7 Transformation to Canonical Coordinate System

Given a set of electrode positions on a patient's individual 3D MRI space, it is quite straightforward to transform them to a standard coordinate system such as the Montreal Neurological Institute (MNI) template (Evans et al., 1993; Mazziotta et al., 2001). We used SPM2 (http://www.fil.ion.ac.uk/spm) to generate the non-

linear spatial transformation function using the preoperative MRI. The transform was then applied to the electrode coordinates determined from X-ray backprojection to obtain corresponding MNI coordinates. After conversion to Talairach coordinates (http://imaging.mrc-cbu.cam.ac.uk/imaging/MniTalairach), the Talairach Daemon (http://ric.uthscsa.edu/projects/talairachdaemon.html) may be used to corresponding anatomical labels from the Talairach atlas (Talairach and Tournoux, 1988). Note that since many epilepsy patients have unusual brain anatomy, it is especially important to use spatial normalization only to obtain standardized coordinates; functional activations should be rendered on an individual's MRI rather than a standard template.

4.2.8 Interactive Navigation

Another 3D-2D projective transform can be synthesized to map MRI surface points onto the anatomical photograph, using the electrode positions from Section 4.2.5 and/or distinct anatomical features as control points. We have created an interactive navigation tool that uses this MRI-photograph transform along with the the MRI-radiograph transform to allow a user to select any point on the MRI and immediately see that point's corresponding projection on the radiograph and photograph (Figure 4.2). Conversely, selecting a point on the radiograph defines a corresponding point on the photograph and a line (i.e., the X-ray path) on the MRI. Finally, if the MNI spatial normalization has been performed, corresponding MNI

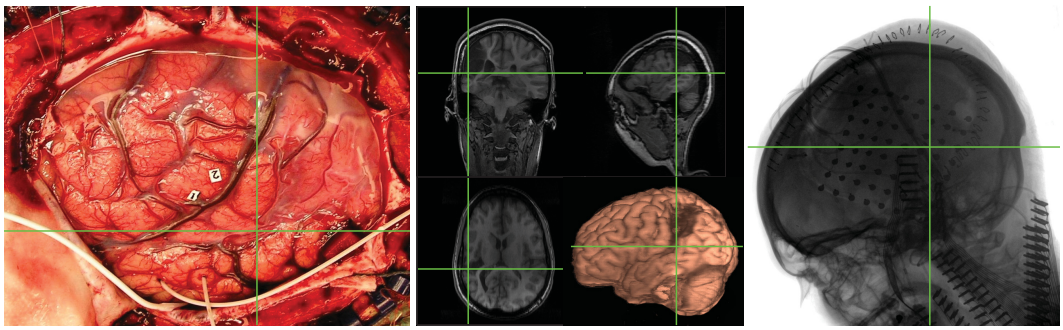

Figure 4.2 Interactive navigation is possible with the photograph, MRI, and radiograph linked via projective transforms. The crosshairs on each image indicate the same brain location, in this case, the inferior tip of a large parietal encephalomalacia.

coordinates and anatomical labels can be displayed.

4.2.9 Performance Evaluation

Accuracy of MRI-Radiograph Projective Transform

In one patient, the complete set of 47 visible electrodes along with four anatomical fiducials (superior orbital ridge, left and right auditory canals, and the vertex) were used to generate the MRI-radiograph projective transform. The backprojected coordinates were compared with the gold standard of photograph-derived coordinates.

We also tested the performance of the projective transform for locations that were not used as control points. Since it is not possible to validate the computed coordinates for electrodes that are located beyond extent of the craniotomy, another projective transform was generated using only 6 of the 47 visible elec-

trodes. The coordinates found from X-ray backprojection were compared with the photograph-derived coordinates not used to compute the transform.

CT-MRI Coregistration

Another patient had a CT scan in addition to high-resolution preoperative MRI scan to a postimplant lateral radiograph. CT-MRI coregistration was performed with SPM2 using a mutual information algorithm. The quality of coregistration was visually verified by ensuring good agreement of skull shape between the CT and MRI. Electrode coordinates were found using our proposed method and compared with the electrode positions derived from the coregistered CT scan. 3D renderings of CT electrode positions on the MRI were created with MRIcro. Figures showing coregistered CT/MRI slices were generated with OsiriX (Rosset et al., 2004, http://homepage.mac.com/rossetantoine/osirix/).

4.3 Results

4.3.1 Performance Evaluation

Electrode locations found by computing projective transforms based on all visible electrodes had a mean discrepancy of 1.55 mm (s.d. 0.53 mm, max 2.71 mm) when compared to the photograph-derived coordinates (Figure 4.3, blue points). Using only a subset of six electrodes to compute the projective transform, the out-

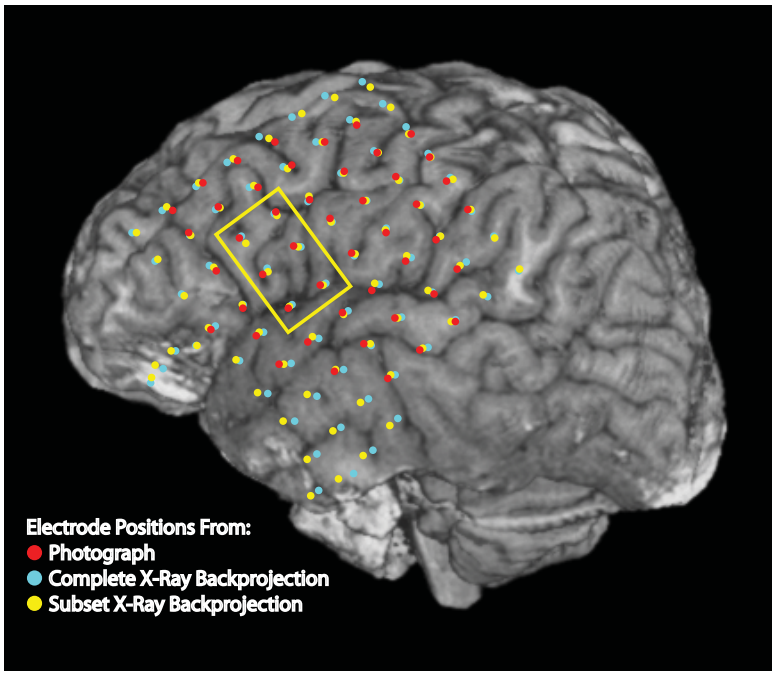

Figure 4.3 Evaluation of registration for the same patient shown in Figure 4.1. Known electrode positions from the photograph are shown as red dots, and the results from using the projective transform with all known electrode positions are depicted in blue. Since it is not possible to validate the location of hidden electrodes, a subset of six visible electrodes (boxed in yellow) were chosen to compute another projective transform. This transform was then applied to all X-ray locations, with the backprojection solution shown in yellow. The results from just these six electrodes agree closely with the known photograph-based positions as well as the results from the complete projective transform.

put electrode locations yielded only a mean discrepancy of 2.05 mm (s.d. 0.96 mm, max 4.64 mm) from the photograph-based positions (Figure 4.3, yellow points).

4.3.2 CT-MRI Coregistration

As shown in Figure 4.5, coregistration of the postimplant CT with the preimplant MRI does not yield a satisfactory solution. Even though the skull and intact right hemisphere were well-registered, several surface electrodes coregistered to

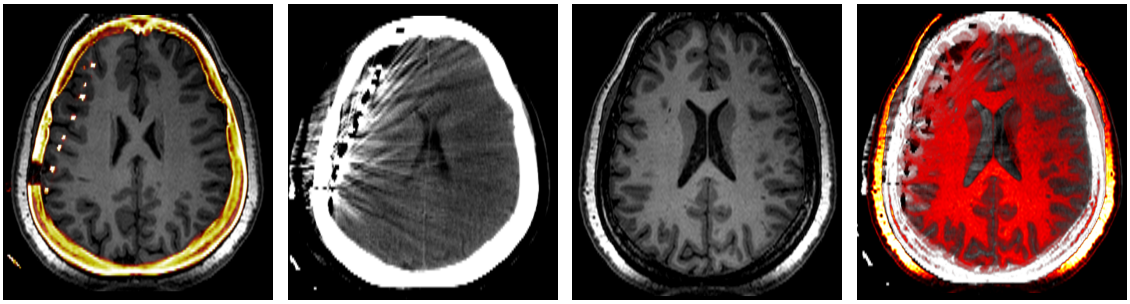

(a) (b) (c) (d)

Figure 4.4 Coregistration of postimplant CT (in color) with preoperative MRI (grayscale) in one patient. (a) Even though registration of the skull, scalp, and right hemisphere are good, many surface electrodes on the coregistered CT land more than 10 mm deep on the MRI. (b) Another slice of the CT scan adjusted for contrast to visualize the ventricles. (c) The corresponding MRI slice. (d) The MR (color) slice overlaid on the CT (grayscale). Note the clear midline shift, indicating significant brain deformation.

locations more than 1 cm deep into brain tissue on the MRI (Figure 4.4(a)). Another CT-MRI overlay (Figure 4.4(d)) shows that the midline of the brain shifted considerably. These displacements are likely due to the craniotomy, associated swelling, and the thickness of the cables and electrodes themselves.

Therefore, it was necessary to project electrode locations from the CT to the brain surface. Figure 4.5 compares the results of this procedure to electrode locations from the surgical photograph. The discrepancy of CT-based electrode positions with the photograph-based positions averaged 7.48 mm (s.d. 2.51 mm), with a maximum error of 14.5 mm. Upon removal of the grid implant, the surgeon (NMB) confirmed that the grid had not shifted appreciably. Additionally, iEEG recordings from this patient showed patterns consistent with the photograph-

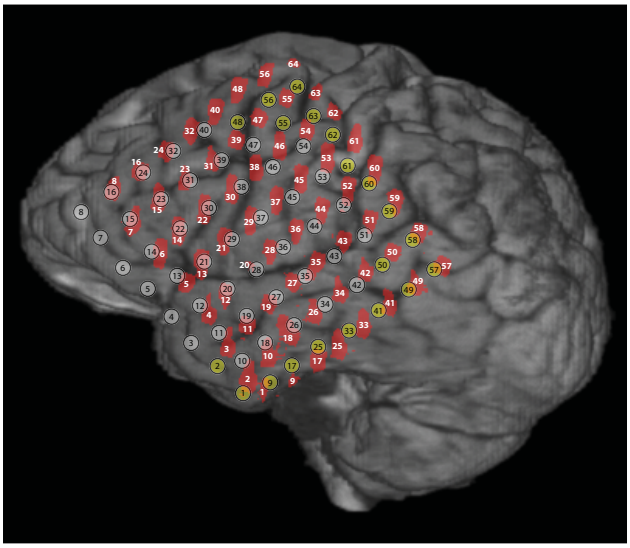

(a)

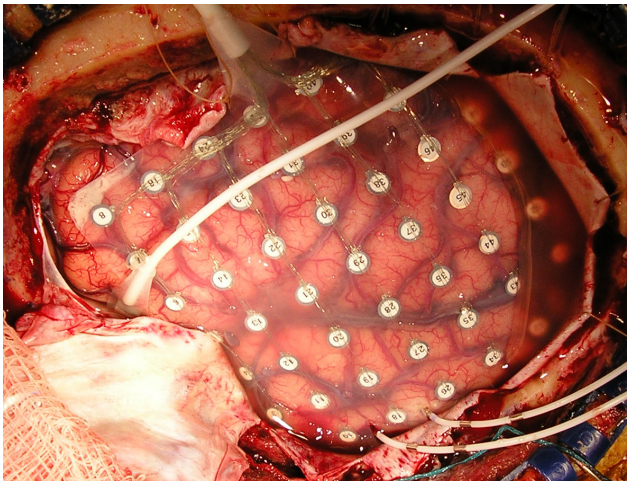

(b)

Figure 4.5 (a) Comparison of electrode registration with the proposed technique and from CT-MRI coregistration. The red splotches are the CT-derived positions; their shape is determined from intensity-based segmentation of the CT. The translucent white disks indicate positions known from the surgical photographs, while the yellow disks indicate positions backprojected from the X-ray. The CT-derived positions are considerably displaced posteriorly relative to the photograph-verified positions. (b) Surgical photograph for this patient.

based electrode locations, such as phase reversals across the Sylvian fissure as well as auditory and motor responses in expected areas (Canolty et al., 2006; Dalal et al., 2007b).

4.4 Discussion

We have demonstrated that our procedure outputs an accurate localization of electrode positions and does not require additional imaging procedures that add risk, radiation exposure, and expense to standard practice. Our technique makes use of digital photographs and high-resolution MRIs that have only recently been incorporated into the standard of care for epilepsy surgery patients. Precise knowledge of the X-ray configuration, placement of additional fiducial markers on the patient, and special calibration are not required. Most importantly, as the input images required are already collected by most neurosurgery centers, the technique can be quickly implemented and introduced to clinical use as well as applied to archived images from past patients for research use.

We have also shown that a popular technique for electrode localization, coregistration of postimplant CT scans with preoperative MRI scans, may not provide accurate results. The thicker slices usually obtained with standard clinical CT scanners result in significant partial volume averaging and coarse resolution along the superior-inferior axis. Furthermore, coregistrations may be unreliable since sim-

ply performing a craniotomy is known to significantly deform brain tissue (Hill et al., 1998; Roberts et al., 1998); particularly for patients implanted with chronic electrodes, swelling and the thickness of the electrodes along with associated hardware can contribute to further brain tissue displacement relative to the preoperative MRI. While the same issues may arise with our technique since we are also registering postimplant images with preoperative structure, we expect their impact to be less significant since the algorithm fits only the portion of the brain covered by electrodes and incorporates highly reliable information from the surgical photographs. Therefore, the various projective transforms involved may effectively absorb some brain deformation.

While having a full set of high-quality image data (photographs, MRI, and radiograph) increases confidence in the results, the presented technique is still useful if some images are poor or missing altogether. MRI-radiograph coregistration can still be performed in the absence of surgical photographs with an estimate of a few electrode positions on the MRI and the use of other anatomical features as control points. Without a radiograph, MRI-photograph registration can still be performed, and the position of hidden electrodes can be estimated from known electrode spacing and brain curvature. Furthermore, at any point in the process, electrode locations can be manually adjusted to account for information from other sources such as known electrode spacing, CT coregistration, or coordinates from surgical navigation devices.

The algorithm presented is a valuable complement to existing medical imaging software that fuses different imaging modalities (e.g., existing software coregisters MRI and CT or MRI and PET). It would be useful as part of a suite of programs specifically intended for the diagnostic imaging and monitoring of neurosurgery patients with implanted electrodes. Our interactive navigation tool is clinically useful to aid in the positive identification of structures of interest on the X-ray and photograph; it would also be suitable in an educational setting to help students connect neuroanatomy with radiographs, photographs, MRI slices, and MRI renderings. Our working prototype of the electrode registration process is semi-automated; i.e., visible electrodes and landmarks must be manually selected. However, with sufficient development, it should be possible to automate some of the manual segmentation and adjustment required for typical datasets.

Acknowledgments

Special thanks to Erik Edwards for inspiring me to develop a solution to the problem of electrode registration and collaborating on its development, and to Heidi E. Kirsch and Nicholas M. Barbaro for extensive discussions on electrode implant procedures and individual patients. Additional thanks to Paul A. Garcia and David S. Filippi for acquisition of surgical photographs, Robert G. Gould and Jim Buescher for helpful information on X-ray acquisition protocols, Kenneth E.

Hild II for insightful discussions on algorithmic topics, and Susanne M. Honma for critical assistance in tracking down the medical images and personnel necessary for this project.

Chapter 5

Conclusion

5.1 Overview

I have developed methods that have advanced the study of cortical dynamics with MEG as well as addressed a critical shortcoming of ECoG that hindered its use for validation of MEG analyses.

I have worked extensively with a class of adaptive spatial filters known as beamformers due to their favorable spatial resolution and noise-resistant properties. However, beamformers may fail in the presence of strongly correlated sources; the algorithm assumes that distant brain regions are temporally uncorrelated and so any strong correlations are due to noise! For example, beamformers often fail to reconstruct auditory evoked fields (AEFs), in which both left and right auditory cortices may be simultaneously active and highly coherent. In Chapter 2,

I presented a novel beamformer to address this problem. A modified vector beamformer algorithm was designed to reject the contribution of potentially interfering sources in a user-defined suppression region while allowing for source reconstruction at other specified regions. Performance of the algorithm was validated with simulated data and bilateral AEF data.

Time-frequency analyses have recently become of great interest, especially with the discovery of high gamma activity and its apparent connection with the hemodynamic response measured by fMRI. However, few methods existed for localizing spectral power changes with MEG and, just as importantly, for navigating the resulting high-dimensional output. In Chapter 3, I presented a novel method that uses beamformers optimized for time-frequency source reconstruction from MEG data. The performance of the method was demonstrated with simulated sources and was also applied to real MEG data from a self-paced finger movement task. Modulations in both the beta band and, importantly, the high gamma band were revealed in sensorimotor cortex and found to be statistically significant across subjects. The results were additionally validated by intracranial ECoG data from two epilepsy patients. A particularly exciting finding was high frequency activity (30-300 Hz) in the cerebellum, suggesting an interesting avenue of further noninvasive research on deep brain sources with this technique. The developed algorithm is highly parallel and well-suited for fast processing on modern high performance computing clusters. Time-frequency optimized beamforming enables

and optimizes the ultimate promise of MEG and EEG for five-dimensional imaging of space, time, and frequency activity in the brain and renders it applicable for widespread studies of human cortical dynamics during cognition.

In the course of working with ECoG data, I realized that standard methods for localizing implanted electrodes were not adequate, calling into question the assumption of ECoG studies as a "gold standard" for noninvasive techniques. CT coregistration in our first patient did not yield satisfactory electrode positions due to significant brain displacement relative to the preoperative MRI. A comparison with surgical photographs confirmed that the CT coregistration, while agreeing well with the skull, resulted in a localization error of more than 10 mm. As the study progressed, it turned out that many of our patients would not have CT scans at all, but all had X-rays and surgical photographs. In conjunction with high-resolution MRI scans, I developed a method to link each of these sets of images with projective transforms, described in Chapter 4. Electrodes visible on the photograph are easily registered manually to an MRI rendering of the brain. These known positions are then used to compute the projective transform with the corresponding locations of the X-ray and the remaining electrode coordinates can then be found via backprojection to the cortical surface.

Finally, to facilitate development of all of these methods, I co-authored an analysis toolbox called NUTMEG (Neurodynamic Utility Toolbox for Magnetoencephalography) for the reconstruction and visualization of the spatiotemporal dy-

namics of neural activations. NUTMEG is the framework through which I implemented all of the methods described in this dissertation.

5.2 Future Directions

5.2.1 Time-Frequency Analysis of Deep Brain Sources

Difficulties with MEG/EEG

The detection and reconstruction of deep brain sources has traditionally been a difficult problem for both MEG and EEG. Only a few groups have shown reliable activity in deep structures (Lütkenhöner et al., 2000; Tesche, 1996; Tesche and Karhu, 1997; Hashimoto et al., 2003). These researchers—and their commendable subjects—generally go through heroic efforts involving tens of thousands of trials, painstaking artifact prevention and removal, and complicated source reconstruction techniques. Furthermore, the spherical head models typically used for EEG and MEG source localization are particularly prone to error at such depths (Sekihara et al., 2002b; Haueisen et al., 2002). Finally, structures such as the amygdala, hippocampus, thalamus, and cerebellum are not dominated by the pyramidal cells that are thought to generate most of the signal for neocortical structures. Therefore, these brain structures simply may not exhibit the type of synchrony necessary for the ERP/ERF model of activation (Section 1.3).

Auditory Brainstem Response (ABR)

For example, the auditory brainstem response (ABR), recorded with EEG electrodes on the mastoids, requires thousands of trials to form a suitable average (Jewett et al., 1970). Despite this fact, the ABR has found great clinical utility in detecting pathology in auditory pathways as a diagnostic tool; the ABR is becoming a routine screening for newborn babies in the United States (Ferro et al., 2007), is a standard test in audiology clinics (Noffsinger and Fowler, 1982), and is often used for intraoperative monitoring of the auditory nerve (Raudzens and Shetter, 1982).

The ABR appears to be a manifestation of compound action potentials of the acoustic nerve, since the characteristic ABR peaks all occur within 15 ms of the auditory stimulus and are spaced only about 2 ms apart. In any case, it seems unlikely that pyramidal cells or postsynaptic potentials contribute significantly. Therefore, it seems strange to expect that ABR responses would be perfectly phase-locked to the stimulus, and this type of activity may be well-suited to time-frequency analysis. In fact, Fridman et al. (1982) reported an attempt at spectral analysis of ABR data, but observed large "phase variance" at certain frequencies and interpreted it as a reflection of noise content!

I gathered preliminary ABR data in one subject and attempted time-frequency analysis on it. The spectrogram shown in Figure 5.1 demonstrates that the ABR contains very high frequency content (100-700 Hz) that may not be suited for av-

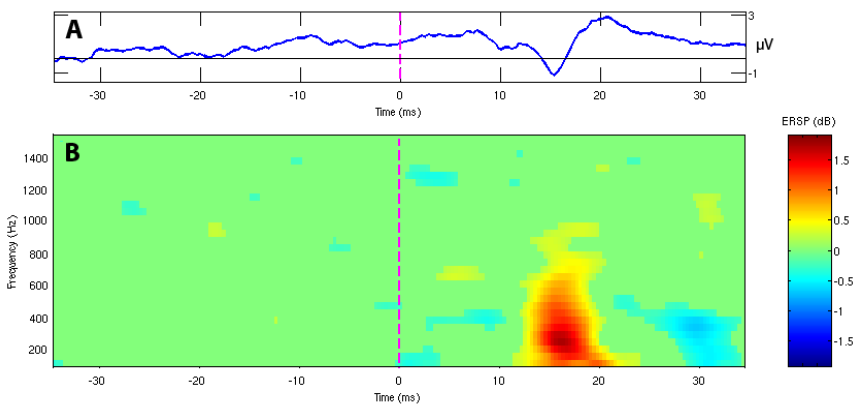

Figure 5.1 (a) The auditory brainstem response (ABR) is traditionally averaged over thousands of trials. (b) However, time-frequency analysis may provide a more appropriate characterization of acoustic nerve and brainstem function, while requiring far less trials.

eraging. Additionally, the basic spectral pattern emerges after only about 50-100 trials rather than the 1000-3000 trials often used for the average. It would be interesting to compare the ABR spectrogram of patients with hearing loss associated with cochlear or acoustic nerve pathology.

Improved Head Modeling

Source localization for ABR data is not strictly necessary since the responses precede higher brain activity and all peaks are thought to arise from the cochlea and acoustic nerve. For other deep generators, inverse methods must be optimized to distinguish them from the stronger signal of superficial sources. Finite element modeling (FEM) provides a promising approach towards improving upon the spherical head models used for EEG and MEG (Haueisen et al., 1997; Zhang et al., 2004). The errors of the spherical model are known to increase greatly

with depth, perhaps due to tissue conductivity anisotropy (Sekihara et al., 2002b; Haueisen et al., 2002)

Recently, techniques have been developed to noninvasively estimate conductivity anisotropy information from an MR technique called diffusion tensor imaging (DTI) (Wolters et al., 2006). Incorporating this information into finite element model (FEM) may be able to further refine the lead field.

Improved head models, possibly combined with the time-frequency optimized beamformers described in Chapter 3, may increase the utility of MEG for investigating deep brain sources.

Cerebellum

Our serendipitous finding of high frequency cerebellum activation with the time-frequency optimized beamformer invites further study of deeper brain structures with source reconstruction techniques and MEG. My results suggest that the cerebellum is not necessarily coherent with other sensorimotor cortex for a finger movement task (Figure 3.6). In recent years, the cerebellum has been implicated in a variety of higher cognitive functions that contradict the idea of motor control as the sole function of the cerebellum (see Marien et al., 2001, for a review). However, these studies are almost solely fMRI-based and mesoscopic intracranial recordings of the cerebellum are extremely rare in humans and even in the animal literature.

It has been suggested that it has been difficult to record cerebellar activity with

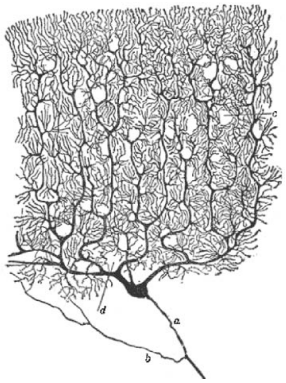

Figure 5.2 The classic tracing from Ramón y Cajal (1904) of a Golgi stain showing the dendritic arbor of cerebellar Purkinje cells. The dendrites are arranged in parallel, similar to the apical dendrites of pyramidal cells, and likely are the major contributors to externally recorded electromagnetic fields from the cerebellum.

noninvasive EEG since the neurons of the cerebellum are arranged in a "closed field" configuration (Ito, 1984). However, the arrangement of Purkinje cells in cerebellar cortex (Ramón y Cajal, 1904) seem very analogous to pyramidal cells in cerebral cortex (see Figure 5.2) and likely contribute to the signal that we have recorded with MEG. Therefore, I am optimistic that, as Niedermeyer (2004) suggested, MEG can provide further insight into the role of the cerebellum in human cognition and action.

Amygdala and Hippocampus

The amygdala and hippocampus are other brain structures that have been difficult to observe with EEG and MEG. In addition to their integral roles in emotion and memory, respectively, they are often suspected of generating seizures in many epilepsy patients. Currently, invasive recordings are the only way to confirm

epileptiform activity in these structures. Noninvasively studying the dynamics of the amygdala and hippocampus can therefore advance both cognitive neuroscience as well as the treatment of epilepsy, and may be possible with the methods described in this dissertation. A particularly attractive advantage to this line of research is the possibility for validation from invasive recordings.

5.3 Final Thoughts

MEG is making the transition into a mature neuroimaging technique as a result of developments in the areas of source reconstruction, head modeling, statistics, and probabilistic models. As partially illustrated by this dissertation, MEG, EEG, and ECoG stand to benefit greatly from questioning many of the traditional assumptions of the field. MEG is not doomed to record sulcal generators, activity above 40 Hz is not necessarily noise, the average ERP/ERF is not necessarily the most appropriate model of neural activation for all experiments, neocortical pyramidal cells are not necessarily the only contributors to MEG/EEG signal, and the cerebellum likely has a role broader than motor control. I find it amazing how much resistance I encounter from prominent researchers on these concepts from time to time. I have no doubt that state-of-the-art technology combined with new analysis methods will continue to push the frontier of neuroimaging and challenge many deeply held assumptions of neuroscience.

Appendix A

NUTMEG: Neurodynamic Utility Toolbox for Magnetoencephalography[1]

Abstract

We have developed an analysis toolbox called NUTMEG (Neurodynamic Utility Toolbox for Magnetoencephalography) for reconstructing the spatiotemporal dynamics of neural activations and overlaying them onto structural MR images. The toolbox runs under MATLAB in conjunction with SPM2 and can be used with the Linux/UNIX, Mac OS X, and even Windows platforms. Currently, evoked

[1]This chapter is adapted from an article published in *Neurology and Clinical Neurophysiology* (Dalal et al., 2004)

magnetic field data from 4-D Neuroimaging, CTF, and KIT systems can be imported to the toolbox for analysis. NUTMEG uses an eigenspace vector beamforming algorithm to generate a tomographic reconstruction of spatiotemporal magnetic source activity over selected time intervals and spatial regions. The MEG coordinate frame is coregistered with an anatomical MR image using fiducial locations and, optionally, head shape information. This allows the reconstruction to be superimposed onto an MRI to provide a convenient visual correspondence to neuroanatomy. Navigating through the MR volume automatically updates the displayed time series of activation for the selected voxel. Animations can also be generated to view the evolution of neural activity over time. Since NUTMEG displays activations using SPM2's engine, certain SPM functions such as brain rendering and spatial normalization may be applied as well. Finally, as a MATLAB package, the end user can easily add customized functions. Source code is available at http://bil.ucsf.edu/ and distributed under a BSD-style license.

A.1 Introduction

Magnetoencephalography (MEG) and electroencephalography (EEG) noninvasively measure the magnetic and electric fields generated by neuronal currents, respectively, and can detect such activity with fine temporal resolution. The potential to localize the sources of these signals more accurately has emerged with the ad-

vent of dense MEG and EEG sensor arrays. Traditional multiple-dipole methods assume that a small set of current dipoles can adequately represent the distribution of an unknown source. While these methods are ideal for focal sources when the number of sources is known a priori or can be deduced from the spatiotemporal distribution of the data, problems arise if the sources have a large spatial extent or are otherwise not well characterized by current dipoles (Jeffs et al., 1987). This is often the case, for example, in cognitive studies or studies involving sensorimotor integration. In addition, finding the dipole model which best accounts for the actual distribution of sources may be difficult because of problems in estimating the correct model order and in finding the optimal solution of the nonlinear optimization problem associated with multiple-dipole source models.

Studies of the inverse problem have traditionally focused on improving the spatial resolution of MEG and EEG, with the accepted limit being on the order of 2 mm to 5 mm (Leahy et al., 1998). However, a second problem in MEG/EEG involves estimating the time course of source activations. A spatial filtering technique called beamforming provides an efficient solution, without requiring a priori assumptions about the location or number of neural sources. Using such a class of algorithms, MEG source reconstructions can be viewed as a "virtual depth electrode" measurement technique. We have developed the Neurodynamic Utility Toolbox for Magnetoencephalography (NUTMEG) to implement a data-dependent spatial filter for MEG spatiotemporal source reconstructions and

to coregister the results of these reconstructions onto anatomical MRI volumes. NUTMEG provides an easy-to-use software suite to generate and visualize neural source reconstructions from MEG sensor arrays (Figure A.1).

A.2 Methods

NUTMEG is written for MATLAB (MathWorks, Natick, MA, USA), and requires SPM2 (http://www.fil.ion.ucl.ac.uk/spm). The interface with SPM2 allows activations to be overlaid onto standard orthogonal MRI slices or a rendered 3-D brain volume; at present, SPM2's analysis engine is not used. Activations may also be spatially normalized and displayed on an MNI template brain (Evans et al., 1993; Mazziotta et al., 2001). All development and testing has been with dual 2 GHz Pentium Xeon systems with 2 GB of RAM running Red Hat Linux 9, though NUTMEG should be compatible with any platform running MATLAB 6.5 or 7. NUTMEG is open source and freely available (http://bil.ucsf.edu) for noncommercial use under a BSD-style license (Open Source Initiative, 2004). Currently, MEG data may be readily imported from systems manufactured by CTF Systems, 4D Neuroimaging (BTi), and KIT/Yokogawa; shortly, it will also support data from Elekta Neuromag systems.

NUTMEG implements an adaptive spatial filter called an eigenspace vector beamformer (Sekihara et al., 2001). We currently employ the spherically symmetric

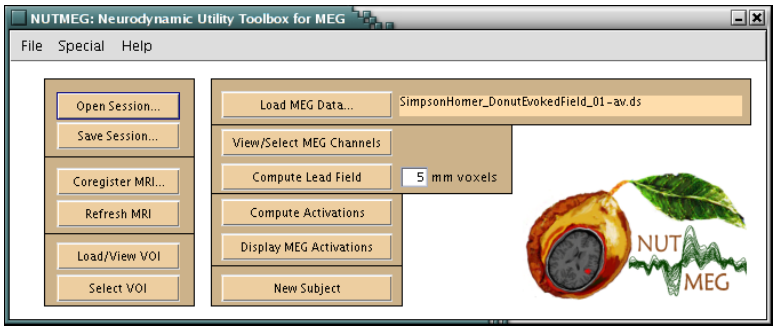

Figure A.1 The main graphical user interface for NUTMEG.

volume conductor model in our computations (Sarvas, 1987). Lead field calculations with this forward model have been vectorized and, using a spatial resolution of 5 mm, can be generated within a few seconds even for large reconstruction volumes. The vector beamformer separates sources into three orthogonal directions (although the radial component has no contribution with a spherical head model). As with all beamformers, the sensor covariance plays an important role; the eigenspace modification separates this covariance matrix into signal and noise subspace components using singular value decomposition (Sekihara et al., 2001) (see Figure A.2).

In the course of our laboratory's methods development, several additional source reconstruction and denoising algorithms have been incorporated as plugins to NUTMEG. I have described an approach to circumventing the correlated source weakness of beamforming in Chapter 2 and Dalal et al. (2006). The increasing availability of high performance computing clusters (e.g., the California Institute for Quantitative Biomedical Research Shared Computing Facility) have made

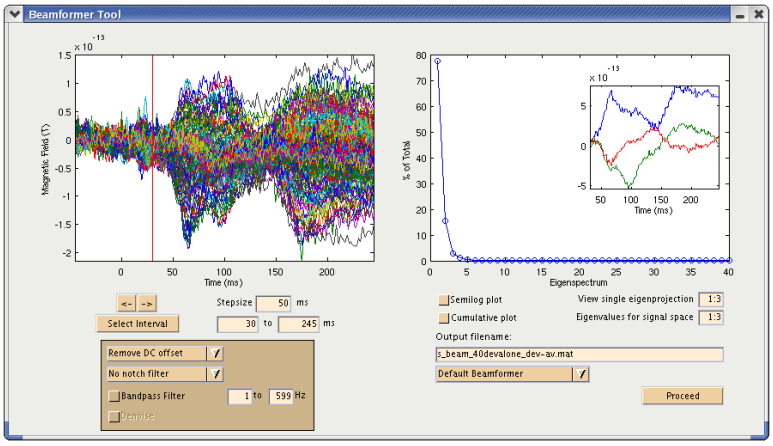

Figure A.2 Interactive tool showing MEG sensor data (left) and singular values of the sensor covariance matrix (right) with associated eigenprojections (right, inset). The time interval and signal subspace desired for beamforming reconstruction can be selected here.

highly intensive source reconstruction algorithms more feasible; I took advantage of this computing power to implement time-frequency optimized beamforming of unaveraged MEG data described in Chapter 3. Additionally, my colleagues have implemented algorithms based on graphical modeling, factor analysis, and Bayesian techniques (Nagarajan et al., 2006; Zumer et al., 2006, 2007).

For visualization, the MEG coordinate system is coregistered onto an anatomical MRI using fiducial information to calculate an appropriate affine transformation matrix. Optionally, information obtained from a headshape digitizer may be used to further refine this transformation. The reconstruction volume can be selected by simply drawing outlines on the orthogonal cross-sections of the MRI (see Figure A.3). Alternatively, if the subject's MRI is registered to the MNI template, whole-brain VOIs may be automatically generated from the template's brain mask.

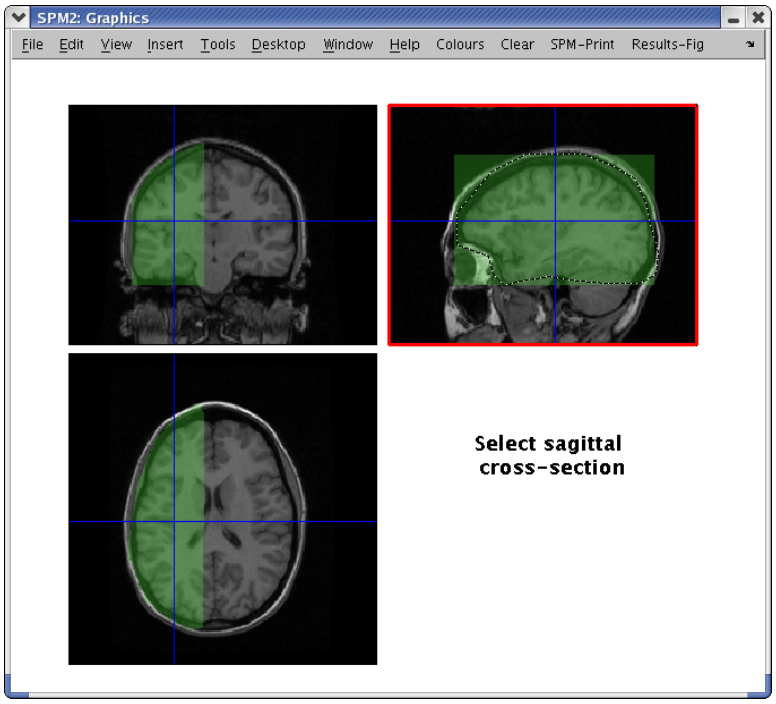

Figure A.3 Interface for manually selecting volume of interest (VOI) for beamformer reconstruction. VOIs may be defined by drawing outlines on each of the three orthogonal cross-sections. Alternatively, if the subject's MRI is registered to the MNI template, whole-brain VOIs may be automatically generated from the template's brain mask.

Final results can be navigated in space, time, and optionally frequency through a graphical interface (see Figure A.4 and A.5).

A.3 Results

To demonstrate some of the features and capabilities of NUTMEG, we report results on phantom data and a human study collected with a CTF Omega 275 system (VSM MedTech, Coquitlam, BC, Canada) at UCSF.

The phantom consisted of a spherical saline-filled volume conductor containing

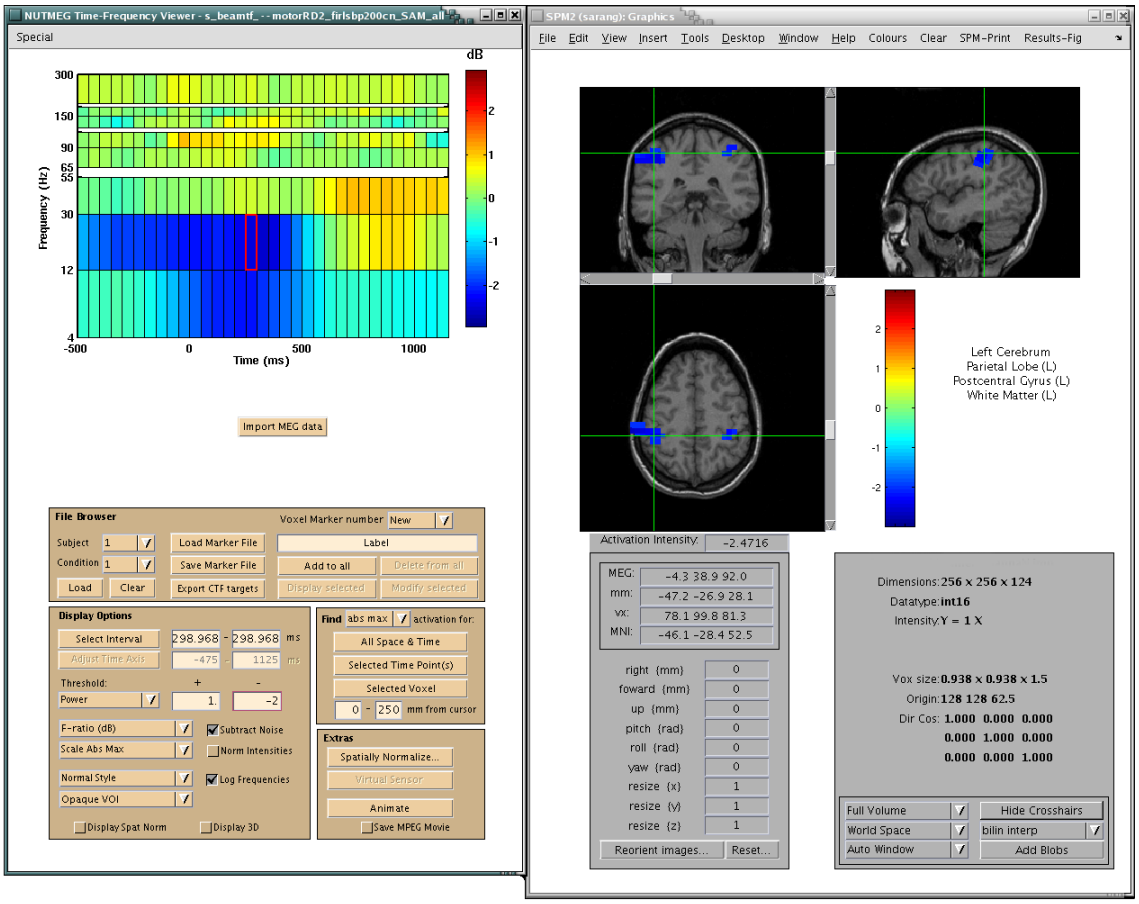

Figure A.4 Interactive navigation of space, time, and frequency output from the time-frequency optimized beamformer (Chapter 3). Shown analysis is for a right index finger movement, with movement onset occurring at 0 ms. The time-frequency spectrogram, MNI coordinates, and Talairach atlas labels are automatically updated by clicking on the MRI slices to select a new brain location. Conversely, selecting a new time-frequency window on the spectrogram updates the spatial map displayed on the MRI.

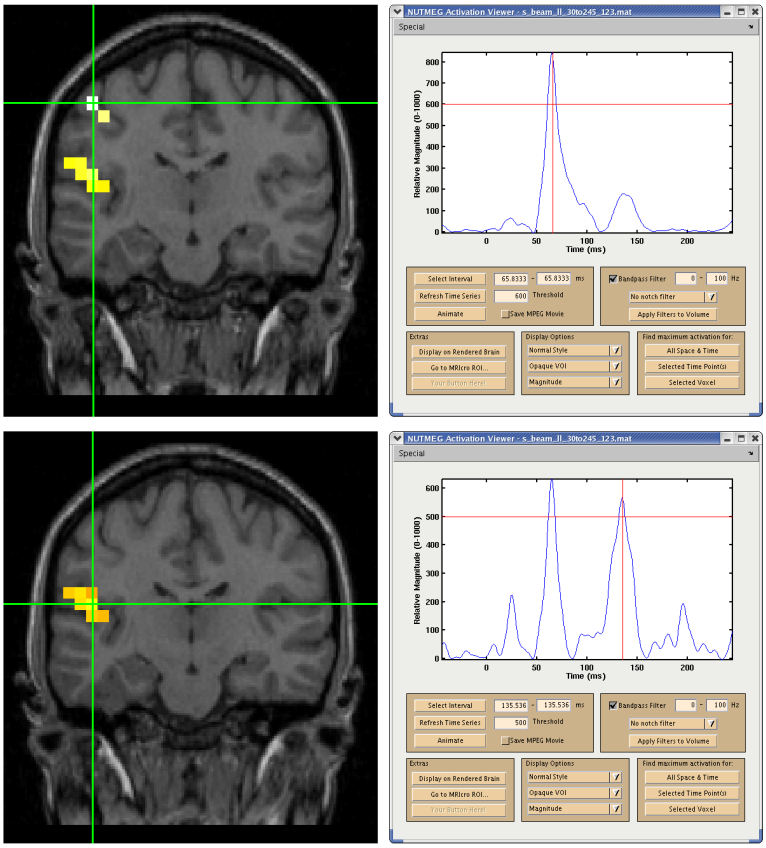

Figure A.5 Beamformer reconstruction of evoked tactile stimulation of right D2 showing time series and localization for S1 at 66 ms (top) and S2 at 136 ms (bottom); note S2 also shows activity at 66 ms (slice has been tilted to include both S1 and S2). The peak at 20 ms is due to stimulus artifact.

a current source set to oscillate at 7 Hz and 0.3 V_{pp}, yielding a peak dipole moment of 17 nAm. The SNR was approximately 34 dB, calculated by dividing the signal subspace eigenvalue by the sum of the noise subspace eigenvalues. The theoretical location of the phantom dipole was (36, 0, 30) mm. Using a 2 mm reconstruction grid, NUTMEG localized the source in a voxel centered at (36.0, 2.0, 30.0) mm. Standard dipole source localization placed the source of the current phantom at (35.6, 1.7, 28.9) mm, which is located within the same voxel. These results are

within the expected error range of 3 mm from the theoretical location.

The second data set was a somatosensory evoked field collected from a normal human adult subject; a piezoelectric device was used to stimulate a finger on the right hand (RD2) with a 25 ms, 40 Hz vibration. NUTMEG localized two focal areas of activation; a peak at 66 ms showed a coactivation of areas corresponding to S1 and S2, while a broad peak near 136 ms activated primarily S2 (see Figure A.5).

A.4 Conclusion

We have developed an extensible toolbox that uses an eigenspace vector beamformer to reconstruct the spatiotemporal dynamics of neural sources from MEG sensor arrays. This toolbox allows a user unfamiliar with the details of beamforming to reconstruct spatiotemporal activations from MEG sensor data. Results from this toolbox can facilitate comparisons of results with other functional neuroimaging modalities such as fMRI and PET.

Methods for assessing the statistical significance of beamformer activation maps are under investigation (e.g., Sekihara et al., 2005a) and will soon be implemented. The vector beamformer currently used by NUTMEG is robust to weakly coherent sources and other forms of low-rank interferences (Sekihara et al., 2002a; Zumer et al., 2004). However, all beamformers poorly resolve multiple strongly coherent sources. We have developed several methods to suppress activity from

such interfering sources (Sahani and Nagarajan, 2004; Dalal et al., 2005). Future directions for NUTMEG include incorporating support for more sophisticated head models as well as additional source localization methods.

Acknowledgments

My primary co-developer, Johanna M. Zumer, deserves much credit and praise for tirelessly working with me to help make NUTMEG an indispensable research tool at the Biomagnetic Imaging Laboratory. Special thanks go to Kenneth E. Hild II, Vineet K. Agrawal, and Adrian G. Guggisberg for substantial contributions to NUTMEG, as well as Kensuke Sekihara for extensive collaborations on algorithm development and David J. McGonigle for discussions on MEG analysis needs and interfacing with SPM. Alex Wade, Tom Holroyd, Fred Carver, and Darren Weber are also acknowledged for critical contributions to source code. Finally, thanks to Anne M. Findlay, John F. Houde, Theda Heinks-Maldonado, and Anthony M. Norcia for valuable feedback.

Bibliography

Abdel-Azziz, Y. and Karara, H. (1971). Direct linear transformation from comparator coordinates into object space coordinates in close-range photogrammetry. In *Papers from the 1971 ASP Symposium on Close-range Photogrammetry*, pages 1–18, Falls Church, VA. American Society for Photogrammetry.

Adrian, E. D. (1935). Discharge frequencies in the cerebral and cerebellar cortex. *J Physiol*, 83:32P–33P.

Ashburner, J. and Friston, K. J. (1999). Nonlinear spatial normalization using basis functions. *Hum Brain Mapp*, 7:254–266.

Bancaud, J., Talairach, J., and Bonis, A. (1965). *La stéréo-électroencéphalographie dans l'epilepsie*. Masson, Paris.

Barnes, G. R. and Hillebrand, A. (2003). Statistical flattening of MEG beamformer images. *Hum Brain Mapp*, 18:1–12.

Barnett, G. H., Kormos, D. W., Steiner, C. P., and Morris, H. (1993). Registration of

EEG electrodes with three-dimensional neuroimaging using a frameless, armless stereotactic wand. *Stereotact Funct Neurosurg*, 61:32–38.

Berger, H. (1929). Über das elektrenkephalogramm des menschen. *Arch Psychiat Nervenkr*.

Berger, H. (1930). Über das elektrenkephalogramm des menschen. *J Psychol Neurol*, 40:160–179.

Bootsveld, K., Träber, F., Kaiser, W. A., Layer, G., Elger, C. E., Hufnagel, A., Gieseke, J., and Reiser, M. (1994). Localisation of intracranial eeg electrodes using three dimensional surface reconstructions of the brain. *European Radiology*, 4:52–56.

Brovelli, A., Lachaux, J.-P., Kahane, P., and Boussaoud, D. (2005). High gamma frequency oscillatory activity dissociates attention from intention in the human premotor cortex. *NeuroImage*, 28:154–164.

Bullock, T. H., McClune, M. C., Achimowicz, J. Z., Iragui-Madoz, V. J., Duckrow, R. B., and Spencer, S. S. (1995). EEG coherence has structure in the millimeter domain: Subdural and hippocampal recordings from epileptic patients. *Electroencephalogr Clin Neurophysiol*, 95:161–177.

Canolty, R. T., Edwards, E., Dalal, S. S., Soltani, M., Nagarajan, S. S., Kirsch, H. E., Berger, M. S., Barbaro, N. M., and Knight, R. T. (2006). High gamma power is phase-locked to theta oscillations in human neocortex. *Science*, 313:1626–1628.

Cheyne, D., Gaetz, W., Garnero, L., Lachaux, J.-P., Ducorps, A., Schwartz, D., and Varela, F. J. (2003). Neuromagnetic imaging of cortical oscillations accompanying tactile stimulation. *Brain Res Cogn Brain Res*, 17:599–611.

Cohen, D. (1968). Magnetoencephalography: evidence of magnetic fields produced by alpha-rhythm currents. *Science*, 161:784–786.

Crone, N. E., Boatman, D., Gordon, B., and Hao, L. (2001a). Induced electrocorticographic gamma activity during auditory perception. *Clin Neurophysiol*, 112:565–582.

Crone, N. E., Hao, L., Hart, J., Boatman, D., Lesser, R. P., Irizarry, R., and Gordon, B. (2001b). Electrocorticographic gamma activity during word production in spoken and sign language. *Neurology*, 57:2045–2053.

Crone, N. E., Miglioretti, D. L., Gordon, B., and Lesser, R. P. (1998). Functional mapping of human sensorimotor cortex with electrocorticographic spectral analysis. II. Event-related synchronization in the gamma band. *Brain*, 121 (Pt 12):2301–2315.

Crone, N. E., Sinai, A., and Korzeniewska, A. (2006). Chapter 19: High-frequency gamma oscillations and human brain mapping with electrocorticography. *Prog Brain Res*, 159:275–295.

Dalal, S. S., Edwards, E., Kirsch, H. E., Barbaro, N. M., Knight, R. T., and Na-

garajan, S. S. (2007a). Localization of neurosurgically implanted electrodes via photograph-MRI-radiograph coregistration. Submitted.

Dalal, S. S., Edwards, E., Kirsch, H. E., Canolty, R. T., Soltani, M., Barbaro, N. M., Knight, R. T., and Nagarajan, S. S. (2005). Spatiotemporal dynamics of cortical networks preceding finger movement and speech production [abstract]. In *Proceedings of the 16th Meeting of the International Society for Brain Electromagnetic Topography*, Bern, Switzerland.

Dalal, S. S., Guggisberg, A. G., Edwards, E., Sekihara, K., Findlay, A. M., Canolty, R. T., Berger, M. S., Knight, R. T., Barbaro, N. M., Kirsch, H. E., and Nagarajan, S. S. (2007b). Five-dimensional neuroimaging: Localization of the time-frequency dynamics of cortical activity. Submitted.

Dalal, S. S., Sekihara, K., and Nagarajan, S. S. (2006). Modified beamformers for coherent source region suppression. *IEEE Trans Biomed Eng*, 53:1357–1363.

Dalal, S. S., Zumer, J. M., Agrawal, V., Hild, K. E., Sekihara, K., and Nagarajan, S. S. (2004). NUTMEG: A neuromagnetic source reconstruction toolbox. *Neurol Clin Neurophysiol*, page 52.

Dale, A. M., Fischl, B., and Sereno, M. I. (1999). Cortical surface-based analysis. I. Segmentation and surface reconstruction. *NeuroImage*, 9:179–194.

Dale, A. M. and Sereno, M. I. (1993). Improved localization of cortical activity by combining eeg and meg with mri cortical surface reconstruction. *J Cogn Neurosci*.

Darvas, F., Pantazis, D., Kucukaltun-Yildirim, E., and Leahy, R. M. (2004). Mapping human brain function with MEG and EEG: methods and validation. *NeuroImage*, 23 Suppl 1:S289–S299.

Dhamala, M., Pagnoni, G., Wiesenfeld, K., Zink, C. F., Martin, M., and Berns, G. S. (2003). Neural correlates of the complexity of rhythmic finger tapping. *NeuroImage*, 20:918–926.

Dimitrova, A., de Greiff, A., Schoch, B., Gerwig, M., Frings, M., Gizewski, E. R., and Timmann, D. (2006). Activation of cerebellar nuclei comparing finger, foot and tongue movements as revealed by fMRI. *Brain Res Bull*, 71:233–241.

Dow, R. S. (1938). The electrical activity of the cerebellum and its functional significance. *J Physiol*, 94:67–86.

Edwards, E. (2007). *Electrocortical Activation and Human Brain Mapping*. PhD thesis, University of California, Berkeley.

Edwards, E., Soltani, M., Deouell, L. Y., Berger, M. S., and Knight, R. T. (2005). High gamma activity in response to deviant auditory stimuli recorded directly from human cortex. *J Neurophysiol*, 94:4269–4280.

Evans, A. C., Collins, D. L., Mills, S. R., Brown, E. D., Kelly, R. L., and Peters, T. M.

(1993). 3d statistical neuroanatomical models from 305 mri volumes. In *Proc IEEE Nucl Sci Symp Med Imaging Conf*, volume 3, pages 1813–1817.

Fein, G., Raz, J., Brown, F. F., and Merrin, E. L. (1988). Common reference coherence data are confounded by power and phase effects. *Electroencephalogr Clin Neurophysiol*, 69:581–584.

Ferro, L. M., Tanner, G., Erler, S. F., Erickson, K., and Dhar, S. (2007). Comparison of universal newborn hearing screening programs in Illinois hospitals. *Int J Pediatr Otorhinolaryngol*, 71:217–230.

Fischl, B., Sereno, M. I., and Dale, A. M. (1999). Cortical surface-based analysis. II: Inflation, flattening, and a surface-based coordinate system. *NeuroImage*, 9:195–207.

Fox, P. T., Perlmutter, J. S., and Raichle, M. E. (1985). A stereotactic method of anatomical localization for positron emission tomography. *J Comput Assist Tomogr*, 9(1):141–153.

Freeman, W. J. (1975). *Mass action in the nervous system: examination of the neurophysiological basis of adaptive behavior through the EEG*. Academic Press, New York.

Fridman, J., John, E. R., Bergelson, M., Kaiser, J. B., and Baird, H. W. (1982). Application of digital filtering and automatic peak detection to brain stem auditory evoked potential. *Electroencephalogr Clin Neurophysiol*, 53:405–416.

Gaetz, W. and Cheyne, D. (2006). Localization of sensorimotor cortical rhythms induced by tactile stimulation using spatially filtered MEG. *NeuroImage*, 30:899–908.

Greenblatt, R. E., Ossadtchi, A., and Pflieger, M. E. (2005). Local linear estimators for the bioelectromagnetic inverse problem. *IEEE Trans Signal Process*, 53:3403–3412.

Grodd, W., Hülsmann, E., Lotze, M., Wildgruber, D., and Erb, M. (2001). Sensorimotor mapping of the human cerebellum: fMRI evidence of somatotopic organization. *Hum Brain Mapp*, 13:55–73.

Gross, J. and Ioannides, A. A. (1999). Linear transformations of data space in MEG. *Phys Med Biol*, 44:2081–2097.

Gross, J., Kujala, J., Hamalainen, M., Timmermann, L., Schnitzler, A., and Salmelin, R. (2001). Dynamic imaging of coherent sources: Studying neural interactions in the human brain. *Proc Natl Acad Sci U S A*, 98:694–699.

Gross, J., Timmermann, L., Kujala, J., Dirks, M., Schmitz, F., Salmelin, R., and Schnitzler, A. (2002). The neural basis of intermittent motor control in humans. *Proc Natl Acad Sci U S A*, 99:2299–2302.

Grzeszczuk, R., Tan, K. K., Levin, D. N., Pelizzari, C. A., Hu, X., Chen, G. T. Y., Beck, R. N., Chen, C.-t., Cooper, M., Milton, J., Spire, J.-P., Towle, V. L., Dohrmann, G. J.,

and Erickson, R. K. (1992). Retrospective fusion of radiographic and MR data for localization of subdural electrodes. *J Comput Assist Tomogr*, 16(5):764–773.

Guggisberg, A. G., Dalal, S. S., Findlay, A. M., and Nagarajan, S. S. (2007). High-frequency oscillations in distributed neural networks reveal the dynamics of human decision making. Submitted.

Gulrajani, R. M. (1998). *Bioelectricity and Biomagnetism*. Wiley, New York.

Gutiérrez, L. F., Shechter, G., Lederman, R. J., McVeigh, E. R., and Ozturk, C. (2005). Distortion correction, calibration, and registration: Towards an integrated MR and X-ray interventional suite. In Galloway, R. L. and Cleary, K. R., editors, *Proceedings of the SPIE Medical Imaging Conference*, volume 5744, pages 146–156.

Hämäläinen, M., Hari, R., IImoniemi, R. J., Knuutila, J., and Lounasmaa, O. V. (1993). Magnetoencephalography–theory, instrumentation, and applications to noninvasive studies of the working human brain. *Rev Mod Phys*, 65:413–497.

Hämäläinen, M. S. and Sarvas, J. (1989). Realistic conductivity geometry model of the human head for interpretation of neuromagnetic data. *IEEE Trans Biomed Eng*, 36:165–171.

Hanslmayr, S., Klimesch, W., Sauseng, P., Gruber, W., Doppelmayr, M., Freunberger, R., Pecherstorfer, T., and Birbaumer, N. (2007). Alpha phase reset contributes to the generation of ERPs. *Cereb Cortex*, 17(1):1–8.

Hartley, R. I. and Zisserman, A. (2004). *Multiple View Geometry in Computer Vision*. Cambridge University Press, second edition.

Hashimoto, I., Kimura, T., Tanosaki, M., Iguchi, Y., and Sekihara, K. (2003). Muscle afferent inputs from the hand activate human cerebellum sequentially through parallel and climbing fiber systems. *Clin Neurophysiol*, 114:2107–2117.

Haueisen, J., Ramon, C., Eiselt, M., Brauer, H., and Nowak, H. (1997). Influence of tissue resistivities on neuromagnetic fields and electric potentials studied with a finite element model of the head. *IEEE Trans Biomed Eng*, 44:727–735.

Haueisen, J., Tuch, D. S., Ramon, C., Schimpf, P. H., Wedeen, V. J., George, J. S., and Belliveau, J. W. (2002). The influence of brain tissue anisotropy on human EEG and MEG. *Neuroimage*, 15:159–166.

Herdman, A. T., Wollbrink, A., Chau, W., Ishii, R., Ross, B., and Pantev, C. (2003). Determination of activation areas in the human auditory cortex by means of synthetic aperture magnetometry. *NeuroImage*, 20:995–991005.

Hill, D. L., Maurer, C. R., Maciunas, R. J., Barwise, J. A., Fitzpatrick, J. M., and Wang, M. Y. (1998). Measurement of intraoperative brain surface deformation under a craniotomy. *Neurosurgery*, 43:514–526.

Hinkley, L. B. N., Nagarajan, S. S., Dalal, S. S., and Disbrow, E. A. (2006). Activity in human posterior parietal cortex during visually-guided reaching and saccadic

eye movements: an MEG study [abstract]. In *Proceedings of the 36th Annual Meeting of the Society for Neuroscience*, Atlanta, GA.

Hochberg, L. R., Serruya, M. D., Friehs, G. M., Mukand, J. A., Saleh, M., Caplan, A. H., Branner, A., Chen, D., Penn, R. D., and Donoghue, J. P. (2006). Neuronal ensemble control of prosthetic devices by a human with tetraplegia. *Nature*, 442:164–171.

Hoogenboom, N., Schoffelen, J.-M., Oostenveld, R., Parkes, L. M., and Fries, P. (2006). Localizing human visual gamma-band activity in frequency, time and space. *NeuroImage*, 29:764–773.

Huang, M. X., Mosher, J. C., and Leahy, R. M. (1999). A sensor-weighted overlapping-sphere head model and exhaustive head model comparison for MEG. *Phys Med Biol*, 44:423–440.

Hülsmann, E., Erb, M., and Grodd, W. (2003). From will to action: Sequential cerebellar contributions to voluntary movement. *NeuroImage*, 20:1485–1492.

Hunter, J. D., Hanan, D. M., Singer, B. F., Shaikh, S., Brubaker, K. A., Hecox, K. E., and Towle, V. L. (2005). Locating chronically implanted subdural electrodes using surface reconstruction. *Clin Neurophysiol*, 116(8):1984–1987.

Ishii, R., Shinosaki, K., Ukai, S., Inouye, T., Ishihara, T., Yoshimine, T., Hirabuki, N.,

Asada, H., Kihara, T., Robinson, S. E., and Takeda, M. (1999). Medial prefrontal cortex generates frontal midline theta rhythm. *NeuroReport*, 10:675–679.

Ito, M. (1984). *The Cerebellum and Neural Control*. Raven, New York.

Ivry, R. B. and Keele, S. W. (1989). Timing functions of the cerebellum. *J Cogn Neurosci*, 1:136–152.

Jeffs, B., Leahy, R., and Singh, M. (1987). An evaluation of methods for neuromagnetic image reconstruction. *IEEE Trans Biomed Eng*, 34:713–723.

Jenkinson, M., Pechaud, M., and Smith, S. (2005). BET2: MR-based estimation of brain, skull and scalp surfaces. In *Eleventh Annual Meeting of the Organization for Human Brain Mapping*.

Jewett, D. L., Romano, M. N., and Williston, J. S. (1970). Human auditory evoked potentials: Possible brain stem components detected on the scalp. *Science*, 167:1517–1518.

Jurkiewicz, M. T., Gaetz, W. C., Bostan, A. C., and Cheyne, D. (2006). Post-movement beta rebound is generated in motor cortex: Evidence from neuromagnetic recordings. *NeuroImage*, 32:1281–1289.

Kaiser, J., Lutzenberger, W., Ackermann, H., and Birbaumer, N. (2002). Dynamics of gamma-band activity induced by auditory pattern changes in humans. *Cereb Cortex*, 12:212–221.

Katila, T., Maniewski, R., Poutanen, T., Varpula, T., and Karp, P. J. (1981). Magnetic fields produced by the human eye. *J Appl Phys*, 52(3):2565–2571.

Kirchberger, K., Hummel, C., and Stefan, H. (1998). Postoperative multichannel magnetoencephalography in patients with recurrent seizures after epilepsy surgery. *Acta Neurol Scand*, 98:1–7.

Kovalev, D., Spreer, J., Honegger, J., Zentner, J., Schulze-Bonhage, A., and Huppertz, H.-J. (2005). Rapid and fully automated visualization of subdural electrodes in the presurgical evaluation of epilepsy patients. *AJNR Am J Neuroradiol*, 26:1078–1083.

Lachaux, J.-P., Fonlupt, P., Kahane, P., Minotti, L., Hoffmann, D., Bertrand, O., and Baciu, M. (2007). Relationship between task-related gamma oscillations and BOLD signal: New insights from combined fMRI and intracranial EEG. *Hum Brain Mapp*. In press.

Lachaux, J.-P., George, N., Tallon-Baudry, C., Martinerie, J., Hugueville, L., Minotti, L., Kahane, P., and Renault, B. (2005). The many faces of the gamma band response to complex visual stimuli. *NeuroImage*, 25:491–501.

Leahy, R. M., Mosher, J. C., Spencer, M. E., Huang, M. X., and Lewine, J. D. (1998). A study of dipole localization accuracy for MEG and EEG using a human skull phantom. *Electroencephalogr Clin Neurophysiol*, 107:159–173.

Lehmann, D. and Michel, C. M. (1990). Intracerebral dipole source localization for FFT power maps. *Electroencephalogr Clin Neurophysiol*, 76:271–276.

Lesser, R. P., Gordon, B., Fisher, R. S., Hart, J., and Uematsu, S. (1991). Subdural grid electrodes in surgery of epilepsy. In Lüders, H. O., editor, *Epilepsy Surgery*. Raven, New York.

Leuthardt, E. C., Miller, K. J., Schalk, G., Rao, R. P. N., and Ojemann, J. G. (2006). Electrocorticography-based brain computer interface–the Seattle experience. *IEEE Trans Neural Syst Rehabil Eng*, 14:194–198.

Leuthardt, E. C., Schalk, G., Wolpaw, J. R., Ojemann, J. G., and Moran, D. W. (2004). A brain-computer interface using electrocorticographic signals in humans. *J Neural Eng*, 1:63–71.

Levenberg, K. (1944). A method for the solution of certain nonlinear problems in least squares. *Quart Appl Math*, 2:164–168.

Logothetis, N. K., Pauls, J., Augath, M., Trinath, T., and Oeltermann, A. (2001). Neurophysiological investigation of the basis of the fMRI signal. *Nature*, 412:150–157.

Lotze, M., Scheler, G., Tan, H.-R. M., Braun, C., and Birbaumer, N. (2003). The musician's brain: Functional imaging of amateurs and professionals during performance and imagery. *NeuroImage*, 20:1817–1829.

Lütkenhöner, B. (1992). Frequency-domain localization of intracerebral dipolar sources. *Electroencephalogr Clin Neurophysiol*, 82:112–118.

Lütkenhöner, B., Lammertmann, C., Ross, B., and Pantev, C. (2000). Brain stem auditory evoked fields in response to clicks. *NeuroReport*, 11:913–918.

Makeig, S. (1993). Auditory event-related dynamics of the EEG spectrum and effects of exposure to tones. *Electroencephalogr Clin Neurophysiol*, 86:283–293.

Malmivuo, J. and Plonsey, R. (1995). *Bioelectromagnetism—Principles and Applications of Bioelectric and Biomagnetic Fields*. Oxford University Press, New York.

Malmivuo, J., Suihko, V., and Eskola, H. (1997). Sensitivity distributions of EEG and MEG measurements. *IEEE Trans Biomed Eng*, 44:196–208.

Marien, P., Engelborghs, S., and De Deyn, P. P. (2001). Cerebellar neurocognition: a new avenue. *Acta Neurol Belg*, 101:96–9109.

Marquardt, D. W. (1963). An algorithm for least-squares estimation of nonlinear parameters. *SIAM J Appl Math*, 11:431–444.

Mazziotta, J., Toga, A., Evans, A., Fox, P., Lancaster, J., Zilles, K., Woods, R., Paus, T., Simpson, G., Pike, B., Holmes, C., Collins, L., Thompson, P., MacDonald, D., Iacoboni, M., Schormann, T., Amunts, K., Palomero-Gallagher, N., Geyer, S., Parsons, L., Narr, K., Kabani, N., Le Goualher, G., Boomsma, D., Cannon, T.,

Kawashima, R., and Mazoyer, B. (2001). A probabilistic atlas and reference system for the human brain: International Consortium for Brain Mapping (ICBM). *Philos Trans R Soc Lond B Biol Sci*, 356:1293–1322.

Michalewski, H. J., Prasher, D. K., and Starr, A. (1986). Latency variability and temporal interrelationships of the auditory event-related potentials (N1, P2, N2, and P3) in normal subjects. *Electroencephalogr Clin Neurophysiol*, 65:59–71.

Miller, K. J., Makeig, S., Hebb, A. O., Rao, R. P. N., denNijs, M., and Ojemann, J. G. (2007). Cortical electrode localization from X-rays and simple mapping for electrocorticographic research: The "Location on Cortex" (LOC) package for MATLAB. *J Neurosci Methods*.

Mosher, J. C., Baillet, S., and Leahy, R. M. (1999). EEG source localization and imaging using multiple signal classification approaches. *J Clin Neurophysiol*, 16:225–238.

Mosher, J. C., Spencer, M. E., Leahy, R. M., and Lewis, P. S. (1993). Error bounds for EEG and MEG dipole source localization. *Electroencephalogr Clin Neurophysiol*, 86:303–321.

Mukamel, R., Gelbard, H., Arieli, A., Hasson, U., Fried, I., and Malach, R. (2005). Coupling between neuronal firing, field potentials, and FMRI in human auditory cortex. *Science*, 309:951–954.

Nagarajan, S. S., Attias, H. T., Hild, K. E., and Sekihara, K. (2006). A graphical model for estimating stimulus-evoked brain responses from magnetoencephalography data with large background brain activity. *NeuroImage*, 30:400–416.

Nelles, M., König, R., Kandyba, J., Schaller, C., and Urbach, H. (2004). Koregistrierung von mrt vor und CT nach der implantation subduraler gitterelektroden. *Zentralbl Neurochir*, 65(4):174–179.

Niedermeyer, E. (2004). The electrocerebellogram. *Clin EEG Neurosci*, 35:112–115.

Niessing, J., Ebisch, B., Schmidt, K. E., Niessing, M., Singer, W., and Galuske, R. A. W. (2005). Hemodynamic signals correlate tightly with synchronized gamma oscillations. *Science*, 309:948–951.

Noffsinger, D. and Fowler, C. G. (1982). Brain stem auditory evoked potentials: Applications in clinical audiology. *Bull Los Angeles Neurol Soc*, 47:43–54.

Nunez, P. L. and Srinivasan, R. (2006). *Electric Fields of the Brain: The Neurophysics of EEG*. New York: Oxford University Press, second edition.

Nunez, P. L., Srinivasan, R., Westdorp, A. F., Wijesinghe, R. S., Tucker, D. M., Silberstein, R. B., and Cadusch, P. J. (1997). EEG coherency. I: Statistics, reference electrode, volume conduction, Laplacians, cortical imaging, and interpretation at multiple scales. *Electroencephalogr Clin Neurophysiol*, 103:499–515.

Ohara, S., Ikeda, A., Kunieda, T., Yazawa, S., Baba, K., Nagamine, T., Taki, W., Hashimoto, N., Mihara, T., and Shibasaki, H. (2000). Movement-related change of electrocorticographic activity in human supplementary motor area proper. *Brain*, 123:1203–1215.

Ojemann, G., Ojemann, J., Lettich, E., and Berger, M. (1989). Cortical language localization in left, dominant hemisphere. An electrical stimulation mapping investigation in 117 patients. *J Neurosurg*, 71:316–326.

Ojemann, G. A. (1979). Individual variability in cortical localization of language. *J Neurosurg*, 50:164–169.

Open Source Initiative (2004). The BSD license. http://www.opensource.org/licenses/bsd-license.php.

Osipova, D., Takashima, A., Oostenveld, R., Fernández, G., Maris, E., and Jensen, O. (2006). Theta and gamma oscillations predict encoding and retrieval of declarative memory. *J Neurosci*, 26:7523–7531.

Pascual-Marqui, R. D. (2002). Standardized low-resolution brain electromagnetic tomography (sLORETA): technical details. *Methods Find Exp Clin Pharmacol*, 24 Suppl D:5–12.

Pekkonen, E., Huotilainen, M., Virtanen, J., Sinkkonen, J., Rinne, T., Ilmoniemi,

R. J., and Näätänen, R. (1995). Age-related functional differences between auditory cortices: a whole-head MEG study. *NeuroReport*, 6:1803–1806.

Pellet, J. (1967). L'électrocérébellogramme vermien au cours des états de veille et de sommeil. *Brain Res*, 5:266–270.

Penfield, W. and Roberts, L. (1959). *Speech and Brain Mechanisms*. Princeton University Press, Princeton, NJ.

Pfurtscheller, G. and Aranibar, A. (1977). Event-related cortical desynchronization detected by power measurements of scalp EEG. *Electroencephalogr Clin Neurophysiol*, 42:817–826.

Pfurtscheller, G. and Cooper, R. (1975). Frequency dependence of the transmission of the EEG from cortex to scalp. *Electroencephalogr Clin Neurophysiol*, 38:93–96.

Pfurtscheller, G., Graimann, B., Huggins, J. E., Levine, S. P., and Schuh, L. A. (2003). Spatiotemporal patterns of beta desynchronization and gamma synchronization in corticographic data during self-paced movement. *Clin Neurophysiol*, 114:1226–1236.

Pfurtscheller, G. and Lopes da Silva, F. H. (1999). Event-related EEG/MEG synchronization and desynchronization: Basic principles. *Clin Neurophysiol*, 110:1842–1857.

Pfurtscheller, G. and Neuper, C. (1992). Simultaneous EEG 10 Hz desynchronization and 40 Hz synchronization during finger movements. *NeuroReport*, 3:1057–1060.

Pfurtscheller, G., Stancák, A., and Neuper, C. (1996). Post-movement beta synchronization. A correlate of an idling motor area? *Electroencephalogr Clin Neurophysiol*, 98:281–293.

Phillips, J. W., Leahy, R. M., and Mosher, J. C. (1997). MEG-based imaging of focal neuronal current sources. *IEEE Trans Med Imaging*, 16:338–348.

Pollok, B., Gross, J., Müller, K., Aschersleben, G., and Schnitzler, A. (2005). The cerebral oscillatory network associated with auditorily paced finger movements. *NeuroImage*, 24:646–655.

Ramón y Cajal, S. (1893). La rétine des vertébrés. *La Cellule*, 9:119–257.

Ramón y Cajal, S. (1904). *Textura del Sistema Nervioso del Hombre y de los Vertebrados*. N. Moya, Madrid.

Ramón y Cajal, S. (1905). *Studien Über die Hirnrinde des Menschen*. Verlag von Johann Ambrosius Barth, Leipzig.

Raudzens, P. A. and Shetter, A. G. (1982). Intraoperative monitoring of brain-stem auditory evoked potentials. *J Neurosurg*, 57:341–348.

Raz, J., Cardenas, V., and Fletcher, D. (1995). Frequency domain estimation of covariate effects in multichannel brain evoked potential data. *Biometrics*, 51:448–460.

Roberts, D. W., Hartov, A., Kennedy, F. E., Miga, M. I., and Paulsen, K. D. (1998). Intraoperative brain shift and deformation: a quantitative analysis of cortical displacement in 28 cases. *Neurosurgery*, 43:749–58; discussion 758.

Robinson, S. E., Nagarajan, S. S., Mantle, M., Gibbons, V., and Kirsch, H. (2004). Localization of interictal spikes using SAM(g2) and dipole fit. *Neurol Clin Neurophysiol*, 2004:74–74.

Robinson, S. E. and Vrba, J. (1999). Functional neuroimaging by synthetic aperture magnetometry. In Yoshimoto, T., Kotani, M., Kuriki, S., Karibe, H., and Nakasato, N., editors, *Recent Advances in Biomagnetism*, pages 302–305, Sendai. Tohoku University Press.

Rorden, C. and Brett, M. (2000). Stereotaxic display of brain lesions. *Behav Neurol*, 12:191–200.

Rosset, A., Spadola, L., and Ratib, O. (2004). OsiriX: an open-source software for navigating in multidimensional DICOM images. *J Digit Imaging*, 17:205–216.

Sahani, M. and Nagarajan, S. S. (2004). Reconstructing MEG sources with un-

known correlations. In Thrun, S., Saul, L. K., and Schölkopf, B., editors, *Advances in Neural Information Processing Systems 16*. MIT Press, Cambridge, MA.

Salmelin, R. H. and Hämäläinen, M. S. (1995). Dipole modelling of MEG rhythms in time and frequency domains. *Brain Topogr*, 7:251–257.

Santhanam, G., Ryu, S. I., Yu, B. M., Afshar, A., and Shenoy, K. V. (2006). A high-performance brain-computer interface. *Nature*, 442:195–198.

Sarvas, J. (1987). Basic mathematical and electromagnetic concepts of the biomagnetic inverse problem. *Phys Med Biol*, 32:11–22.

Scherg, M. and von Cramon, D. (1986). Evoked dipole source potentials of the human auditory cortex. *Electroencephalogr Clin Neurophysiol*, 65:344–360.

Schiffbauer, H., Berger, M. S., Ferrari, P., Freudenstein, D., Rowley, H. A., and Roberts, T. P. L. (2003). Preoperative magnetic source imaging for brain tumor surgery: a quantitative comparison with intraoperative sensory and motor mapping. *Neurosurg Focus*, 15:E7–E7.

Schulze-Bonhage, A. H.-J., Huppertz, H. J., Comeau, R. M., Honegger, J. B., Spreer, J. M., and Zentner, J. K. (2002). Visualization of subdural strip and grid electrodes using curvilinear reformatting of 3D MR imaging data sets. *AJNR Am J Neuroradiol*, 23:400–403.

Sekihara, K., Nagarajan, S., Poeppel, D., and Miyashita, Y. (1999). Time-frequency MEG-MUSIC algorithm. *IEEE Trans Med Imaging*, 18:92–97.

Sekihara, K., Nagarajan, S. S., Poeppel, D., and Marantz, A. (2002a). Performance of an MEG adaptive-beamformer technique in the presence of correlated neural activities: Effects on signal intensity and time-course estimates. *IEEE Trans Biomed Eng*, 49:1534–1546.

Sekihara, K., Nagarajan, S. S., Poeppel, D., and Marantz, A. (2004). Asymptotic SNR of scalar and vector minimum-variance beamformers for neuromagnetic source reconstruction. *IEEE Trans Biomed Eng*, 51:1726–1734.

Sekihara, K., Nagarajan, S. S., Poeppel, D., Marantz, A., and Miyashita, Y. (2001). Reconstructing spatio-temporal activities of neural sources using an MEG vector beamformer technique. *IEEE Trans Biomed Eng*, 48:760–771.

Sekihara, K., Nagarajan, S. S., Poeppel, D., Miyauchi, S., Fujimaki, N., Koizumi, H., and Miyashita, Y. (2000). Estimating neural sources from each time-frequency component of magnetoencephalographic data. *IEEE Trans Biomed Eng*, 47:642–653.

Sekihara, K., Nagarajan, S. S., Robinson, S. E., and Vrba, J. (2002b). Spatial resolution, leakage, and signal-to-noise ratio in adaptive beamformer source reconstruction technique. In Nowak, H., Haueisen, J., Giessler, F., and Huonker, R.,

editors, *Proceedings of the 13th International Conference on Biomagnetism*, page 813, Berlin. VDE.

Sekihara, K., Sahani, M., and Nagarajan, S. S. (2005a). A simple nonparametric statistical thresholding for MEG spatial-filter source reconstruction images. *NeuroImage*, 27:368–376.

Sekihara, K., Sahani, M., and Nagarajan, S. S. (2005b). Localization bias and spatial resolution of adaptive and non-adaptive spatial filters for MEG source reconstruction. *NeuroImage*, 25:1056–1067.

Sekihara, K. and Scholz, B. (1996). Generalized Wiener estimation of three-dimensional current distribution from biomagnetic measurements. In Aine, C. J., editor, *Biomag 96: Proceedings of the Tenth International Conference on Biomagnetism*, pages 338–341. Springer-Verlag.

Siegel, M., Donner, T. H., Oostenveld, R., Fries, P., and Engel, A. K. (2006). High-Frequency Activity in Human Visual Cortex Is Modulated by Visual Motion Strength. *Cereb Cortex*.

Singh, K. D., Barnes, G. R., and Hillebrand, A. (2003). Group imaging of task-related changes in cortical synchronisation using nonparametric permutation testing. *NeuroImage*, 19:1589–1601.

Singh, K. D., Barnes, G. R., Hillebrand, A., Forde, E. M. E., and Williams, A. L.

(2002). Task-related changes in cortical synchronization are spatially coincident with the hemodynamic response. *NeuroImage*, 16:103–114.

Sochůrková, Danielarková, D., Rektor, I., Jurák, P., and Stančák, A. (2006). Intracerebral recording of cortical activity related to self-paced voluntary movements: a Bereitschaftspotential and event-related desynchronization/synchronization. SEEG study. *Exp Brain Res*, 173:637–649.

Talairach, J. and Tournoux, P. (1988). *Co-Planar Stereotaxic Atlas of the Human Brain*. Thieme, Stuttgart, Germany.

Tang, L., Mantle, M., Ferrari, P., Schiffbauer, H., Rowley, H. A., Barbaro, N. M., Berger, M. S., and Roberts, T. P. L. (2003). Consistency of interictal and ictal onset localization using magnetoencephalography in patients with partial epilepsy. *J Neurosurg*, 98:837–845.

Taniguchi, M., Kato, A., Fujita, N., Hirata, M., Tanaka, H., Kihara, T., Ninomiya, H., Hirabuki, N., Nakamura, H., Robinson, S. E., Cheyne, D., and Yoshimine, T. (2000). Movement-related desynchronization of the cerebral cortex studied with spatially filtered magnetoencephalography. *NeuroImage*, 12:298–306.

Ten Cate, J. and Wiggers, N. (1942). On the occurrence of slow waves in the electrocerebellogram. *Arch Neerl Physiol l'Homme Anim*, 26:433–435.

Tesche, C. D. (1996). Non-invasive imaging of neuronal population dynamics in human thalamus. *Brain Res*, 729:253–258.

Tesche, C. D. and Karhu, J. (1997). Somatosensory evoked magnetic fields arising from sources in the human cerebellum. *Brain Res*, 744:23–31.

Thickbroom, G. W., Byrnes, M. L., and Mastaglia, F. L. (2003). Dual representation of the hand in the cerebellum: Activation with voluntary and passive finger movement. *NeuroImage*, 18:670–674.

Towle, V. L., Carder, R. K., Khorasani, L., and Lindberg, D. (1999). Electrocorticographic coherence patterns. *J Clin Neurophysiol*, 16:528–547.

van den Broek, S. P., Reinders, F., Donderwinkel, M., and Peters, M. J. (1998). Volume conduction effects in EEG and MEG. *Electroencephalogr Clin Neurophysiol*, 106:522–534.

Van Veen, B. D. and Buckley, K. M. (1988). Beamforming: A versatile approach to spatial filtering. *IEEE Acoust Speech Signal Processing Mag*, 5:4–24.

Van Veen, B. D., van Drongelen, W., Yuchtman, M., and Suzuki, A. (1997). Localization of brain electrical activity via linearly constrained minimum variance spatial filtering. *IEEE Trans Biomed Eng*, 44:867–880.

van Wassenhove, V. and Nagarajan, S. S. (2006). Auditory-visual habituation in

perceptual recalibration [abstract]. In *Proceedings of the 13th Annual Meeting of the Cognitive Neuroscience Society*, San Francisco, CA.

van Wassenhove, V. and Nagarajan, S. S. (2007). Auditory cortical plasticity in learning to discriminate modulation rate. *J Neurosci*, 27:2663–2672.

Vidal, J. R., Chaumon, M., O'Regan, J. K., and Tallon-Baudry, C. (2006). Visual grouping and the focusing of attention induce gamma-band oscillations at different frequencies in human magnetoencephalogram signals. *J Cogn Neurosci*, 18:1850–1862.

Vrba, J. and Robinson, S. E. (2002). SQUID sensor array configurations for magnetoencephalography applications. *Supercond Sci Technol*, 15(9):R51–R89.

Wada, J. and Rasmussen, T. (1960). Intracarotid injection of sodium amytal for the lateralization of cerebral speech dominance. *J Neurosurg*, 17:266–282.

Wellmer, J., von Oertzen, J., Schaller, C., Urbach, H., König, R., Widman, G., Van Roost, D., and Elger, C. E. (2002). Digital photography and 3D MRI-based multimodal imaging for individualized planning of resective neocortical epilepsy surgery. *Epilepsia*, 43:1543–1550.

Winkler, P. A., Vollmar, C., Krishnan, K. G., Pfluger, T., Brückmann, H., and Noachtar, S. (2000). Usefulness of 3-D reconstructed images of the human cere-

bral cortex for localization of subdural electrodes in epilepsy surgery. *Epilepsy Res*, 41:169–178.

Wolters, C. H., Anwander, A., Tricoche, X., Weinstein, D., Koch, M. A., and MacLeod, R. S. (2006). Influence of tissue conductivity anisotropy on EEG/MEG field and return current computation in a realistic head model: a simulation and visualization study using high-resolution finite element modeling. *NeuroImage*, 30:813–826.

Wyler, A. R., Walker, G., Richey, E. T., and Hermann, B. P. (1988). Chronic subdural strip electode recordings for difficult epileptic problems. *J Epilepsy*, 1:71–78.

Yuan, X., Zhang, J., and Buckles, B. P. (2004). Evolution strategies based image registration via feature matching. *Information Fusion*, 5(4):269–282.

Zhang, Y. C., Zhu, S. A., and He, B. (2004). A second-order finite element algorithm for solving the three-dimensional EEG forward problem. *Phys Med Biol*, 49:2975–2987.

Zumer, J. M., Attias, H. T., Sekihara, K., and Nagarajan, S. S. (2006). Two probabilistic algorithms for MEG/EEG source reconstruction. In *2006 IEEE ISBI: From Nano to Macro*.

Zumer, J. M., Attias, H. T., Sekihara, K., and Nagarajan, S. S. (2007). A probabilistic algorithm integrating source localization and noise suppression for MEG and

EEG data. In Schölkopf, B., Platt, J., and Hoffman, T., editors, *Adv. Neur. Info. Proc. Sys. 19*. MIT Press, Cambridge, MA.

Zumer, J. M., McGonigle, D. J., Disbrow, E. A., Dalal, S. S., Zhu, Z., and Nagarajan, S. S. (2004). Magnetic source imaging of somatosensory frequency mismatch responses [abstract]. In *Proceedings of the 34th Annual Meeting of the Society for Neuroscience*, New Orleans, LA.